UNIVERSIDADE FEDERAL DE SANTA CATARINA
CENTRO DE CIÊNCIAS FÍSICAS E MATEMÁTICAS
PROGRAMA DE PÓS-GRADUAÇÃO EM FÍSICA

Giovana Conod

Interacting Active Galactic Nuclei: Investigating a Triple Merger

Florianópolis (SC)
2026

Giovana Conod

Interacting Active Galactic Nuclei: Investigating a Triple Merger

Dissertação submetida ao Programa de Pós-Graduação em Física da Universidade Federal de Santa Catarina para a obtenção do título de Mestre em Física.
Orientador: Prof. Daniel Ruschel Dutra, Dr.

Florianópolis (SC)
2026

Ficha catalográfica gerada por meio de sistema automatizado gerenciado pela BU/UFSC.
Dados inseridos pelo próprio autor.

Conod, Giovana
Interacting Active Galactic Nuclei: Investigating a Triple Merger / Giovana Conod ; orientador, Daniel Ruschel Dutra, 2026.
75 p.

Dissertação (mestrado) - Universidade Federal de Santa Catarina, Centro de Ciências Físicas e Matemáticas, Programa de Pós-Graduação em Física, Florianópolis, 2026.

Inclui referências.

1. Física. 2. Astrofísica Extragaláctica. 3. Núcleos Ativos de Galáxias. 4. Evolução Galáctica. I. Dutra, Daniel Ruschel. II. Universidade Federal de Santa Catarina. Programa de Pós-Graduação em Física. III. Título.

Giovana Conod

Interacting Active Galactic Nuclei: Investigating a Triple Merger

O presente trabalho em nível de Mestrado foi avaliado e aprovado, em 3 de novembro de 2025, por banca examinadora composta pelos seguintes membros:

Prof. Daniel Ruschel Dutra, Dr.
Universidade Federal de Santa Catarina (UFSC)

Profa. Natalia Vale Asari, Dra.
Universidade Federal de Santa Catarina (UFSC)

Prof. Jose Andres Hernandez Jimenez, Dr.
Universidad de Investigación y Desarrollo (UDI)

Certificamos que esta é a **versão original e final** do trabalho de conclusão que foi julgado adequado para obtenção do título de Mestre em Física.

Documento assinado digitalmente
Natalia Vale Asari
Data: 26/01/2026 10:09:30-0300
CPF: ***.497.091-**
Verifique as assinaturas em https://v.ufsc.br

Coordenação do Programa de
Pós-Graduação em Física

Documento assinado digitalmente
Daniel Ruschel Dutra
Data: 22/01/2026 09:02:36-0300
CPF: ***.099.190-**
Verifique as assinaturas em https://v.ufsc.br

Prof. Daniel Ruschel Dutra, Dr.
Orientador

Florianópolis (SC), 2026.

AGRADECIMENTOS

Essa conquista não teria sido possível sem o apoio de amigos, família e professores. Agradeço ao meu orientador, Daniel Ruschel, pelos ensinamentos e paciência em ensinar. Os conhecimentos que adquiri durante esses dois anos irão me acompanhar pelo resto da minha carreira acadêmica. Sou extremamente grata pela oportunidade de começá-la com uma base tão sólida. Agradeço também aos professores do grupo Roberto Saito, Roberto Cid, Natalia Assari, André Amorim e Antônio Kannan, que também tiveram papel fundamental em minha formação.

Agradeço aos colegas de laboratório pelas trocas de ideias para solucionar problemas e pelos socorros prestados quando os códigos não funcionavam. Janayna Mendes, Victor Hugo Sasse, Márlon de Carvalho, Rhana Lunkes, Jonathan Ramos, Mirley Mesquita, Roberto Kammers, Vitor Fermiano e Ricardo Hesse. Aos meus amigos de curso Letícia Bertuzzi, Alyson Fernando De Barros, João Pedro Engster, Haimon Otto Trebien, Bruna Vallin, Raphael Pacheco Cardoso e Maria Gabriela Damaceno, por todas as conversas e ajuda com listas de exercícios.

Agradeço aos meus melhores amigos Nicolas de Castro e Eduardo Zanella, que estão comigo desde o início, quando éramos apenas calouros. Quero levar vocês para a vida toda.

Agradeço ao meu namorado, Fernando Miguel Hahne, cujo apoio foi imprescindível para que eu chegasse até aqui. Eu não estaria aqui sem você, e não consigo colocar em palavras a gratidão que tenho por tudo o que você já fez por mim.

Por fim, agradeço a meus pais, Angelita Silveira, Edson Conod, Adriana Amorim, e minha irmã Aline de Oliveira, por todo o apoio durante todos esses anos de estudos, e por todo o incentivo.

RESUMO

O paradigma atual para a formação de galáxias é baseado em um modelo hierárquico, em que ao longo da história do Universo galáxias menores se fundiram em sucessivas interações até chegarem ao estado atual. Ao mesmo tempo, sabemos que a maior parte do crescimento dos buracos negros supermassivos (SMBH) que se encontram no núcleo das galáxias ocorreu antes de $z = 1$. Portanto, fusões de galáxias mais recentes do que isso necessariamente implicam na interação entre os SMBHs e, eventualmente, em sua fusão. O objetivo deste trabalho é compreender a fusão de buracos negros a partir da observação de sistemas em que estes ainda são entidades separadas e comparar essas observações com outros sistemas em interação, para tentar traçar um quadro mais geral, que sirva de vínculo para os modelos cosmológicos e de evolução de galáxias. Neste trabalho estudamos dados de espectroscopia de campo integral obtidos com o instrumento MUSE, instalado no Very Large Telescope (VLT) do Observatório Europeu Austral (ESO). Utilizamos dados do trio de galáxias em interação SDSSJ0849+1114, que possui três núcleos ativos confirmados por emissão de raio-X, e com distância projetada de ~ 3.5 kpc e ~ 5.3 kpc para os núcleos sul e norte, respectivamente, com relação ao núcleo principal. Utilizando o software IFSCube, fizemos os ajustes das linhas de emissão, e identificamos a presença de uma região de linhas estreitas estendida em todas as galáxias, com velocidades relativas entre ± 150 km s^{-1}, que sugere que a interação está ocorrendo majoritariamente no plano do céu. A análise de emissão também mostrou uma região no centro do sistema cuja cinemática do gás necessita de uma segunda função gaussiana para ser corretamente ajustada; acreditamos ser devido ao feedback do AGN principal, cujas observações anteriores mostraram a presença de um jato de rádio na região, que estaria causando um outflow. A partir de uma análise da cinemática do sistema, nós conseguimos determinar uma possível órbita para as galáxias do sistema. As galáxias principal e sul parecem estar orbitando uma a outra rotacionando da direita para a esquerda, em um ângulo de aproximadamente 135°. A galáxia norte, entretanto, parece estar orbitando as outras duas perpendicularmente. Pelos rastros de gás deixados para trás, nós acreditamos que ela já tenha contornado as outras duas pelo menos uma vez. A análise das razões de linhas de emissão mostram que o processo de ionização do gás presente na galáxia não pode ser explicado apenas por formação estelar; ao redor dos três núcleos os diagramas BPT e WHAN sugerem que a fonte ionização do gás naquelas regiões se dá pela presença do AGN. Também vemos indícios de regiões de formação estelar próximas ao núcleo sul e ao longo do braço adjacente a ele. A análise de população estelar mostra que, em média, as estrelas do sistema são bastante velhas (> 1 Gyr), e com metalicidades um pouco menor do que a metalicidade do Sol.

Palavras-chave: Astrofísica extragaláctica. Núcleos ativos de galáxias. Evolução de galáxias.

ABSTRACT

The current paradigm for galaxy formation is based on a hierarchical model, in which, throughout the history of the Universe, smaller galaxies merged through successive interactions until they reached their current state. At the same time, we know that most of the growth of supermassive black holes (SMBHs) at the cores of galaxies occurred before z=1. Therefore, galaxy mergers more recent than this necessarily imply interactions between SMBHs and, eventually, their merger. The goal of this work is to understand black hole mergers by observing systems in which they are still separate entities and to compare these observations with other interacting systems, attempting to draw a more general picture that serves as a link for cosmological and galaxy evolution models. In this work, we study integral-field spectroscopy data obtained with the MUSE instrument, installed on the Very Large Telescope (VLT) of the European Southern Observatory (ESO). We used data from the interacting galaxy trio SDSSJ0849+1114, which has three active nuclei confirmed by X-ray emission, and with projected distances of ~ 3.5 kpc and ~ 5.3 kpc for the southern and northern nuclei, respectively, relative to the main nucleus. Using IFSCube software, we fitted the emission lines and identified the presence of a region of narrow lines extended across all galaxies, with relative velocities between ± 150 km s^{-1}, suggesting that the interaction is occurring primarily in the plane of the sky. The emission analysis also revealed a region at the center of the system whose gas kinematics require a second Gaussian function to fit correctly; we believe this is due to feedback from the main AGN, whose previous observations showed the presence of a radio jet in the region, causing an outflow. From an analysis of the system's kinematics, we were able to determine a possible orbit for the galaxies in the system. The main and southern galaxies appear to be orbiting each other, rotating from right to left, at an angle of approximately 135°. The northern galaxy, however, appears to be orbiting the other two at right angles. From the gas trails it leaves behind, we believe it has already circled the other two at least once. Analysis of the emission line ratios shows that the ionization process of the gas present in the galaxy cannot be explained solely by star formation; around the three cores, the BPT and WHAN diagrams suggest that the source of gas ionization in those regions is the presence of AGN. We also see evidence of star-forming regions near the southern core and along the adjacent arm. Analysis of the stellar population shows that, on average, the stars in the system are quite old (> 1 Gyr) and with metallicities slightly below that of the Sun.

Keywords: Extragalactic astrophysics. Active galactic nuclei. Galaxy evolution.

RESUMO EXPANDIDO

Introdução

Os Núcleos Ativos de Galáxias (AGN — *Active Galactic Nuclei* em inglês) são regiões compactas no centro de algumas galáxias capazes de produzir grandes quantidades de energia. Essa energia não pode ser explicada pela fusão termonuclear das estrelas presentes na galáxia; em vez disso, é atribuída à acreção de matéria por buracos negros supermassivos localizados no núcleo destas. A investigação de AGNs é crucial para a compreensão da evolução das galáxias, servindo como um laboratório para o estudo da física em condições extremas.

O consenso atual é de que buracos negros supermassivos (SMBH) estão presentes no centro da maioria das galáxias [Kormendy e Richstone 1995], [Kormendy e Ho 2013], conceito que foi primeiro proposto por [Lynden-Bell, D. 1969]. O modelo unificado propõe que, ao redor do SMBH, forma-se um disco de acreção composto pela matéria de sua galáxia hospedeira quando esta matéria perde momento angular e cai em direção ao núcleo. Quando este processo ocorre, dizemos que o núcleo da galáxia está ativo, onde energia gravitacional é convertida em energia térmica e luz.

O paradigma atual da evolução galáctica se baseia em um modelo hierárquico, em que a formação das galáxias massivas que observamos hoje resulta de sucessivas fusões de galáxias menores. Ao mesmo tempo, sabemos que a maior parte do crescimento de SMBH ocorreu antes de $z = 1$. Portanto, fusões de galáxias mais recentes do que isso necessariamente implicam na interação entre os SMBHs e, eventualmente, em sua fusão. O estudo de galáxias em processo de interação, então, se torna essencial para compreender os impactos que o AGN causa na sua galáxia hospedeira, já que pode suprimir ou aumentar a taxa de formação estelar.

Neste trabalho investigamos um trio de galáxias em estágios inicias de interação que possui três núcleos ativos confirmados pela detecção de emissão de raio-X pelo *Chandra X-ray Survey* [Foord et al. 2021] e com distância projetada de ~ 3.5 kpc e ~ 5.3 kpc para os núcleos sul e norte, respectivamente, com relação ao núcleo principal.

Metodologia

A análise dos dados foi conduzida por meio de uma sequência de procedimentos, começando pelo pré-processamento dos dados, onde identificamos e descartamos dados incorretos devido a erros computacionais e de instrumentação. Isolamos os dados da galáxia no cubo de dados e os cortamos para otimizar nosso trabalho. Após extrair os espectros, fizemos as correções por redshift e extinção Galáctica por poeira.

Para a síntese de populações estelares, utilizamos o código STARLIGHT para modelar a composição estelar das galáxias, a fim de recuperar a história de formação estelar da galáxia. Para isso, ajustamos uma combinação linear de populações estelares compostas (CSPs), baseadas na biblioteca BC03 [Bruzual e Charlot 2003]. Utilizamos uma base com 3 metalicidades e 15 idades. Adicionalmente, incluímos na base uma combinação de leis de potência para ajustar melhor a região ao redor do núcleo. A análise das linhas de emissão foi feita com o software IFSCube, que ajustou as diferentes componentes das linhas de emissão utilizando funções gaussianas.

Resultados

A síntese de população estelar revela que as populações estelares presentes na galáxia são, em média, bastante velhas (> 1 Gyr), e com metalicidades um pouco abaixo da metalicidade do Sol.
A análise de emissão também mostrou uma região no centro do sistema cuja cinemática do gás necessita de uma segunda função gaussiana para ajustar corretamente; acreditamos ser devido ao feedback do AGN principal, cujas observações anteriores mostraram a presença de um jato de rádio na região, que estaria causando um outflow.
A partir de uma análise da cinemática do sistema, nós conseguimos determinar uma possível órbita para as galáxias do sistema. As galáxias principal e sul parecem estar orbitando uma a outra rotacionando da direita para a esquerda, em um ângulo de aproximadamente 135°. A galáxia norte, entretanto, parece estar orbitando as outras duas perpendicularmente. Pelos rastros de gás deixados para trás, nós acreditamos que ela já tenha contornado as outras duas pelo menos uma vez.
A análise das razões de linhas de emissão mostram que o processo de ionização do gás presente na galáxia não pode ser explicado apenas por formação estelar; ao redor dos três núcleos os diagramas BPT e WHAN sugerem que a fonte ionização do gás naquelas regiões se dá pela presença do AGN. Também vemos indícios de regiões de formação estelar próximas ao núcleo sul e ao longo do braço adjacente a ele.

Considerações finais

Neste trabalho, realizamos uma análise detalhada de um sistema triplo de galáxias em interação, obtendo resultados sobre a cinemática das galáxias, suas populações estelares e os mecanismos de fotoionização. Identificamos perturbações dinâmicas causadas pelas interações gravitacionais entre as galáxias, que afetam a distribuição do gás e o movimento das estrelas. Esperamos que estes resultados nos ajudem a descobrir os mecanismos complexos que regem a formação e evolução de galáxias.

Palavras-chave: Astrofísica extragaláctica. Núcleos ativos de galáxias. Evolução de galáxias.

LIST OF FIGURES

LIST OF ABBREVIATIONS AND ACRONYMS

2dFGRS	2dF Galaxy Redshift Survey
ADC	Analog-to-Digital Converter
ADS	Archaeological Downsizing
AGN	Active Galactic Nucleus / Nuclei
BOOMERanG	Balloon Observations Of Millimetric Extragalactic Radiation And Geophysics Experiment
BPT	Baldwin, Phillips, Telervich
CCD	Charge-Coupled Device
CDM	Cold Dark Matter
CMD	Cosmic Microwave Background
CPS	Composite Stellar Population
EW	Equivalent Width
FWHM	Full Width at Half Maximum
IFS	Integral Field Spectroscopy
IFUs	Integral Field Units
IMF	Initial Mass Function
IR	Infrared
LINER	Low-ionization Nuclear Emission-line Region
MUSE	Multi-Unit Spectroscopic Explorer
NFM	Narrow Field Mode
PSF	Point Spread Function
QSOs	Quasi-Stellar Objects
RG	Retired Galaxies
S/N	Signal-to-Noise
SDSS	Sloan Digital Sky Survey

SED	Spectral Energy Distribution
SFH	Star Formation History
SFRs	Star Formation Rates
SMBH	Supermassive Black Hole
SPS	Stellar Population Synthesis
SSP	Simple Stellar Population
UV	Ultraviolet
VLT	Very Large Telescope
wAGN	weak Active Galactic Nuclei
WFM	Wide Field Mode

CONTENTS

1 INTRODUCTION

Active Galactic Nuclei (AGNs) are among the most energetic and dynamic phenomena in the Universe. At the center of these objects lies a supermassive black hole [Magorrian et al. 1998, Ho 2008, Kormendy e Ho 2013]. Powered by a mass accretion process, AGNs are extremely bright, often outshining all the stars present in their host galaxies combined [Lynden-Bell, D. 1969, Shakura e Sunyaev 1973]. Evidence suggests a strong connection between the build-up of stellar mass in galactic bulges and the evolution of the central black hole, with gravitational torques funneling gas to the central regions of galaxies, thereby fueling both star formation and black hole accretion [Haehnelt, Natarajan e Rees 1998, Richstone et al. 1998, Haan et al. 2009]. Some properties of the bulge, such as stellar velocity dispersion, are linked to the mass of the black hole, which also scales linearly with the absolute blue luminosity of the bulge [Ferrarese e Merritt 2000, Gebhardt et al. 2000, Kormendy e Richstone 1995]. We know that the mass growth of SMBHs is due to the accretion during the AGN phase, but there is speculation whether energy and momentum feedback from nuclear activity may be sufficient to reshape the host galaxy, since the exact mechanisms remain unclear [Silk e Rees 1998, Matteo, Springel e Hernquist 2005, Croton et al. 2006]. It is still uncertain how feedback operates within galaxies and what the specific processes behind AGN feedback are, but simulations and observational data suggest that it can affect the properties of the interstellar medium (ISM), suppress or trigger star formation [Fabian 2012, King e Pounds 2015].

The current consensus, based on the hierarchical model of evolution, is that the massive galaxies we see nowadays are the product of successive interactions and eventual merger of smaller, less massive galaxies. When galaxies collide or interact, gravitational forces can funnel gas towards their central regions, triggering or enhancing AGN activity. Studying such interactions is crucial to understand how galaxy dynamics influence black hole growth and AGN fueling mechanisms. These interactions also provide valuable insight into galactic and black holes co-evolution, a complex process that is still being investigated [White e Rees 1978, Somerville e Davé 2015].

1.1 GALAXY EVOLUTION

1.1.1 The Hierarchical model

To understand galactic evolution, and the role Active Galactic Nuclei (AGN) have on the process, we need to take a step back and explore the basics of cosmology. Cosmology as we have it today is the result of a century of observations, hypothesis and modeling, and it began when Albert Einstein used general relativity to create a relativistic universe model. Starting from Newtonian cosmology, where the universe is infinite, Einstein solved the field equations of gravity for a static, spatially closed, spherical, Universe with an

uniform distribution of matter, which required the addition of an extra term. This term was a constant sufficiently small to not affect the general relativity's success in predicting planetary motion, and determines the density of matter and the radius of cosmic space: the cosmological constant Λ [O'Raifeartaigh et al. 2017]. Around the same time, in 1917, Slipher found evidence of redshift in the spectra of spiral nebulae, indicating that they were moving away from us at velocities that range from 300 to 1000 km s^{-1}. This means that these objects could not be gravitationally bound to the Milky Way, and therefore, were outside our galaxy [Slipher 1917]. In 1929, based on observations of extragalactic nebulae, Edwin Hubble noticed the velocity–distance relation: the velocity of the receding nebula was linearly proportional to its distance [Hubble 1929]. This result is known as the Hubble law, $v = H_0 r$, where $H_0 = 71$ km s^{-1} Mpc^{-1} is the Hubble's constant and represents the rate at which the Universe is expanding.

In 1939, Fritz Zwicky studied the properties of extragalactic nebulae, particularly their motions and redshifts (translated by [Zwicky 2009])[1]. Focusing on the Coma Galaxy Cluster, he applied the virial theorem to estimate the total mass required to keep the cluster gravitationally bound. His analysis found that the average mass density of the system needed be at least 400 times larger that what was derived from observations of luminous matter. Based on this significant discrepancy, Zwicky proposed that non-luminous matter, or dark matter, must exist in far greater quantities than luminous, visible matter throughout the universe. The idea that galaxies are immersed in halos of dark matter was discussed in further detail in the 1970s, as analyses of observational data indicated that mass was missing from galaxies, which was consistent with Zwicky's hypothesis. This idea was further supported by a numerical study of the stability of galaxies [Ostriker e Peebles 1973], which showed that models including a spherical component (the halo) are more stable than those without. In 1978, White and Rees proposed a galaxy formation model where gas cools and condenses to form galaxies in the gravitational potential wells of the dark matter halos, which are the product of a hierarchical merging process [White e Rees 1978]. The discovery of Cosmic Microwave Background, in 1965, confirmed Lemaître's theory of the Big Bang, where the expansion of the Universe started from a hot dense state. Major developments were made in the 1980s, with the introduction of the theory of cosmological inflation by [Guth 1981] and [Linde 1982]. Around the same time, the CfA Redshift Survey [Davis et al. 1982], the first large scale 3D galaxy survey, was published, providing the first detailed view of the complex distribution of galaxies in the Universe. These cosmological structures were later called the "comic web". Since then, new data from a range of surveys and experiments helped shape the currently accepted standard model of cosmology: the ΛCDM model. Some of the important results came from the BOOMERanG experiment (Balloon Observations Of Millimetric Extragalactic Radiation

[1] Original paper: F. Zwicky, "Die Rotverschiebung von extragalaktischen Nebeln", Helv. Phys. Acta 6, 110–127 (1933). Reprinted with the original publisher's permission and translated by Anita Ehlers. More information available in the link https://link.springer.com/article/10.1007/s10714-008-0707-4.

And Geophysics, [Bernardis et al. 2000]), which showed that the universe's geometry is very close to flat, and large-scale structure surveys such as the Two-degree-Field Galaxy Redshift Survey (2dFFGRS, [Colless et al. 2001]), and Sloan Digital Sky Survey (SDSS). These surveys raised large amounts of data that have been used to test and prove models and theories to this day. In the ΛCDM model, the universe is dominated by cold dark matter, that is, non-relativistic matter that clusters under gravity, and dark energy, a component that drives the accelerated expansion of the universe. Dark energy, which only interacts through gravity, provides a scale for the cosmic acceleration and is represented by the cosmological constant Λ [Frenk e White 2012]. Observations of Type Ia supernovae by the Supernova Cosmology Project served as evidence of the existence of dark energy, and concluded that the Universe is accelerating [Goobar et al. 2000]. A natural outcome from the ΛCDM model is that galaxies form and evolve through an hierarchical merger process: smaller galaxies interact and merge into bigger, more massive galaxies, due to gravity.

Because light has a finite speed, it takes time for it to reach the Earth after it was emitted. When we observe far away galaxies, we are seeing them as they were in the past. Comparing observations of nearby galaxies with far away galaxies can help us trace an evolutionary path for these objects.

1.1.2 Galaxy formation

In the context of the hierarchical model that has been discussed until now, galaxies started to form in the early Universe, shortly after the Big Bang, when small density fluctuations in the dark matter field caused the collapse of dark matter halos. These halos acted as gravitational wells, attracting gas and leading to the formation of the first stars and proto-galaxies. Over time, proto-galaxies coalesced into larger, more massive galaxies. This merger process is responsible for galaxy growth and evolution [Somerville e Davé 2015]. Not only do mergers form larger galaxies, they also affect the history of their stars as the condensation of gas within galaxies creates stars. The nuclear fusion that happen inside the stars creates new elements, and as stars die, these elements are returned to the interstellar medium, where they can be used to create new stars. The initial phases of galaxy evolution were dominated by intense star formation, which peaked around redshift $z \sim 2$, when the Universe was around 3 billion years old. During this period, galaxies were rich in gas, and their star formation rates (SFRs) often exceed 100 $M_\odot$ year^{-1} [Barger et al. 1998,Madau e Dickinson 2014]. As the Universe aged, SFRs began to decline due to the exhaustion of gas available for star formation, and other environmental factors that prevent gas from cooling, such as feedback from massive stars that heat the ISM. Understanding how star formation rates change over time, through the study of star formation histories (SFHs), is essential to understand galaxy evolution.

In 1926, Edwin Hubble proposed a classification system for different types of galaxies based on their morphology: elliptical galaxies (E), normal spiral galaxies (S), barred spiral

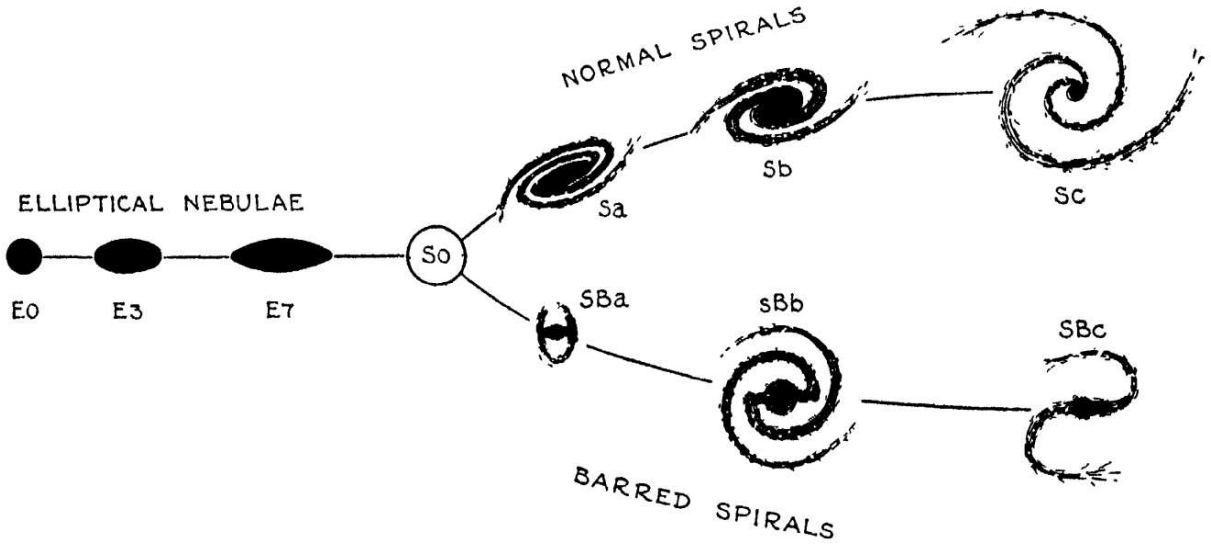

Figure 1 – Hubble Tuning Fork, taken from [Hubble 1936]. The horizontal branch represents elliptical galaxies (E0 to E7). The two branches to the right of the picture represent spiral galaxies. The one on top represents normal spirals (Sa to Sc), and the one on the bottom represents barred spiral (SBa to SBc). In the intersection is the lenticular galaxy type S0, an intermediate type between an elliptical and a spiral galaxy.

galaxies (SB), and irregular galaxies (Irr). Each class of galaxy except irregular galaxies has a subclassification to it, as can be seen in Figure 1. Elliptical galaxies can be classified from E0 to E6, depending on its ellipticity, E0 galaxies are very round, E6 galaxies have a very flat elliptical shape. Normal and barred (B) spiral galaxies can be classified by the shape of their arms. Sa and SBa present very tight arms and a prominent bulge, while Sc and SBc have a smaller bulge and less tight arms [Hubble 1926]. In 1936, he added lenticular galaxies (S0) to his classification system, known as Hubble Tuning Fork [Hubble 1936]. Hubble called elliptical and lenticular galaxies "early-type" galaxies, and spiral galaxies "late-type", although these terms are not based on evolutionary stages. In fact, elliptical galaxies are very massive galaxies formed when spiral galaxies merge, therefore, elliptical galaxies host older stars than spiral galaxies. This reflects into a bimodal distribution in galaxy properties, which surveys such as the SDSS have highlighted, such as color, morphology, and SFR. This bimodality becomes evident at a transitional stellar mass of 3×10^{10} $M_\odot$ [Kauffmann et al. 2003], indicating the presence of the two dominant galaxy types: star-forming (blue) spiral galaxies, which host young, massive stars, and quiescent (red) spheroidal or elliptical galaxies, which have already ceased star formation and are dominated by older stellar populations.

Multi-wavelength imaging and spectroscopy data indicate that galaxies have been growing in mass consistently over cosmic time [Madau e Dickinson 2014]. From $z \sim 4-2$, the number density of massive galaxies increases rapidly as galaxies merge ($\mathcal{M} > 10^{11}$ $M_\odot$). However, observations from $z \sim 2$ to present day show that this growth has slowed

considerably, with the number density of massive galaxies remaining relatively constant. In contrast, the number density of low-mass galaxies began rising more rapidly later, around $z \lesssim 1-2$. These observations suggest that massive galaxies formed earlier in cosmic history, growing their stellar masses, and then ceasing star formation relatively quickly. Meanwhile, low-mass galaxies evolved more recently, and are still forming stars [Muzzin et al. 2013, Marchesini et al. 2009, Moustakas et al. 2013]. As a direct consequence, massive galaxies host the oldest stars, a phenomenon called archaeological downsizing. At first, archaeological downsizing seems to go against the hierarchical model, since it predicts that the dark matter halos collapse and merge over time into more massive structures, which should apply to galaxies as well. However, while older stars originally formed in smaller galaxies, those galaxies later merged to form the massive systems we observe today.

Galaxy mergers are powerful processes that trigger star formation, severely impacting the SFR of the galaxies involved [Larson e Tinsley 1978, Yee e Ellingson 1995, Kennicutt, Barton, Geller e Kenyon 2000]. Theoretical and numerical studies have shown that, during the merger process, gravitational torques cause gas to lose angular momentum, which results it to fall towards the center of the galaxie [HERNQUIST 1989]. The efficiency in which this process happens not only depends on the individual characteristics of the galaxies involved, and in the gas present on them, but also on the characteristics of the merger itself [Lambas et al. 2012, Pan et al. 2019].

Both observational and theoretical works have shown that in the center of most galaxies resides a supermassive black hole (SMBH) [Kormendy e Richstone 1995], so it is essential that we study their evolution as well. Black holes are predicted by General Relativity, from the Einstein's equations 1.1, which encode the curvature of space-time into the Einstein tensor $G_{\mu\nu}$ in terms of the stress-energy tensor $T_{\mu\nu}$, which describes the distribution of energy, and consequently, matter, Newton's gravitational constant G and the speed of light c [Einstein 1916]:

$$G_{\mu\nu} = \frac{8\pi G}{c^4} T_{\mu\nu}. \tag{1.1}$$

Karl Schwarzschild solved the Einstein's field equations for a spherical mass without angular momentum in 1916 (translated [Schwarzschild 1999]), a solution called Schwarzschild metric. The metric tells matter how to move according to the distortion (the curvature) it causes in the fabric of spacetime. Schwarzchild's metric, specifically, describes the gravitational field outside the spherical mass, and predicts a spacetime singularity at the center of the system, when $r = 0$. One of the parameters of Schwarzchild's metric is the Schwarzchild's radius, a scale factor related to the mass M, and is the radius of a spherical surface in which the escape velocity is higher than the speed of light. Every particle that crosses the Schwarzchild's inevitably falls into the singularity. If all of the mass of a body is inside its Schwarzschild's radius, we call this body a black hole. The Schwarzschild's radius form its event horizon and is given by equation 1.2, where G is the

gravitational constant and c is the speed of light:

$$r_s = \frac{2MG}{c^2}. \tag{1.2}$$

The collapse of a massive star, under the right conditions, could lead to the formation of a black hole. In 1965, Penrose demonstrated that the Schwarzschild's radius delimits a spherical region called trapped region, where light rays converge inwards, and a spacetime singularity inevitably forms [Penrose 1965]. It wasn't until 1972, however, that a black hole was observed, proving their existence [Bolton 1972, Webster e Murdin 1972]. Observations of the binary system HDE 226868 = Cygnus X-1 showed strong X-ray emissions coming from a compact source, Cygnus X-1, the black hole, due to the accretion of mass coming from stellar winds of its blue supergiant variable star companion HDE 226868 [Gies e Bolton 1986]. While stellar-mass black holes (BH), with mass ranging from $\sim$ 3–100$M_\odot$, are thought to form from the collapse of massive stars, the origins of SMBHs, with masses $> 10^6$ $M_\odot$, are still not known [Volonteri, Habouzit e Colpi 2021]. One possible explanation is the collapse of population III stars, supermassive stars with mass up to 200 $M_\odot$ that formed in the begining of the universe from primordial gas clouds. These stars then collapsed into SMBH with mass of around 100 $M_\odot$ [Madau e Rees 2001].

BH growth can happen through two processes, accretion of falling matter during the AGN phase [Shakura e Sunyaev 1973], and SMBH mergers [Antonini, Gieles e Gualandris 2019]. When galaxies merge, so do their central SMBHs. As the interaction happens, the evolution of the interacting SMBH progresses through three stages, from its formation to eventual merger. First, as the galaxies merge, the SMBHs spiral inward and form a binary system. They orbit each other closer and closer, and the gravitational torques from surrounding objects can cause the orbit of the SMBH binary to decay even further. As a result, an accretion disk may form, structure present in almost all types of AGN, irradiating large amounts of energy as it falls into the SMBHs. When the SMBH is accreting mass, we call it an active galactic nucleus. In later stages of the galaxy merger, at small enough separations, the system starts to rapidly lose energy in the form of gravitational waves, and the SMHB binary finally merge [Begelman, Blandford e Rees 1980]. This means that the evolution of SMBHs is intrinsically connected to the evolution of its host galaxy.

1.2 ACTIVE GALACTIC NUCLEI

The term Active Galactic Nuclei (AGN) refers to the existence of highly energetic phenomena happening in the central region of its host galaxy which cannot be attributed to star formation. For an AGN, the energy emitted by the nucleus can be comparable or sometimes even surpass the energy emitted by all the stars present in the galaxy combined. In their spectra, the presence of broad emission lines suggests that gas is moving around the nuclear region at high speeds, being photoionized by a hard source that emits UV and X-ray photons.

1.2.1 Historical Overview

Early 20th century observations found strong resolved emission lines present in spiral nebulae, later identified as galaxies, that were several angstroms wide [Fath 1909, Slipher 1917]. Carl Seyfert was the one who identified a new class of galaxies, later called Seyfert galaxies, through a systematic analysis in 1943 [Seyfert]. The emission lines in the spectra of the observed galaxies appeared broadened, assumed to be due to the Doppler effect caused by the high velocities of the gas. For this reason, the widths of these lines are measured in kilometers per second (km s^{-1}).

From the twelve galaxies known to exhibit high-excitation nuclear emission lines at the time, ten were either early or intermediate type spiral galaxies, and the remaining two could be classified as either peculiar elliptical or irregular galaxies. Other common features of these galaxies were their high luminosity nuclei, and the fact that the average of their absolute magnitudes were brighter than those of typical spiral galaxies without nuclear activity. Seyfert studied the spectra of the galaxies NGC 1068, NGC 3516, NGC 4051, NGC 4151 and NGC 7469, six of the brightest known galaxies showing emission bands in their nuclei at the time. He found that the nuclei of these galaxies had an extremely high surface brightness and spectra dominated by emission lines of very high excitation. All of them presented broadening of hydrogen emission lines. Some of these galaxies, like NGC 3516 and NGC 7469 had the total width of hydrogen lines up to 8500 km s^{-1}, while galaxies like NGC 4151 had more narrow lines, with total widths up to 7500 km s^{-1}. Seyfert measured the Doppler broadening using the total width of the emission lines, that is, the full extent of the line from one end to the other from where it differs from the continuum, rather than using a standardized metric like the full width at half maximum (FWHM). This approach captured the broadest velocity components present but made comparisons between different objects or studies less precise. In the 1950's, AGNs continued to be studied in the radio band. Several radio surveys were conducted, such as the Third Cambridge survey (3C) [Edge et al. 1959].

In 1963, Schmidt discovered that the emission lines of the galaxy 3C 273 were dislocated by redshift [Schmidt 1963], which was attributed to the expansion of the universe [Greenstein e Schmidt 1964]. Since the optical source had not been resolved but appeared point-like, this object, and the ones identified subsequently, were classified as QSRs (quasi-stellar radio sources), or quasars. Although AGNs were first identified due to their strong radio emissions, they emit across the entire electromagnetic spectrum, ranging from radio waves to X-rays, and in some cases, even gamma rays. The main difference between Quasars and Seyfert galaxies is the amount of radiation emitted by the compact central source; a typical nucleus of a Seyfert galaxy has a bolometric luminosity of $L_{bol} > 10^{42}$ erg/s, which is comparable to the emission of all stars present in the host galaxy, while quasar nuclei outshine the starlight of their host galaxies, with $L_{bol} > 10^{45}$ erg/s [Blandford, Meier e Readhead 2019].

1.2.2 Unified model

Over the past decades, our understanding of AGN has grown significantly, as technology advances made computer simulation and modeling more efficient, as well as better instruments and detectors. Since AGN emissions cover the entire electromagnetic spectrum, multiple surveys collecting data at different wavelengths have aided in the detection and classification of these objects, such as the Sloan Digital Sky Survey (SDSS [York et al. 2000]) in the optical band. Due to the instrumental limitation of the time when these objects began to be investigated, AGN classification was divided into two categories based on their radio emissions. Galaxies with faint radio emissions were called radio-quiet AGN, while those with strong radio emissions were called radio-loud AGN. Over the years, as more AGN were being discovered, different classifications were created based on the difference in their spectral features, radio emissions, redshift, brightness. One of the dominant characteristics of AGNs is the presence of Doppler-broadened emission lines in their spectra. AGNs are classified as type 1 and type 2 depending on the presence or absence of broad components in the emission lines of the hydrogen Balmer series, in their optical spectra, characterized by their full width at half maximum (FWHM). Broad lines (FWMH$\geq$ 2000 km s^{-1}), are produced in the broad line region (BLR), located near the SMBH. Depending on the orientation of the system with respect to our line of sight, the BLR can be obscured, resulting in a spectrum that shows only narrow lines (FWMH$<$ 1000 km s^{-1}). These narrow lines, on the other hand, are produced in the narrow line region (NLR), which lies farther from the nucleus and can extend from $\sim$ 10 pc to $\sim$ 1 kpc.

In 1979, Stockman, Angel and Miley made a significant discovery when they found that, in a sample of quasars, the position angle of optical polarization was strongly correlated with the position angle of the quasars' extended radio structures [Stockman, Angel e Miley 1979]. This indicates that quasars maintain a long-term direction memory, and, more importantly, suggests the presence of a common underlying structure that dictates their observable features. The discovery of a highly polarized Hα broad component in the radio galaxy 3C 234, oriented at a position angle perpendicular to the radio axis [Antonucci 1984], along with observations of NGC 1068 in polarized light [Antonucci e Miller 1985] where the polarization was found to result from scattered electrons, showed that both had very high wavelength-independent continuum polarization. For NGC 1068, the polarized spectrum resembled that of a Seyfert type 1 galaxy; however, observation in unpolarized light shows the spectrum of a Seyfert type 2. To explain these differences, they proposed that the BLR is surrounded by an opaque structure. In this case, photons coming from the accretion disk are scattered by free electrons surrounding it, and are reflected on the surface of this structure, which causes the polarization. This led to the development of the unified model [Antonucci 1993].

Figure 2 illustrates the current understanding of the unified model. The main AGN

structures are seen along the equatorial and polar direction, and an estimative of distances is presented. In the center of the AGN lies a SMBH surrounded by an accretion disk and a corona of hot electrons. Gas clouds above and below the accretion disk form the BLR, a sub-pc scale dust-free region. The lines produced in the BLR are assumed to be Doppler-broadened, where the proximity to the SMBH causes the gas to orbit it at velocities up to 10^5 km s^{-1}. Parallel to the disk is the torus, a structure made of dust that can obscure the emission coming from the BLR, and it is not always aligned to the galaxy's plane. The relative angle with the line of sight determines if broad emission lines are seen on the spectrum or not. If the torus is seen edge-on, the BLR is obscured, and we classify those as type-2 AGN. If the torus is face-on, the BLR is visible (type-1 AGN). Perpendicular to the accretion disk, relativistic jets can generate radio emissions due to synchrotron radiation. Farther away from the nucleus is the NLR. The density of the NLR is low enough that the spectrum presents forbidden emission lines ($\sim 10^8$ cm^{-3}). The most prominent forbidden emission lines seen are [O III] λ4959, 5007, [N II] λ6584, 6584, and [S II] λ6717, 6731. Since this region is farther from the SMBH, the velocity of the gas is not as high, usually as high as 1000 km s^{-1}. Seyfert galaxies follow the same classification for type 1 and type 2 AGNs. To put the compact nature of an AGN into perspective, the accretion disk and BLR could fit within our own solar system. If the supermassive black hole (SMBH) were positioned where the Sun is, the outer boundary of the BLR would extend to the Oort Cloud, roughly 3.2 lightyears away.

While most of the optical and UV continuum emission detected is emitted by the accretion disk, a significant portion of these high energy photons are reprocessed. If the photon interacts with the electrons present in the hot corona, they are up-scattered in the X-ray band, illuminating the surrounding gas. However, if the photon is reprocessed by dust in the torus, and is absorbed, it is later re-emitted in the infrared band. The torus can also collimate the radiation, forming ionization cones, bi-conical shaped structures. X-ray emission is a common feature in AGN spectra, and its study provides valuable insights into the structure and physical characteristics of the material surrounding the nucleus. We parametrize the level of ionization through absorption of X-rays using the line-of-sight column density (N_H). When $N_H \geq 10^{22}$ cm^{-2}, the AGN is obscured [Almeida e Ricci 2017]. However, it is still possible to detect AGNs through X-ray emission even when obscured. X-rays can be divided into two categories according to the produced photon's energy: soft X-rays, with energy ranging from 0.5 keV to 2 keV and hard X-rays, with energy ranging from 2 keV to 8 keV. Hard X-rays are able to penetrate column densities up to $N_H > 10^{24}$ cm^{-2} [Barger et al. 2002], while the flux of soft X-rays is depleted due to photo-electric effect [Almeida e Ricci 2017].

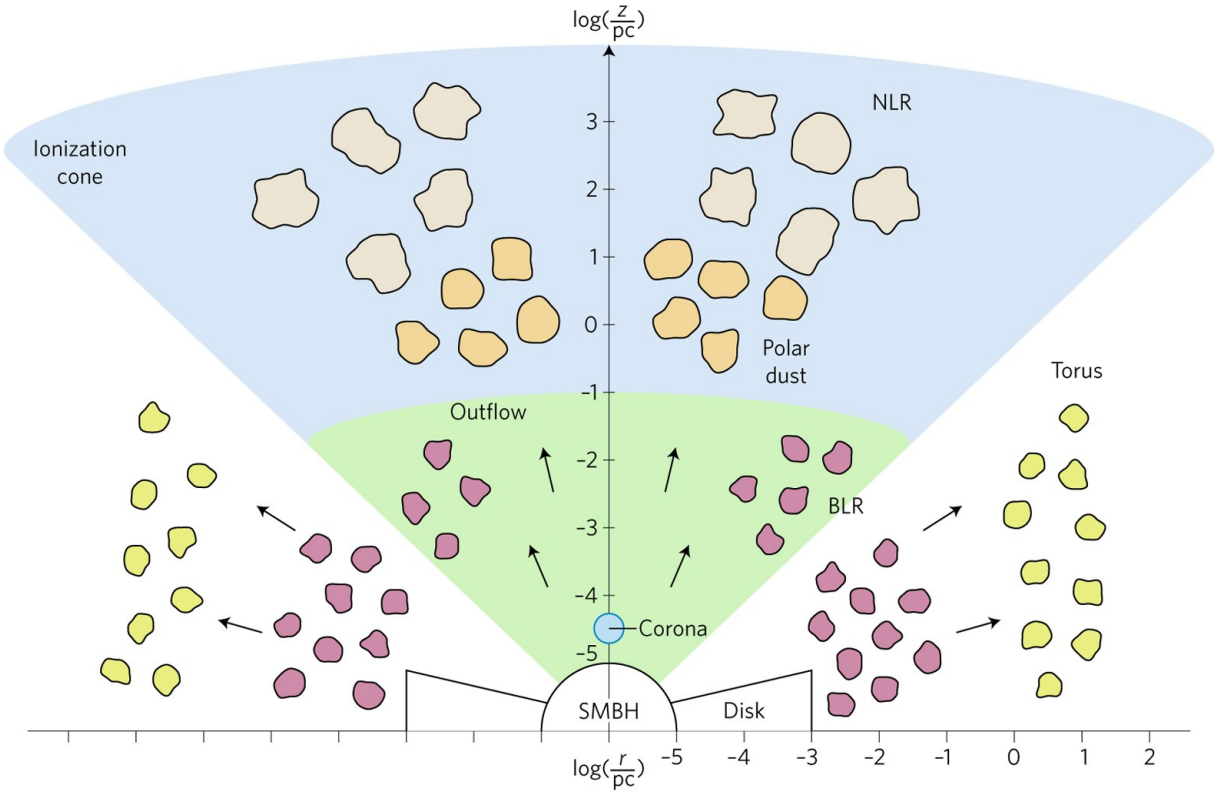

Figure 2 – Sketch of the main AGN structures seen along the equatorial and polar direction. From the center to host-galaxy scales: SMBH, accretion disk and corona, BLR, torus and NLR. Different colors indicate different compositions or densities. Image taken from [Almeida e Ricci 2017].

1.2.3 AGN selection and classification

Photoionization occurs when a photon interacts with an atom or ion and is absorbed. If the energy of this photon is sufficient to overcome the binding energy of the electrons, they can be ejected from their orbits. When this happens, we say that the atom is ionized.

In order to identify which ionizing sources are responsible for the emission lines present in the spectrum there needs to be a quantitative classification system capable of providing a direct and reliable measure of the dominant excitation mechanism acting upon the gas. We use two methods based on the relative strengths of the emission lines present in the spectrum,the Baldwin-Philips-Terlevich (BPT) diagram [Baldwin, Phillips e Terlevich 1981] and the $W_{\mathrm{H}\alpha}$ versus [N II]/Hα (WHAN) diagram [Fernandes et al. 2011]. They are detailed in the following sections.

1.2.3.1 BPT Diagram

Emission lines can be detected in the spectra of AGN host galaxies due to high energy emissions coming from it. However, we can see emission lines in the spectra of other galaxies and objects that don't host an AGN, like planetary nebulae, ionized by supernovae, and H II regions, gas clouds that are ionized by O and B massive stars. In 1981 Baldwin,

Phillips & Terlevich conducted a very detailed study of excitation mechanisms, trying to find a good system based on strong forbidden emission lines in the optical range [Baldwin, Phillips e Terlevich 1981]. They classified the strongest emission lines into groups according to their predominant excitation mechanisms: normal H II regions, giant regions of gas being ionized by massive O and B stars; power-law ionization, usually powered AGNs; and shock wave heating. It was known that H II regions could be classified using ([O III] λ5007 /Hβ λ4861) or ([O III] λ3727 / [O III] λ5007) intensity ratios, but power-law and shock-wave heating ionization can't be well represented by these. So they proposed a two-parameter classification system that could better separate the three groups by plotting the following emission line ratios: ([N II] λ6584 /Hα λ6563) vs ([O III] λ5007 /Hβ λ4861), and ([O II] λ3727 /[O III] λ5007) vs ([O III] λ5007 /Hβ λ4861), ([N II] λ6584 /Hα λ6563) or ([O I] λ6300 /Hα λ6563).

In 2001, Kewley et al. modeled a large sample of infrared starburst galaxies to find a theoretical upper limit for photoionization caused only by massive stars [Kewley et al. 2001]. They used two stellar population synthesis models, whose main difference was the stellar evolutionary tracks and stellar atmosphere models, to generate the SED of young star clusters. All points above this curve need photoionizing sources harder than massive stars. But because the SEDs for massive stars were too hard, their data differs from observation. They used a rectangular hyperbola to parametrize a dividing line between the theoretical starburst region from objects that are photoionized by other mechanisms:

$$\log\left(\frac{[\text{O III}]\lambda5007}{\text{H}\beta}\right) = \frac{0.61}{\log([\text{N II}]/\text{H}\alpha) - 0.47} + 1.19, \tag{1.3}$$

$$\log\left(\frac{[\text{O III}]\lambda5007}{\text{H}\beta}\right) = \frac{0.72}{\log([\text{S II}]\lambda6717/\text{H}\alpha) - 0.32} + 1.30, \tag{1.4}$$

$$\log\left(\frac{[\text{O III}]\lambda5007}{\text{H}\beta}\right) = \frac{0.73}{\log([\text{O II}]\lambda6300/\text{H}\alpha) - 0.59} + 1.33. \tag{1.5}$$

Based on the available data from SDSS, Kauffmann et al. selected galaxies whose four emission lines had $S/N > 3$ to study the properties of AGN host galaxies and how they compare to non-active galaxies [Kauffmann et al. 2003]. Their observations consisted in a 3-arcsecond circular region centered on each galaxy. Because some galaxies were farther away than others, the data is mixed with light coming from a small region of somewhat close galaxies, and a bigger region (that could envelop the whole galaxy) of far away galaxies. When plotting the BPT diagnostic diagram, they noticed that the galaxies were distributed across the diagram in such a way that they formed two branches, and tried to trace a dividing curve to separate ionization by stars or AGN. In this case, any points that fell below their line could be explained solely by stellar photoionization. Anything above that would need a harder radiation field to explain the photoionization, such as collisions, or AGN radiation. There has been a discussion around the existence of "transition" objects, galaxies with low luminosity, and said to have intermediate emission line properties. With this in mind, some would hypothesize that the points in the region

under the Kauffmann2003 (Ka03) line were pure starbursts, points in the region between Ka03 and Kewley2001 (Ke01) would be a mixture starburst and AGN, and points above the Ke01 line were pure AGN, that is, most of the ionization is due to AGNs. This is, however, not true. They shifted Kewley's line to try to match the data from SDSS.

Stasinska et. al analyzed a set of 20,000 galaxies extracted from the SDSS, and tried to explain why, when plotted in a BPT diagram, the data formed the shape of the wings of a seagull [Stasinska et al. 2006]. It happens because when the metallicities of these galaxies are larger than 0.3 $Z_{\odot}$, the N/O ratio increases with O/H, forming the left wing, which represents the branch of Normal Star Forming (NSF) galaxies, while the right wing is formed by galaxies hosting AGNs.

They proposed that the best divisor line between NSF galaxies and AGN host galaxies in the BPT diagram is as follows:

$$y = (-30.787 + 1.1358 + 0.27297x^2)\tanh(5.7409x) - 31.093, \tag{1.6}$$

where $y = \log([\text{O III}]/\text{H}\beta)$ and $x = \log([\text{N II}]/\text{H}\alpha)$. If [O III]/H$\beta$ is not available, x can be change to $x = -0.4$.

Kewley et al. then conducted an empirical analysis in 2006, using SDSS data [Kewley et al. 2006], and concluded that almost every Low-Ionization Nuclear Emission-line Region (LINER) galaxy hosts an AGN, and the most notable difference between LINERs and Seyferts is the accretion rate. However, due to their S/N selection, they missed a huge population of retired galaxies that have LINER-like spectra [Stasińska et al. 2008]. Based on this, they were able to classify these objects with the emission-line ratios [O I]/Hα and [S II]/Hα, both plotted against [O III]/Hβ.

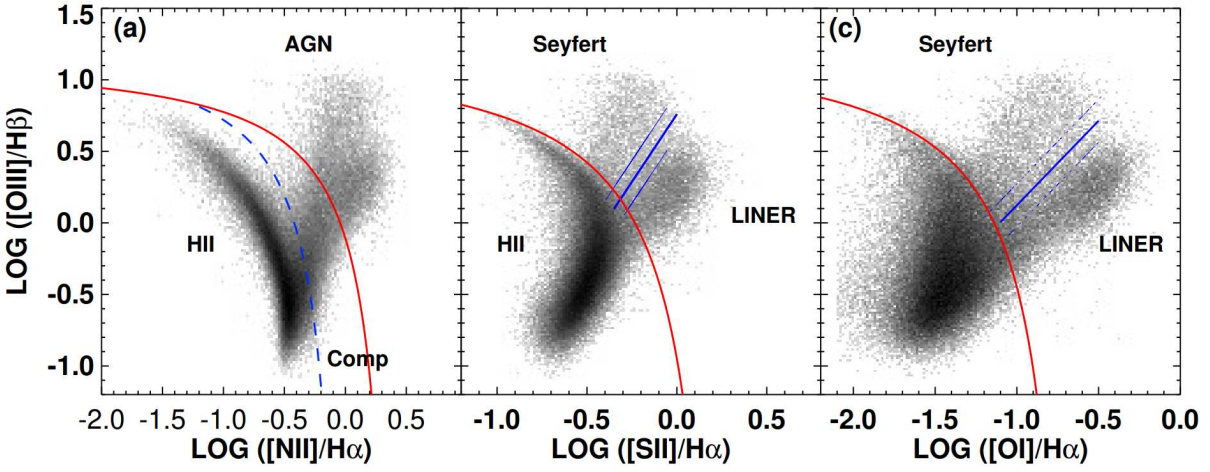

Figure 3 – (a) The [N II]/Hα vs [O III]/Hβ diagram for SDSS galaxies with S/N $>$ 3. The Kewley et al. (2001a) "extreme starburst" line and the Kauffmann et al. (2003a) classification line are shown as solid and dashed lines respectively. (b) The [S II]/Hα vs [O III]/Hβ diagram, (c) The [OI]/Hα vs [O III]/Hβ diagram. Figure taken from [Kewley et al. 2006].

1.2.3.2 WHAN diagram

Using emission line ratios as a classification system has proved to be effective in classifying AGN photoionization. However, in certain cases, not all lines needed are available in the spectrum, such as in weak-line galaxies. To address this, Cid Fernandes et al. introduced the $W_{\mathrm{H}\alpha}$ versus [N II]/Hα (WHAN) diagram [Fernandes et al. 2011]. One of the advantages of WHAN is its ability to distinguish between two overlapping classes in the low-ionization nuclear emission-line region (LINER) region of traditional diagnostic diagrams: weakly active galactic nucleus (wAGN) and "retired" galaxies (RGs), the latter being galaxies that have ceased star formation and are ionized by their hot, low-mass evolved stars (HOLMES). An useful classification criterion is ξ, which measures the ratio of the extinction-corrected Hα luminosity to the Hα luminosity expected from photoionization by stellar populations older than 10^8 yr. However, the Hα equivalent width $W_{\mathrm{H}\alpha}$ is a more accessible, and model-independent quantity, making it a better option.

The WHAN diagram only requires two emission lines: Hα and [N II], which are typically very prominent. We plot $W_{\mathrm{H}\alpha}$ versus the [N II]/Hα to construct it. $W_{\mathrm{H}\alpha}$ has a bimodal distribution that can help to distinguish between strong and weak AGN (Seyferts) and "fake" AGNs (RGs), with the practical division set as $W_{\mathrm{H}\alpha} = 3$ Å. The WHAN diagram plot, shown in Figure 4 and sourced from [Fernandes et al. 2011], displays and labels the five regions corresponding to the four distinct classes of galaxies identified in it, which are as follows:

- pure star-forming galaxies: $\log$ [N II]/H$\alpha < -0.4$ and $W_{\mathrm{H}\alpha} > 3$Å;
- strong AGN (sAGN): $\log$ [N II]/H$\alpha < -0.4$ and $W_{\mathrm{H}\alpha} > 6$Å;
- weak AGN (wAGN): $\log$ [N II]/H$\alpha < -0.4$ and 3Å $> W_{\mathrm{H}\alpha} > 6$Å;
- passive galaxies: $W_{\mathrm{H}\alpha}$ and $W_{[\mathrm{N\ II}]} < 0.5$Å[2].

[2] This division is, however, no longer used.

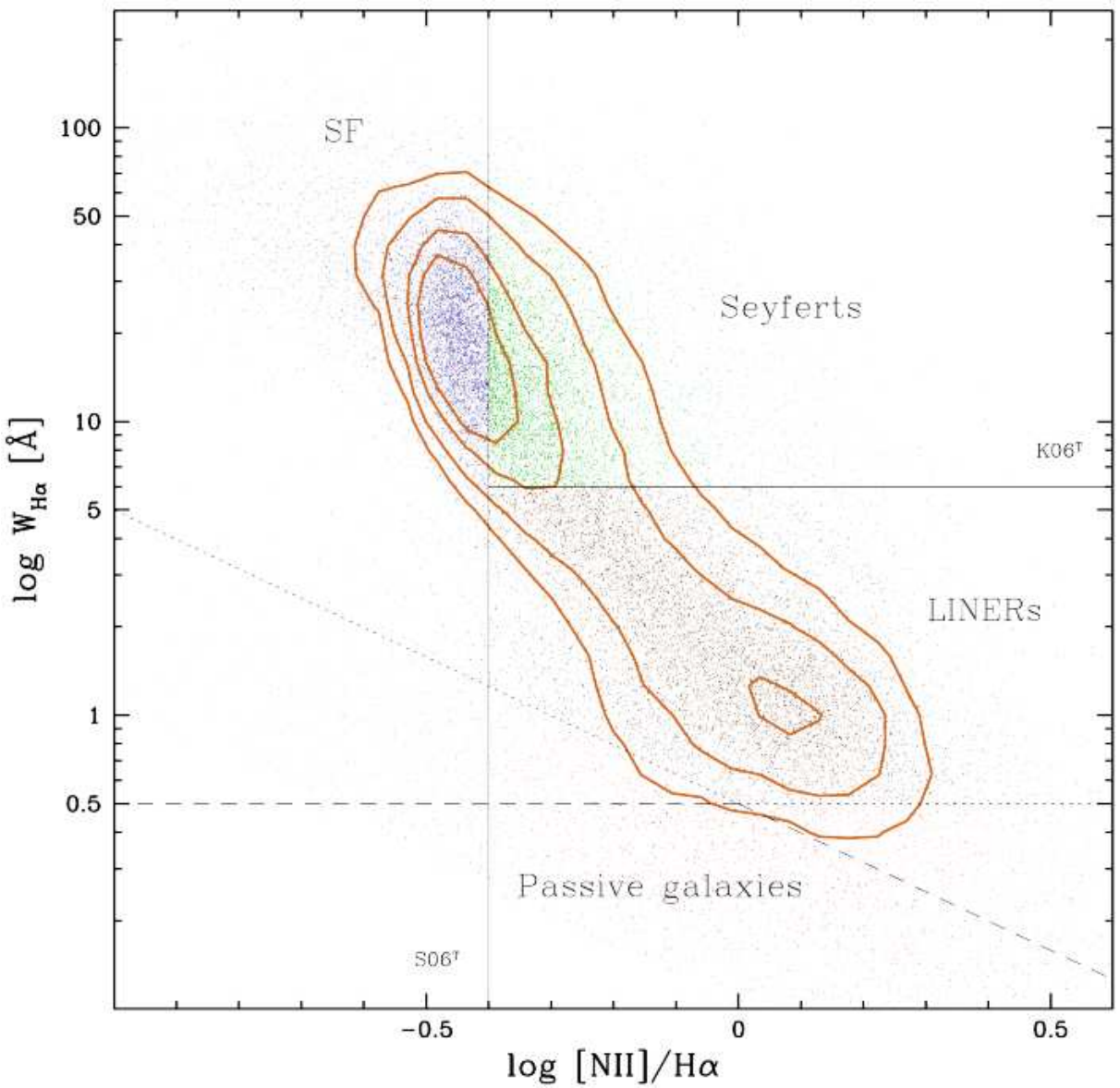

Figure 4 – The WHAN diagram, taken from [Fernandes et al. 2011]. The line labelled S06T represents the optimal transposition of the SF/AGN spectral classification scheme from [Stasinska et al. 2006], while the line at $W_{\mathrm{H}\alpha} = 6$Å represents Seyfert/LINER division by [Kewley et al. 2006]. The dotted lines at $W_{\mathrm{H}\alpha} < 0.5$Å and $W_{[\mathrm{N\ II}]} < 0.5$Å mark the measurements limits.

1.2.4 Dual AGNs

Dual AGNs are formed by pairs of interacting galaxies whose SMBHs are accreting matter. For pairs that have a nuclear separation of $\lesssim 10$ kpc, simulations predict that late-stage mergers are responsible for black hole growth during the AGN stage [Hopkins et al. 2008]. The dual AGNs are predicted to be obscured by gas and dust due to the interaction, which leads to emissions in the mid-infrared band [Blecha et al. 2018]. These results are backed by observational studies that have found that late-stage mergers, and post-merger galaxies are more obscured by dust and gas than isolated AGNs. In this case, obscured AGNs in mergers can be identified more easily using mid-infrared detections than in the optical band [Satyapal et al. 2014, Ellison et al. 2019, Weston et al. 2017]. Unfortunately, despite decades of observations and theoretical works predicting the existence of dual AGNs, they are rare. Few dual AGNs have been observed with projected separation of < 10 kpc [Satyapal et al. 2017]. This scarcity highlights the necessity of better and more efficient selection methods for these objects, since most of them have been found by accident.

Selecting dual AGNs is challenging for several reasons. Projected separations don't always represent the true physical separation between the SMBHs in dual systems. In cases where the separation is artificially smaller, this projection can result in the system being incorrectly classified as being at a more advanced merger stage than it truly is. That is why high-resolution imaging is essential in the selection of dual AGNs, as it provides more accurate measurements, even at high redshifts. While detections can be made in the IR, optical, X-ray and radio bands, the specific configurations of each system can heavily impact detections. For instance, optical emissions can be obscured by dust surrounding the nuclei, resulting in the non-detection in this band, although X-ray emissions may still be detectable. To overcome this problem, Satyapal et al. and Pfeifle et al. selected SDSS late-stage mergers galaxies and cross-matched their optical images with mid-infrared observations from the Wide-Field Infrared Survey Explorer (WISE) all-sky survey [Satyapal et al. 2017, Pfeifle et al. 2019a]. They followed up with X-ray detections from Chandra X-ray Observatory and were able to identify the presence of dual AGNs in the majority of the interacting galaxies in the sample. Among the sample was the triple merger SDSS J084905.51+111447.2.

Dual AGNs can take a long time to merge if they stall in a stable orbit, in timescales that exceed the age of the Universe. However, a third SMBH can speed up this process [Hoffman e Loeb 2007]. Cosmological simulations show that $\sim 16\%$ of all binary BH will interact with a third before total coalescence [Pfeifle et al. 2019b].

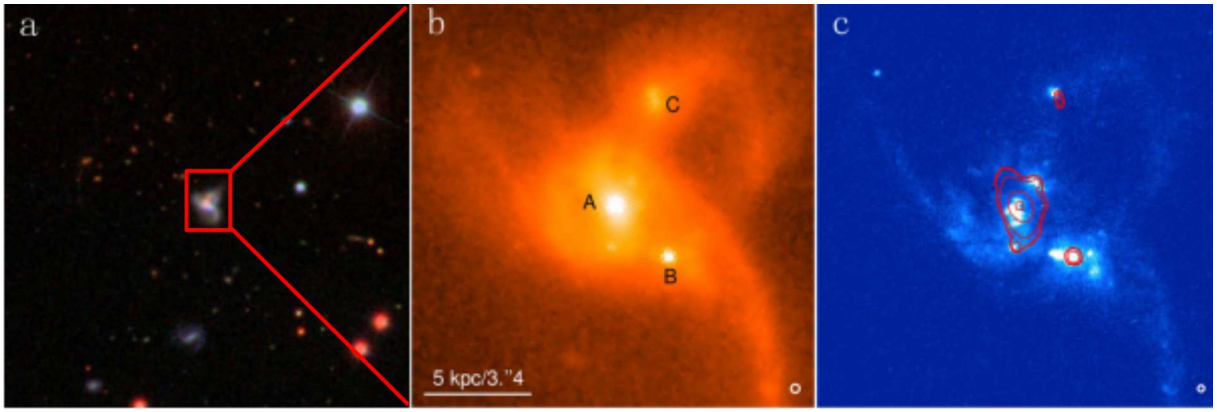

Figure 5 – Optical and near-IR images of SDSSJ0849 from [Liu et al. 2019] are presented. In panel (a) is the 200″ × 200″ field of view SDSS gri-color composite image of the galaxy. Panels (b) and (c) show HST/WFC3 images in the IR/F105W (Y) and UVIS/F336W (U) bands. The circles at the bottom indicate the HST point-spread function (PSF) sizes.

1.3 THE SCIENCE OBJECT: SDSSJ0849+1114

SDSSJ0849+1114, at redshift $z = 0.078$, is a trio of interacting galaxies that caught our attention due to its rarity, since $\lesssim 2\%$ of major mergers involve three galaxies [Darg et al. 2011]. The system is made of three spiral galaxies in the late stages of merger [Pfeifle et al. 2019a, Pfeifle et al. 2019b]. SDSS J0849+1114, which will be referred to as simply SDSSJ0849, was identified in multiple surveys for dual AGNs in the optical, X-ray, and radio bands [Liu et al. 2011, Foord et al. 2021, Liu et al. 2019]. Liu et al. conducted a detailed multi-wavelength analysis including Chandra X-ray imaging spectroscopy, HST U and Y band imaging, VLA radio imaging, and spatially resolved optical spectroscopy. From the BPT diagram, they classified all three nuclei as Seyfert type-2, which makes SDSSJ0849 the first known triple Seyfert type-2 nucleus. In 2019, Pfeifle et al. used high-spatial resolution X-ray, near-IR and optical spectroscopic diagnostics to study SDSSJ0849 [Pfeifle et al. 2019b]. They confirmed that the system is in a late stage of its merger, a result that agrees with their previous work earlier that year [Pfeifle et al. 2019a], based on the morphology of the system, which exhibits strong tidal features, and hard X-ray spectral fitting, which reveals a high column density along the line of sight. They estimate the nuclear pair projected separations of 3.4 kpc between nucleus A and nucleus B, 5.3 kpc between nucleus A and nucleus C, and 7.3 kpc between nucleus B and nucleus C. Chandra observations showed X-ray source points that cannot be explained by star contributions. In 2021, Foord et al. further confirmed these emissions, confirming the triple AGN system [Foord et al. 2021].

In 2022, Peng et al. presented new high-resolution, multi-band VLA radio imaging observations of SDSSJ0849 at 3.0, 6.0, 10.0, and 15.0 GHz, providing an unprecedented radio view of the system, when nucleus A and nucleus C were detected for the first time at

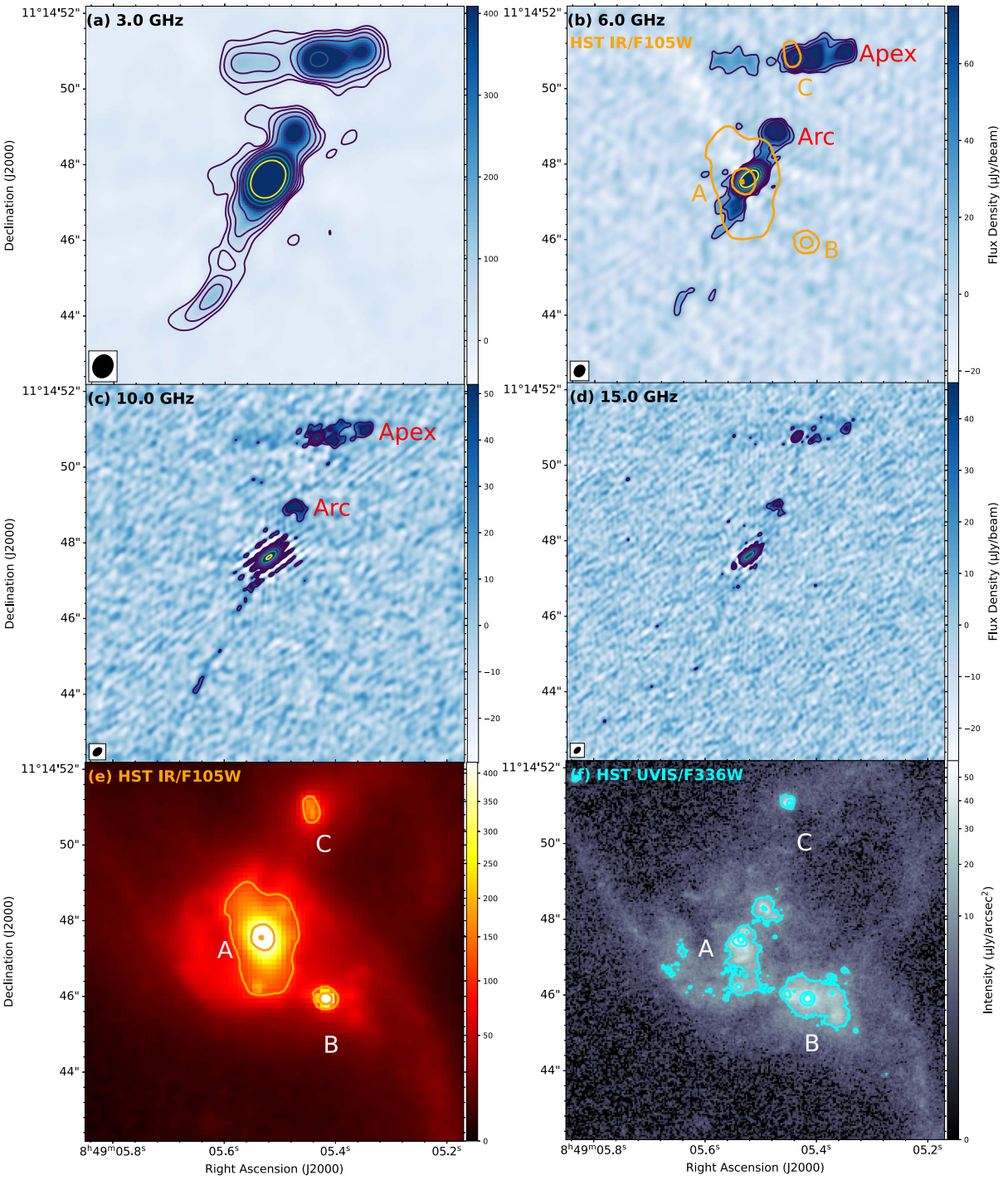

Figure 6 – VLA and HST images of SDSSJ0849 from [Peng et al. 2022]. Panels (a) to (d) show the radio images at 3.0, 6.0, 10.0, and 15.0 GHz frequencies. At the lower-left corner of these panels is indicated the radio synthesized beam. The purple to yellow contours are at levels of (4, 8, 16, 32, 64, 128, 256, 512) × RMS, which is 5, 5, 7, and 6 μ Jy beam^{-1} at 3, 6, 10, and 15 GHz. In panel (b) the orange contours indicate the optical positions of the three nuclei. Panels (c) and (d) reveal the extended radio features. Panels (e) and (f) are HST/WFC3 IR/F105W (Y-band) and UVIS/F336W (U-band) images.

3.0, 6.0, and 15.0 GHz, emissions consistent with synchrotron radiation [Peng et al. 2022]. By analyzing the high-resolution images, they have also found extended features for both nuclei, which they attributed to AGN-driven jets and outflows. Nucleus A presents an inner jet pointing in the southeast-northwest direction at a position angle of $\sim -53°$, and extends to 0.6 arcsec, or 0.9 kpc. However, the outer jets show a change of 20° deviation from the inner jet, which suggests that the SMBH at the center of the nucleus is spinning and the emission of jets is episodic. Nucleus C also presents jets, but it also presents a radio lobe that has a length of $\sim$ 1.5 arcsec, or 2.2 kpc, and width of $\sim$ 0.6 arcsec, or $\sim$ 0.9 kpc. Nucleus B, however, did not present emissions in any of the four frequencies.

The data used for the present work came from the MUSE proposal Program ID:109.238W.009 0109.B-0871(I), which was submitted by our research group. In this work, we conduct an in depth analysis of SDSSJ0849 emission lines based on Integral Field Spectroscopy (IFS) hoping to better understand the merging process. We focus in the kinematics of the gas and the stars. We assumed the standard cosmology of $H_0 = 70\text{km s}^{-1}$ Mpc^{-1} of the Hubble constant, $\Omega_M = 0.3$ for the matter density parameter and $\Omega_\Lambda = 0.7$ for the effective mass density of the dark energy.

1.4 DISSERTATION OUTLINE

This dissertation began with a brief historical introduction. We then delved into what an AGN is, represented by the unified model, and the impact that the presence of an active nucleus has on the host galaxy. We also covered the role of mergers in galactic evolution and the methods for classifying AGN. In Chapter 2, we will detail the processes of data reduction and selection used, the techniques employed, and their justifications. We also report some difficulties we encountered during this process and how we overcame them. Chapter 3 presents the results we obtained and their discussions. The results aim to provide a better understanding of how this galaxy is evolving. We analyzed the stellar populations, determining their ages and metallicities and kinematic dynamics. We also analyzed the gas present in the galaxy, and, together with the stellar population results, we were able to determine the kinematic dynamics of the galaxy as a whole. From the analysis of the emission lines, we determined the photoionization mechanisms and other characteristics of the AGN. Finally, Chapter 4 presents our conclusions.

2 METHODOLOGY AND TECHNIQUES EMPLOYED

To obtain the results reported, we have used various data analysis techniques and tools, starting by attesting the quality of our data. We filtered the data by isolating the interacting system in the data cube, reducing the size of the grid from 60×60 arcsecs to 20×20 arcsecs, in order to optimize the computational process. We then had to prepare the data before running analysis scripts and other software. In this chapter, we detailed these procedures, along with the scientific justification for why they were chosen. The science image reduction was done by ESO using the ESO Data Reduction Pipelines and Workflow Systems. Aside from that, all of the results here listed were done by me (unless specified), but the conclusions taken from them were a combined effort between me and Prof. Daniel.

2.1 INTEGRAL FIELD SPECTROSCOPY (IFS)

Integral Field Spectroscopy (IFS) is a method to collect both spatial and spectral data over a two-dimensional field in a single exposure [Allington-Smith 2006]. It uses Integral Field Units (IFU). Each pixel in the resulting 2D image comes with spectral information encoded in it, in the form of an array of spectral curves throughout the electromagnetic spectrum. This combination between spectral and spatial information is called spectral pixel, or "spaxel". This creates an additional dimension to our data, forming datacubes.

Even though IFS can capture all the spectral information in a single exposure, it offers a more limited field of view than other techniques. This means that multiple exposures with different pointings are required to produce the same number of volume resolution elements. The individual exposures are then combined to create a complete datacube. On the other hand, IFS minimizes the effects of atmospheric disturbances and the interference of cosmic rays, resulting in higher-quality data, crucial for accurate analysis.

There are many ways to create spaxels; some of the most sophisticated IFS techniques are the microlens array, fiber arrays and image slicers [Allington-Smith e Content 1998]. The instrument used to collect the data we use in this work, the Multi Unit Spectroscopic Explorer (MUSE), uses image slicers, the details of which will be explored in the next section.

2.1.1 The MUSE instrument

MUSE is an advanced Integral Field Spectrograph (IFS) located at the Very Large Telescope (VLT) on Cerro Paranal, Chile, specifically mounted at the Nasmyth focus of the Yepun telescope unit. With a broad wavelength range covering from 4800Å to

9300Å, MUSE has applications in diverse astrophysical studies, including galaxy formation and evolution, exoplanet monitoring, and spectroscopic analysis of high-redshift galaxies. MUSE's modular design comprises 24 identical units (Figure 7). Each module consists of an advanced slicer, a spectrograph, and a 4000×4000 pixel Charge-Coupled Device (CCD) detector. The CCD detector converts incoming photons into digital signals. Light hits the detector and the electrons move to the conduction band of the semiconductor. This charge information is sequentially passed between capacitors, forming a continuous data chain, before being converted into a digital signal by an analog-to-digital converter (ADC). MUSE can also utilize Adaptive Optics (AO) via the VLT's secondary deformable mirror, as detailed by Bacon et al., to enhance spatial resolution. This configuration allows MUSE to cover a 1 square arcminute field of view in Wide Field Mode (WFM), or 7.5 square arcseconds in Narrow Field Mode (NFM) [Bacon et al. 2010].

The optical system first divides the incoming light into the 24 Integral Field Units (IFUs), which are then directed through a slicer. The slicer further decomposes the light, separating each IFU into 48 individual slices. Each of these slices is directed to a distinct region on the CCD's surface. Within each region, approximately 76.5 pixel rows capture the spatial distribution of the light. Simultaneously, each column records the spectral dispersion for that slice, arranging data from bluer wavelengths at the bottom to redder wavelengths at the top.

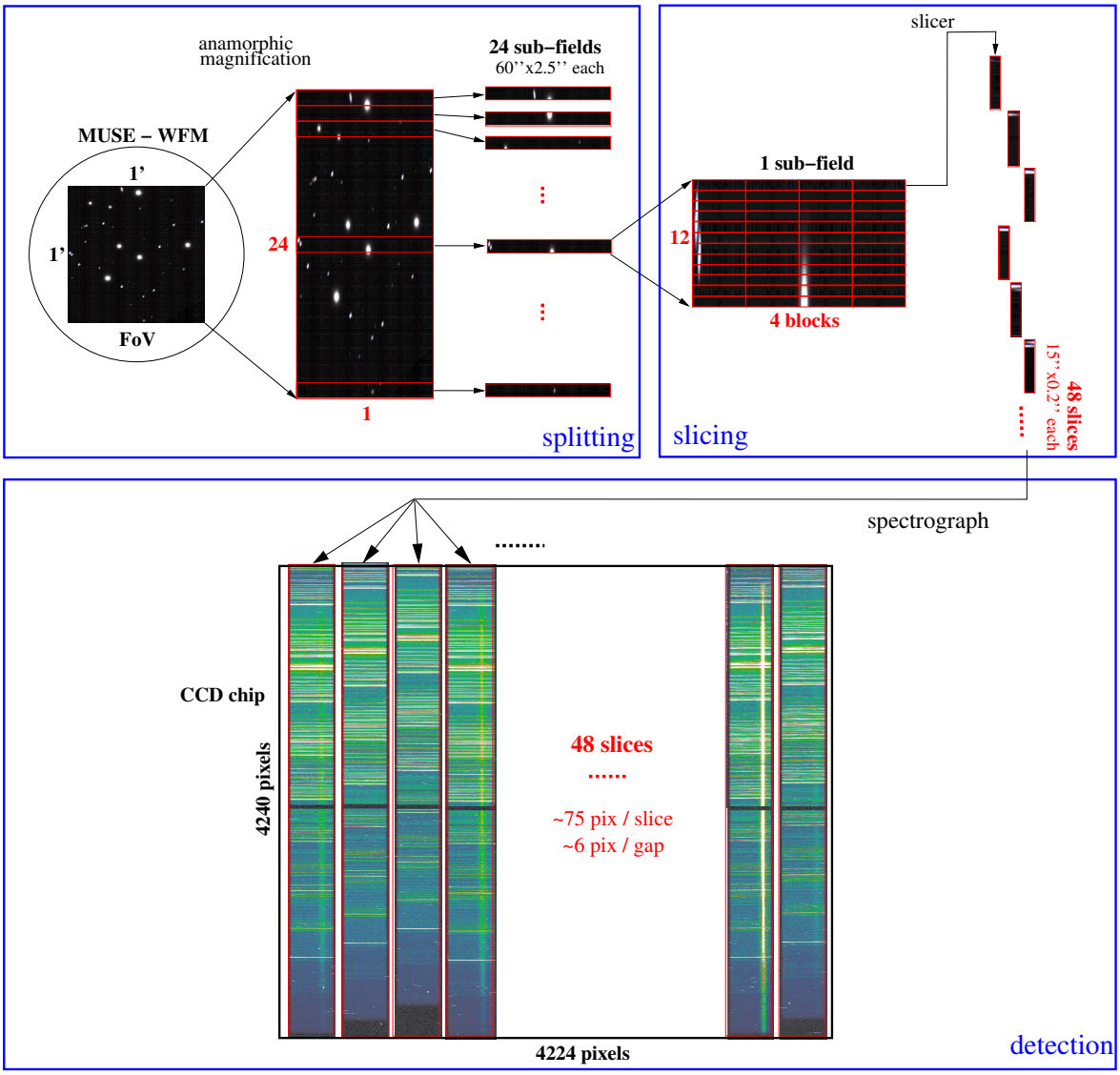

Figure 7 – A schematic view of the lightpath in the MUSE instrument, from [Weilbacher et al. 2012].

2.2 SCIENCE IMAGE REDUCTION

The raw images created by the VLT had to be reduced before we could use them, since there are instrumental characteristics that must be removed for an accurate analysis. The reduction process was already done when we downloaded the data, and was done using the ESO Data Reduction Pipelines and Workflow Systems, which are a series of reduction scripts. Some tasks required for this reduction are listed below.

Bias subtraction

The CCD counts the photons that reach it by detecting the current of excited electrons it produces. It uses an ADC in order to convert the signals and store the information into bits. These bits give us a finite number of levels to express the intensity

of light that each pixel receives. For example, if the information is stored into 8 bits, we have 256 levels, so the information can be separated into 256 levels of intensity. For 16 bits, this number goes up to 65536 level, allowing a more detailed and accurate separation. The ADC operates within a certain range. If the baseline is zero, very weak or negative signals may go undetected, and information will be lost. The bias artificially increases this baseline so that these signals are within the ADC's detection range. Each detector has a bias, and we measure it by taking a zero-second exposure with the camera shutter closed, and is later subtracted.

Flat-field correction

The telescope lens is prone to getting dust and other particles on its surface, which appear in the output image. The flat-field frame is an image of a uniformly illuminated frame, usually a white screen illuminated by a lamp, where we can detect and track patterns due to any imperfections in the lens, as well as any differences in illumination due to variations in the optical system. We divide the science image by the normalized flat-field frame in order to correct these instrumental interferences.

Cosmic ray and bad pixels removal

The flat-field frame is also useful to remove bad pixels from our science image, that is, spots on the CCD camera that might be damaged, or any other kind of interference that could induce errors. Damaged spots in the CCD can lead to undercounting photons, or not counting them at all, while cosmic rays are high-energy particles that cause much higher counts when they reach the CCD than photons.

2.3 PROCESSING THE DATA CUBE

2.3.1 Cutting, shifting and combining the cube

We had initially intended to analyze 10 data cubes obtained from the observations on February 7th and 8th, 2022. However, due to the presence of high instrumental noise in the data obtained on the second night, we were forced to discard the eight datacubes produced. The level of noise severely compromised the data quality, preventing a reliable application of our stellar population synthesis models and emission line analysis. Each of the eight data cubes present straight lines across the image, along both spatial axes, which was likely due to an error during the sky counts subtraction. When I combined the cubes, rather than averaging out and canceling itself, the pattern intensified. This effect was especially problematic along the central axis, where the strongest lines intersected directly over one of the interacting system's three nuclei. As a result, the spectral information in that region was heavily distorted (Figure 8), effectively eliminating our ability to extract any meaningful data about the third AGN.

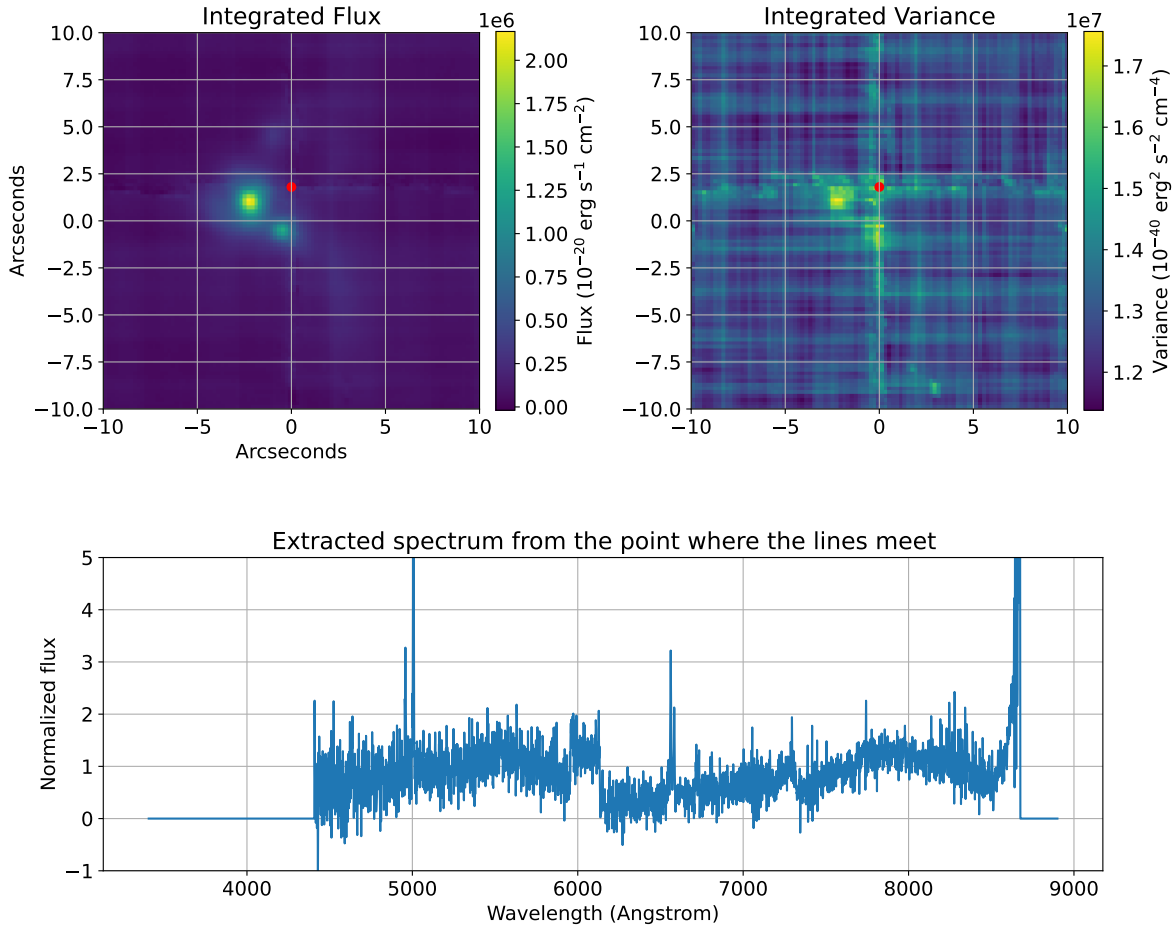

Figure 8 – Combination of the eight datacubes showing the line pattern across the image. The extracted spectrum is from the point where the lines meet, and shows the distortion caused by the instrumental errors.

The remaining datacubes consisted of 2 exposures of ≈ 900 s each. Each exposure gave us a data cube covering a grid of 316×317 pixels, or 60×60 arcsecs. For a more efficient analysis, I combined the two cubes into one. The first step was to locate the system in the cube and isolate it, and I did this by constructing a histogram of the flux emitted (Figure 9). Knowing that the sky emission formed a bell-curve distribution, I set a threshold of two times the standard deviation, corresponding to $\sim 95\%$ of area below the curve. Data below this threshold was dismissed as sky, leaving me with the signal that was mainly emitted by the system (Figure 9). I then secured an area of 100×100 pixels, or 20×20 arcsecs with the system at the center of it. After both cubes were cut, I had to combine them, but upon inspection, I saw that the system was not in the same spot inside both cubes (Figure 10). To overcome this problem, I chose a reference cube and, based on the position of emission lines in it, shifted the pixels in the other cube to match, and combined them (Figure 11). I then extracted the spectra from it and corrected it by removing reddening due to extinction (caused by the dust present in our Galaxy), using

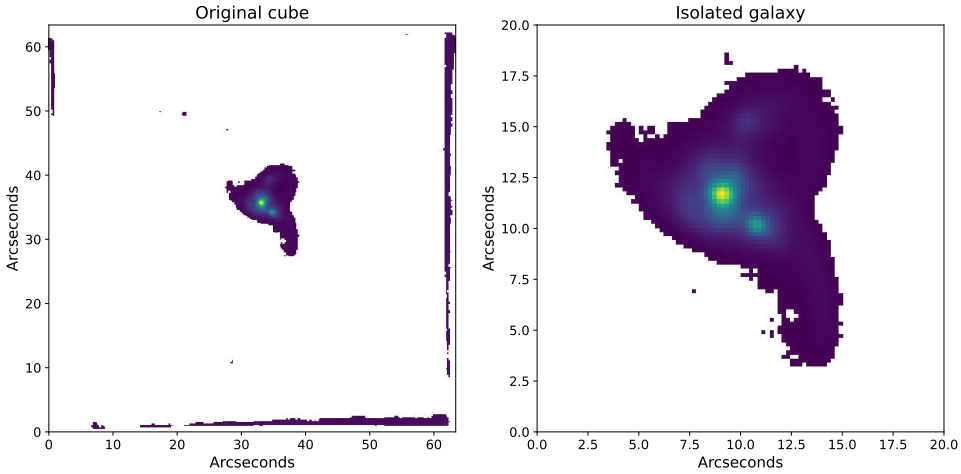

Figure 9 – Comparison between the original 60 × 60 arcsecs cube and the slice of 20 × 20 arcsecs done to isolate the system.

the model G23 [Gordon et al. 2023] from the package Interstellar Dust Extinction, available on Github.

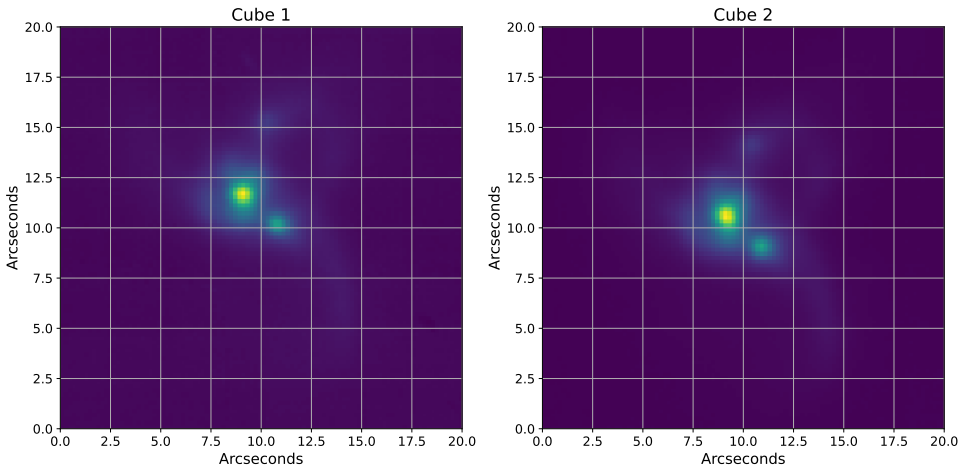

Figure 10 – Comparison between the two cut cubes highlighting the difference in the position of the system within each grid in relation to the central reference pixel.

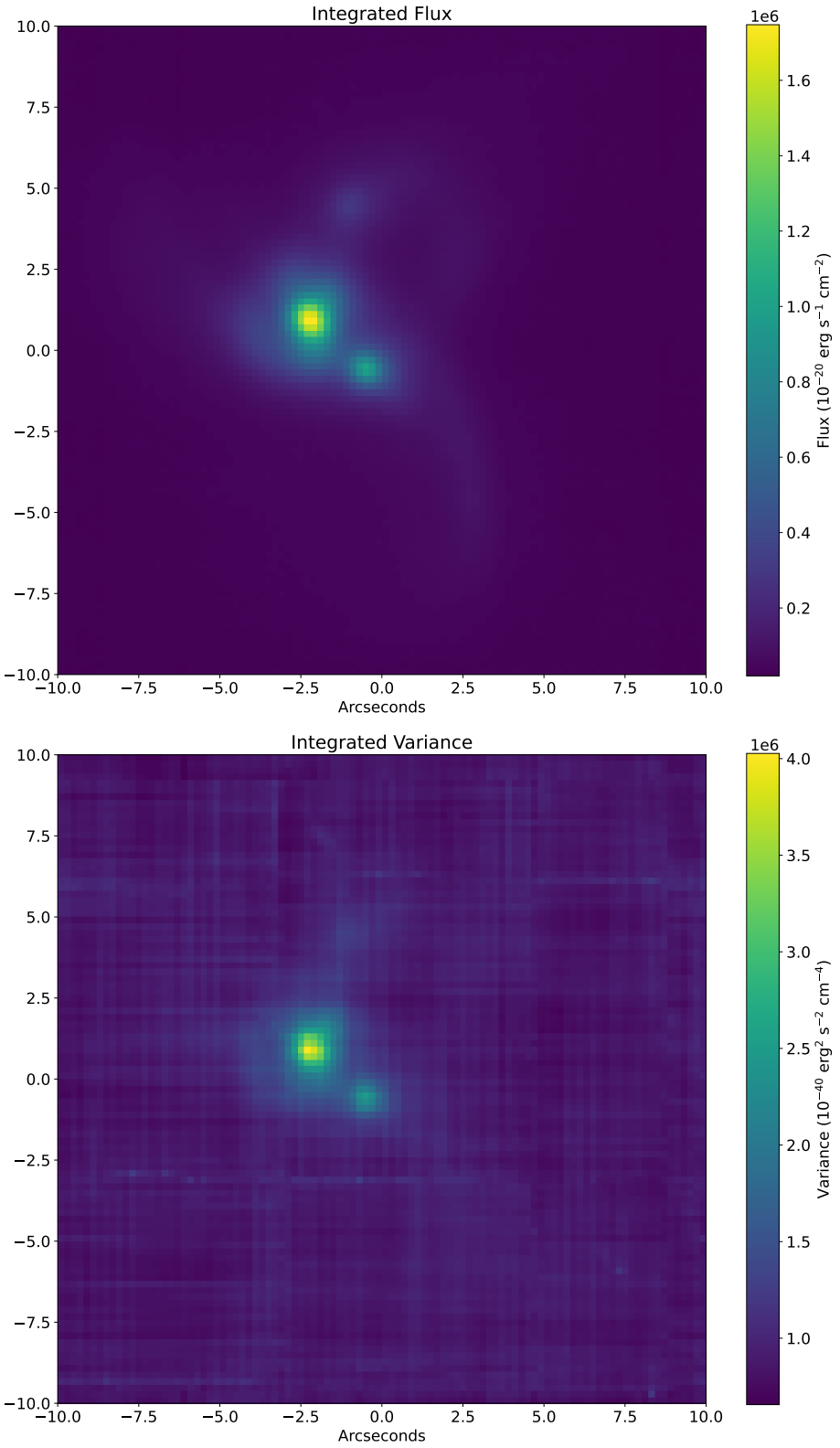

Figure 11 – SDSSJ0849 combined cube.

2.3.2 Dust extinction correction

Dust extinction is the reddening and dimming effect of light from a source as it travels through the interstellar medium to Earth. Along our line of sight, dust grains absorb and scatter photons, predominately affecting shorter (bluer) wavelengths. This process attenuates the measured flux of light. The extinction curves, that is, the wavelength dependence of dust extinction, can provide information about the size, composition, and shape of these interstellar dust grains.

One parameter used to quantify reddening is the color excess, defined as

$$E(B-V) = A_B - A_V = (B-V)_{obs} - (B-V)_{int}$$

where V and B are the magnitudes in the Johnson-Morgan photometric bands and $A_B = B_{obs} - B_{int}$ and $A_V = V_{obs} - V_{int}$ are the interstellar extinction in the B and V bands, respectively. While the color excess is proportional to the dust column density and was used as a calibration parameter, it makes more sense to use A_λ/A_V as our extinction law, since extinction is expressed directly [Cardelli, Clayton e Mathis 1989]. The extinction parameter can be defined as

$$R_V = A_V/(A_B - A_V),$$

which is used to trace the extinction curves for the model G23, and is the ratio of total to selective extinction. While the value of R_V can change with the line-of-sight, we used the standard value for a diffuse interstellar medium $R_V = 3.1$, and $A_V = 0.142$ mag as the extinction in the U band [Schlafly e Finkbeiner 2011].

We chose the dust extinction model G23 because it covers the far-ultraviolet (912 Å) to mid-infrared (32 μm). It is based on the spectroscopic extinction curves used for the GCC09 [Gordon, Cartledge e Clayton 2009], F19 [Fitzpatrick et al. 2019], G21_MWAvg [Gordon et al. 2021], and D22 [Decleir et al. 2022] studies. The comparison between G23 and other models is shown in Figure 12, where it can be seen that the G23 model covers a much wider range. The extinction corrected spectrum from the main nucleus is shown in Figure 13.

2.4 STELLAR POPULATION ANALYSIS

Understanding the evolution of a galaxy requires understanding the evolution of the stellar systems in it. The different stellar populations found in a galaxy provide information about its history. Stellar Population Synthesis (SPS) is a great tool that allows us to decode the stellar energy distributions (SED) of a galaxy. SEDs contain information about the galaxy's physical properties, dynamical behavior, and evolutionary history, within the spectra across different wavelengths. We aim to model the observed SEDs as a composite system based on the knowledge that the light we measure comes from a mixture of different

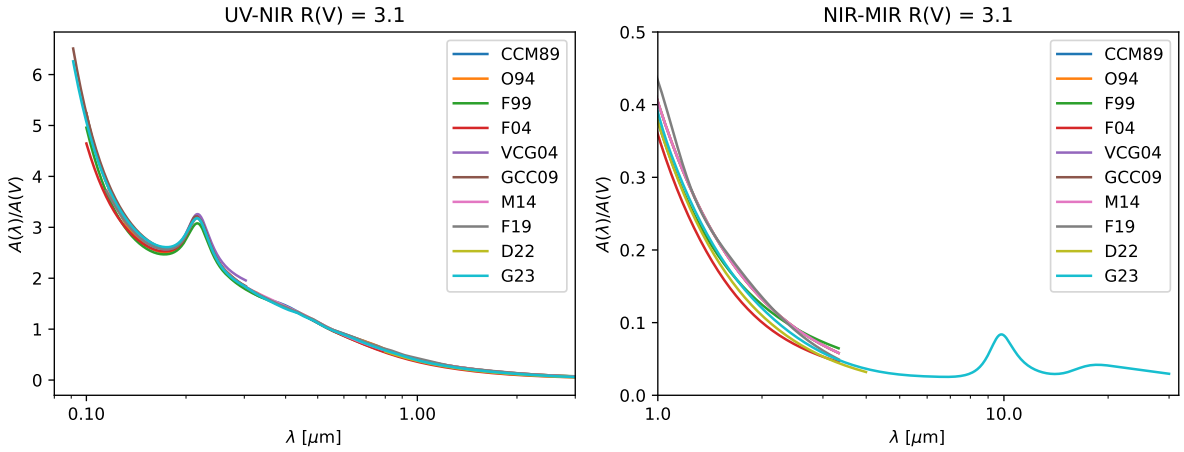

Figure 12 – Examples of multiple Parameter Average models showing the wider range of model G23, taken from [Gordon et al. 2023].

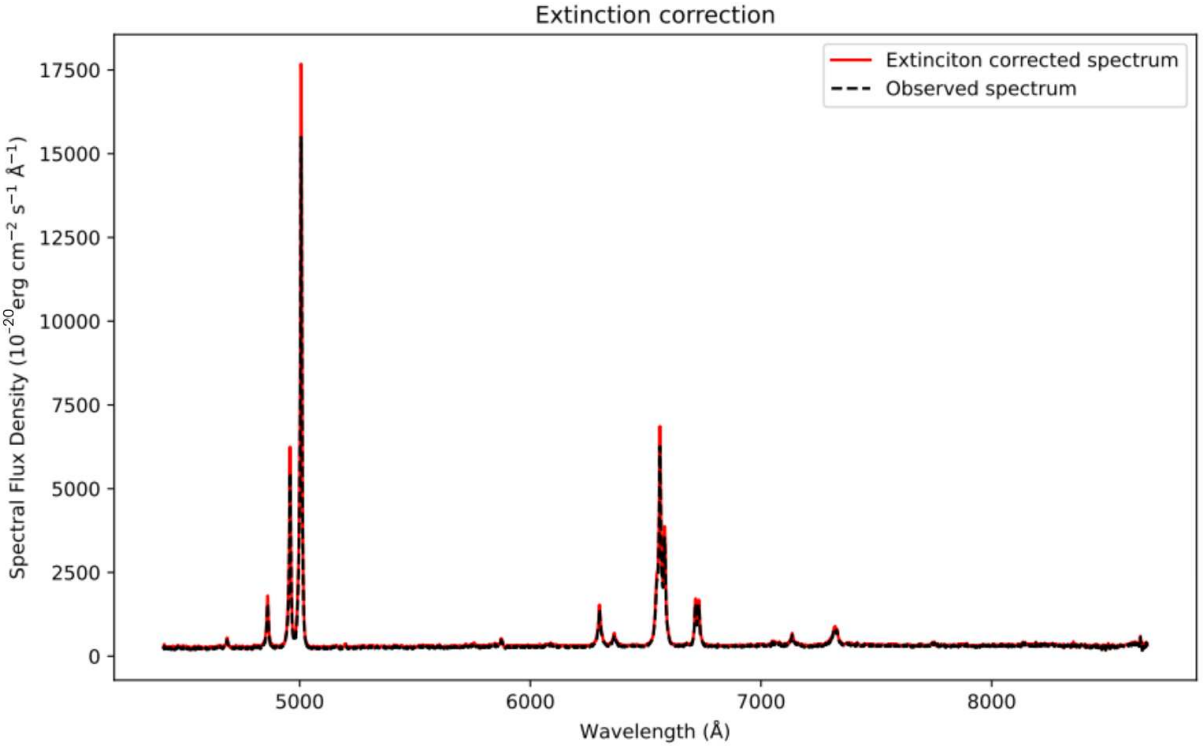

Figure 13 – Extinction corrected spectrum from the main nucleus of SDSS J0849.

stellar populations, each one with its own properties. Once we determine these components, we can trace the galaxy's evolutionary history.

Cid Fernandes et al. pioneered the so-called evolutionary population synthesis methods, which compare galaxy data with models that follow the time evolution of an entire stellar system by combining libraries of evolutionary tracks and stellar spectra with prescriptions for the initial mass function (IMF), star formation and chemical histories. This study led them to create the software STARLIGHT, which is better explained in section

2.4.1 [Fernandes et al.].

Simple Stellar Populations (SSPs) are groups of stars that were born from the same gas cloud, thus they have the same age and chemical composition. SSPs can be formed by both giant and dwarf stars. Therefore, when modelling them, we need an initial mass function, a spectral library, and evolutionary tracks. The initial mass function (IMF) tells us how the mass might be distributed between the stars within the SSP at their birth. It is famously associated with Salpeter's seminal work in 1955, $dN/dm \propto m^{\alpha}$, with $\alpha = -2.35$. This result is derived from the luminosity function and suggests that the SSP contains a greater number of low-mass stars than high-mass stars. As the name implies, the evolutionary tracks represent the known process that stars go through as they evolve from birth to death, with a significant dependence on their masses and chemical composition. It traces the star's development from the early stages, beginning at the pre-main sequence phase, through the hydrogen burning in the main sequence until its final stages of evolution in the post-asymptotic branches. Spectral data can be theoretical, empirical, or a combination of both when creating a Spectral Library, which is a database of SEDs of various star types. Realistically, galaxies have multiple SSPs in different stages of evolution, different masses and metallicities. That leads us to consider a galaxy as a composition of said SSPs, i.e, it forms a Composite Stellar Population (CSP). We aim to identify the SSPs present in SDSSJ0849 to better understand its evolution.

2.4.1 Spectral fitting with STARLIGHT

STARLIGHT is a software that fits an observed spectrum O_λ with a model M_λ built from a linear combination of $N_\star$ spectral components from a pre-defined set of base spectra, the modeled SSPs. Some components are the population vector $\vec{x}$ containing the percentage of simple star population (SSP) used in the fit, the global extinction A_V and the kinematic components velocity shift $v_\star$, and velocity dispersion $\sigma_\star$.

We can decompose the model M_λ onto the $N_\star$ components as follows:

$$M_\lambda = \sum_{j=1}^{N_\star} L_{\lambda,j} = \sum_{j=1}^{N_\star} L^0_{\lambda,j} \otimes G(v_\star, \sigma_\star) 10^{-0.4 A_{\lambda,j}} \tag{2.1}$$

$$M_\lambda = M_{\lambda_0} \left(\sum_{j=1}^{N_\star} x_j b_{j,\lambda} r_\lambda \right) \otimes G(v_\star, \sigma_\star), \tag{2.2}$$

where $b_{j,\lambda}$ is the spectrum of the j^{th} SSP normalized at λ_0, $r_\lambda \equiv 10^{-0.4(A_\lambda - A_{\lambda_0})}$ is the reddening term, M_{λ_0} is the synthetic flux at the normalization wavelength, and G is the Gaussian filter centered at velocity $v_\star$ and with dispersion $\sigma_\star$. Each component x_j ($j = 1 \ldots N_\star$) represents the contribution of the SSP with age t_j and metallicity Z_j to the model flux at λ_0. STARLIGHT searches for the best fitting model that minimizes $\chi^2 = \sum_\lambda [(O_\lambda - M_\lambda)\omega_\lambda]^2$, where ω_λ^{-1} is the error in O_λ.

Transition	Wavelength (Å)	Masked wavelength range (Å)
HeII	4685.7	4670.0 – 4695.0
Hβ	4861.3	4840.0 – 4890.0
[OIII]	4958.9	4930.0 – 4980.0
[OIII]	5006.8	4980.0 – 5040.0
[NI]	5199.1	5080.0 – 5125.0
[NI]	5199.1	5193.0 – 5202.0
[FeIII]	5270.4	5260.0 – 5274.0
HeI	5875.6	5850.0 – 5900.0
[OI]	6300.3	6265.0 – 6335.0
SiII	6347.1	6340.0 – 6355.0
[NII]	6548.0	6530.0 – 6547.0
Hα	6562.8	6500.0 – 6645.0
[NII]	6583.5	6575.0 – 6600.0
[SII]	6716.4	6705.0 – 6750.0
[SII]	6730.8	6735.0 – 6743.0
HeI	7065.2	7040.0 – 7090.0
[ArIII]	7135.8	7120.0 – 7150.0
[OII]	7319.5	7275.0 – 7320.0
[OII]	7330.2	7320.0 – 7360.0

Table 1 – Masked emission lines.

In order to use STARLIGHT, we need an input spectrum, a mask file, a spectral base, a configuration file, and a grid file. For each pixel in our 100×100 image, we extracted the spectral information to insert into the grid file. I generated 100 grid files, one for each pixel along the x-axis, which contained the 100 corresponding spectra along the y-axis. I used the evolutionary synthesis models BC03, which uses the STELIB spectral library, with 3 metallicities, $Z = 0.004$, $Z = 0.02$, and $Z = 0.02$, and 15 different ages, ranging from 1 Myr to 1.13 Gyr [Bruzual e Charlot 2003]. The IMF I used was from Chabrier [Chabrier 2003]. I masked the emission lines in the galaxy's spectrum by delimitating a region of around 50 to 100 Å to each side of the main emission lines present in it, depending on the emission line's width. The masked emission lines can be seen on Table 2.4.1. In the configuration file, I gave STARLIGHT the instructions for the fitting, such as the path of the files mentioned above and the clipping method chosen. In our case, we chose the NOCLIP option. I used the 5200 to 5250 Å normalization window, and 5225 Å normalization wavelength.

2.4.2 Featureless continuum

When investigating the spectra of Seyfert type-2 galaxies and narrow-line radio galaxies, Koski 1978 found that all galaxies had an UV excess in their spectra in comparison to non-active galaxies. Additionally, all of them also had an underlying continuous spectrum that seemed to dilute the stellar light continuum. Subtracting the stellar contribution to the spectrum left a smooth featureless continuum under the emission line spectrum that

could be modeled by a power-law of the form $F_\nu \propto \nu^{-\alpha}$. Such power-law is the source of photoionization and recombination of hydrogen and helium atoms and ions, producing the Hβ, HeI λ5876, and HeII λ4686 emission lines. He found that this featureless continuum is also responsible for about 30% of the light fraction of Hβ λ4861. While the UV excess cannot yet be fully explained, it is widely assumed that the power-law continuum arises from the X-rays produced by the Compton scattering of photons produced in the accretion disk by the hot electron corona surrounding it [Haardt, Maraschi e Ghisellini 1994]. The power law index α can have values ranging from $0.5 < \alpha < 2.0$; however, when dealing with a large volume of galaxies, the general value $\alpha = -1.5$ can be adopted [Kauffmann et al. 2003, Fernandes et al. 2004]. To add the power law due to the AGN ionization to our base files, we selected a radius of 3 spaxels around each nucleus, and ran Starlight adding 5 power laws: $\alpha = 0.5$, $\alpha = 1.0$, $\alpha = 1.5$, $\alpha = 2.0$, and $\alpha = 2.5$. The results showed that two nuclei had the same power law, while one had a different combination of power laws. For the main and north nuclei, the power law exponent was $\alpha = 0.5$, and for the south nucleus it was a combination of $\approx 19\%$ of $\alpha = 1.5$ and $\approx 6\%$ of $\alpha = 2.0$. We then created the spectra of these power laws with a simple linear combination of them, and added to the base files. To determine which sections of the galaxy we would apply each power law, we drew a limit of two-times the Point Spread Function (PSF) radius center around each nucleus. The PSF value was taken from the datacube header. We ran STARLIGHT again and combined the stellar population synthesis with and without the power law.

2.5 EMISSION LINE ANALYSIS WITH IFSCUBE

The analysis of ionized interstellar gas was based on the emission line profiles fitting, using the package of functions for integral field spectroscopy data IFSCUBE[1]. This software allows the simultaneous fitting of several spectral features, with or without constraints and limits for the parameters. The plot of the spectra of each nuclei of SDSSJ0849 can be seen in Figure 14. In this work, we used it to derive a model for the gas emission lines seen in the SEDs to characterize the dynamics of the ionized gas present in the galaxy. We assumed the gas dynamics is the same for the entire cloud, which led us to apply constraints on the kinematic parameters such as radial velocity, velocity dispersion, and flux ratios. We selected 10 emission lines to fit using Gaussian functions: Hβ λ4861 , [O III] λ4985, [O III] λ5007, [O I] λ6300, [N II] λ6364,[O I] λ6548, Hα λ6563, [N II] λ6583, [S II] λ6717, and [S II] λ6730. I then subtracted the stellar continuum and fitted a pseudo continuum using a 10th-order polynomial.

IFSCube has two methods of minimization available, Differential Evolution and Sequential Least Squares Programming (SLSQP). The differential evolution method is a stochastic population-based evolutionary algorithm for the optimization of continuous

[1] https://github.com/danielrd6/ifscube

variables [Storn e Price 1995]. Given a parameters grid, this method runs through it and does not require the optimization problem to be differentiable. This means the chance of getting stuck in a local minimum is reduced. SLSQP is a method to solve the general nonlinear programming problem for a local minimum where the functions are assumed to be continuously differentiable [Kraft 1988]. While the differential equation method results in a better quality fit, it requires more computational power than SLSQP. IFSCube can fit either a single spectrum or an entire cube. I first fit one single spectrum, the main nucleus, using two gaussian components, one narrow and one broad, giving an initial input for σ and the velocity. The initial fitting estimated the velocity of the broad component as around 300 to 500 km s^{-1}, which classify this galaxy as a type-2 Seyfert. At first, I forced IFSCube to fit the spectra based on an initial guess, which was adjusted until the fit was good. After the best initial guess was determined, I let the program adjust the fit freely based on it. During this process I used the differential evolution minimization method, which made sure my minimization parameters corresponded to global minimus. I then ran IFSCube for the whole cube, this time using the SLQP minimization method. Once more, IFSCube was free to fit the cube based on the initial parameters. The spectra of the three nuclei of SDSSJ0849 is shown in Figure 14.

2.5.1 Equivalent Width

The equivalent width (EW) of a spectral line is a quantitative measurement of an emission or absorption line area on an intensity versus wavelength plot, compared to the continuum level. It is used to describe the strength of the spectral line relative to the adjacent continuum. It is defined as the width of a rectangle placed at the level of the continuum that has the same area as the spectral line, despite its shape. Mathematically, it can be defined in terms of the the integral of the fraction of the spectral line intensity over the continuum intensity [Vollmann e Eversberg]:

$$W_\lambda = \int \left(1 - \frac{F_S}{F_C}\right) d\lambda. \tag{2.3}$$

Since the EW normalizes the line strength relative to the continuum, and is able to capture the intrinsic strength of a spectral line regardless of its apparent brightness, it becomes a reliable tool for comparing spectral features from different sources. For example, an emission line observed in two different regions of a galaxy might appear more intense if the region has a stronger continuum. However, its EW might actually be the same or even smaller than that of the same emission line in region with a weaker continuum. EW can be used to determine stellar parameters, such as the effective temperature and metallicity of a star [Sousa et al. 2007] and references within, star formation rates in galaxies [Kauffmann et al. 2003, Khostovan et al. 2024] and photoionization mechanisms, like the WHAN diagram [Fernandes et al. 2011].

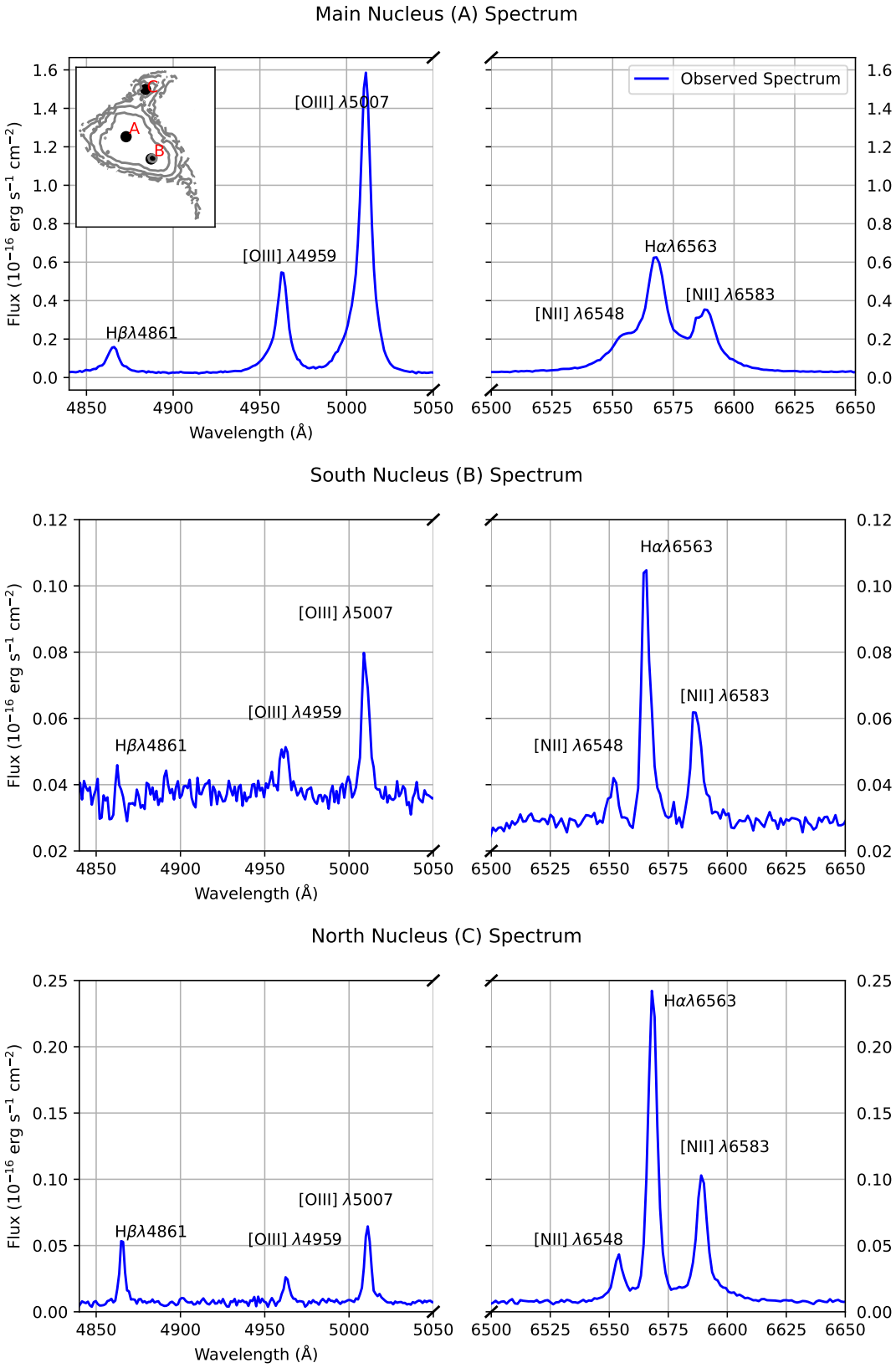

Figure 14 – Spectra of the three nuclei of SDSSJ0849. The top panel shows the spectrum of the main nucleus (A), and a figure of the system with the spatial position of each nuclei marked with black dots. The middle panel shows the spectrum of the south nucleus (B) and the bottom panel shows the spectrum of the north nucleus (C).

3 RESULTS AND DISCUSSION

3.1 TWO COMPONENT FITTING

When dealing with complex systems, the best approach is to use a set of Gaussian functions to fit the emission lines. However, it is not always obvious how many functions are enough to fit the data. When analyzing the spectral features, adding more functions can improve the fit, but can lead to overfitting statistical fluctuations that do not have any real physical meaning. Therefore, it is crucial to carefully assess whether the additional components represent real physical phenomena or if they are simply artifacts of noise. For each emission line fitted, there were three parameters: the amplitude of the Gaussian curve, the velocity, and the velocity dispersion. At first, I used a single Gaussian function for the fit. Upon examining the residual values given by IFSCube we found that, while the fit was satisfactory in some regions of the interacting system, other regions presented significant differences between the model and the observational data. This prompted us to incorporate a second Gaussian function. This way, our new fit was set to have two Gaussian components, one broader and one narrower. Each component represents a distinct kinematic group, with the velocity and velocity dispersion being the same across all emission lines within each group. After the introduction of the second Gaussian function, I plotted a velocity map for the second component and compared it with the velocity map of the first component, and we can see clear differences between the two (Figure 15).

In some regions of the system, gas in one of the components is moving in the opposite direction of the gas in the other component. These differences indicate the complexity of the gas kinematics within the system, suggesting multiple gas components with varying dynamics. I denominated each component as narrow or broad based on the width of their Gaussian function. Here, "broad and narrow components" do not mean the same as in the context of Seyfert Galaxies classification. The term "broad component" refers to the wider Gaussian function between the two components. All three nuclei present the emission line profile of Seyfert Type 2 galaxies, with FWHM < 2000 km s^{-1}, and we can only observe the narrow line regions of the system. We followed the analysis as such, thus allowing for a more accurate representation of the underlying gas motions and a better understanding of the interacting system's kinematic structure.

To determine where the multiple Gaussian functions were needed to properly fit our data, I created a mask based on a statistical analysis of the reduced χ^2, which is the parameter that indicates how good, or bad, is our fitting. I first calculated χ^2 (Eq. 3.1) by dividing the square of the difference between the observed data and the fitted model by the variance, and summed over all points in our data. Then, to get the reduced χ^2, I divided χ^2 by the number of degrees of freedom, $\nu = N_S - N_P$, where N_S is the number of samples and N_P is the number of parameters, both contained in the wavelength window 4977Å–5037Å, which encompasses the [O III] λ4959 and [O III] λ5007 lines (Eq. 3.2) . I

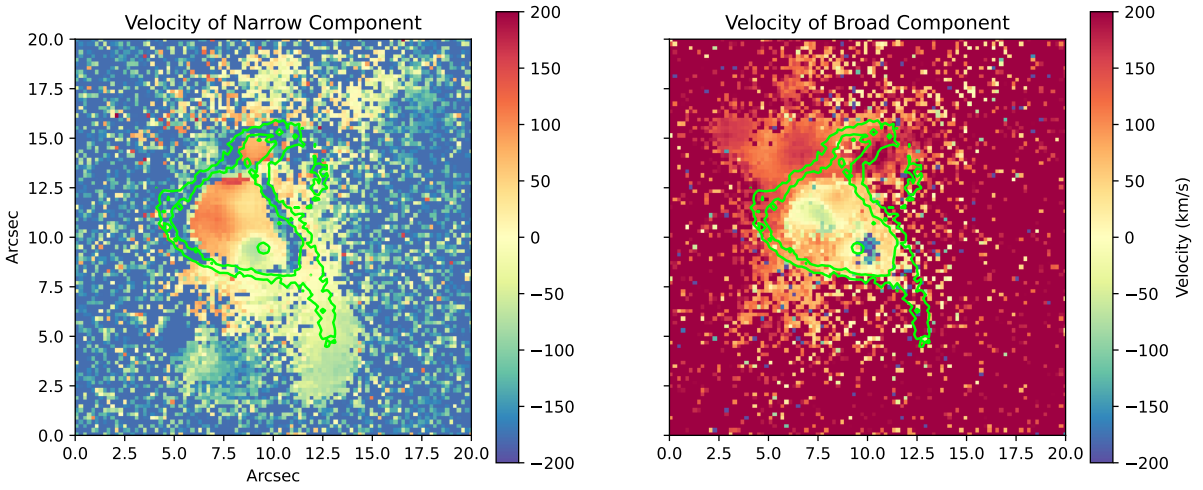

Figure 15 – The velocity maps of the two Gaussian components fitted show significant differences in the gas kinematics. The terms "Narrow" and "Broad" refer to the width of the Gaussian function used for the fit. The green contour delimits the region where there is enough signal from the stars to conduct our analyses.

calculated the reduced χ^2 for the single-Gaussian component fit (which I will call one component fit) and set a threshold of 1.5 for its value, which delimited two regions on the interacting system where I needed to use the results of the two component fit.

$$\chi^2 = \sum_i \frac{(O_i - M_i)^2}{\sigma} \tag{3.1}$$

$$\chi^2_\nu = \frac{\chi^2}{(N_S - N_P)} \tag{3.2}$$

I constructed the main component of our fit as follows: outside the regions delimited by the reduced χ^2 threshold, I used the results from the one component fit; Inside these regions, I had to determine which was the main component between the two. I compared the amplitudes of the [O III] emission line of both kinematic groups: the kinematic group that had the higher amplitude belonged to the main component. Figures 16, 17, and 19 show the comparison between the flux, velocity and velocity dispersion of the main and secondary components. From the velocity map (figure 16) we see differences in the direction in which the gas is moving between the two. In the main component map gas seems to be moving towards us in the small cloud at the bottom in the main component map. In the central region next to the main nucleus, we see that gas is moving with higher velocities (≈ 100 km s^{-1}), also moving away from us. The gas in the secondary component, on the other hand, seems to be moving away from us in the small cloud at the bottom, and in the central region next to the main nucleus, with velocities of ≈ -50 km s^{-1}. The velocity dispersion maps for both components are very similar, although the dispersion is higher for the secondary component (figure 17). The two component fit for each nucleus

can be seen in figure 18. It shows the detailed plot of the observed data, the SP synthesis, the two Gaussian functions used to fit the data, and the resulting fitted curve.

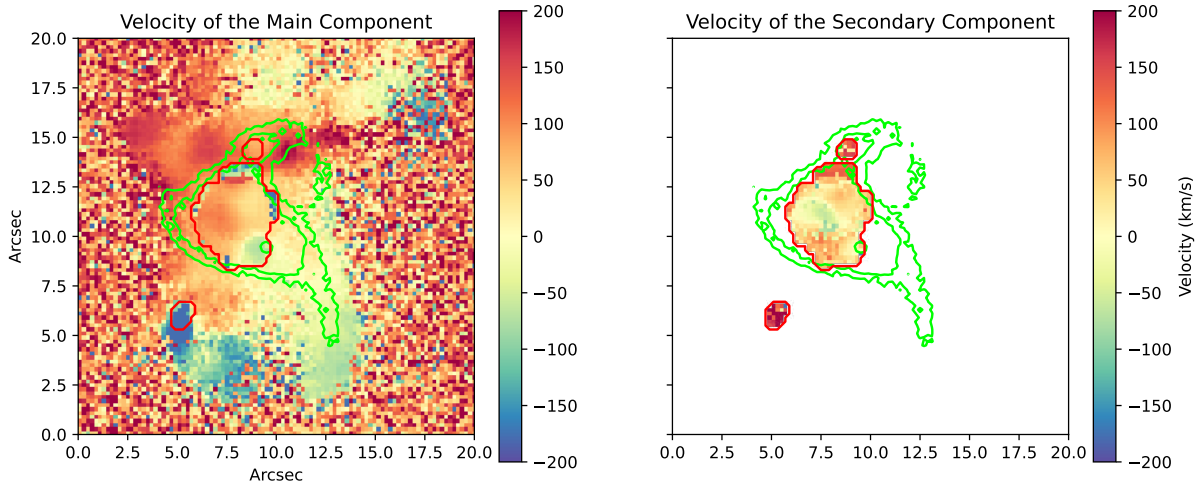

Figure 16 – Comparison between the velocity of the main component of the fit (left), and the weaker component (right).

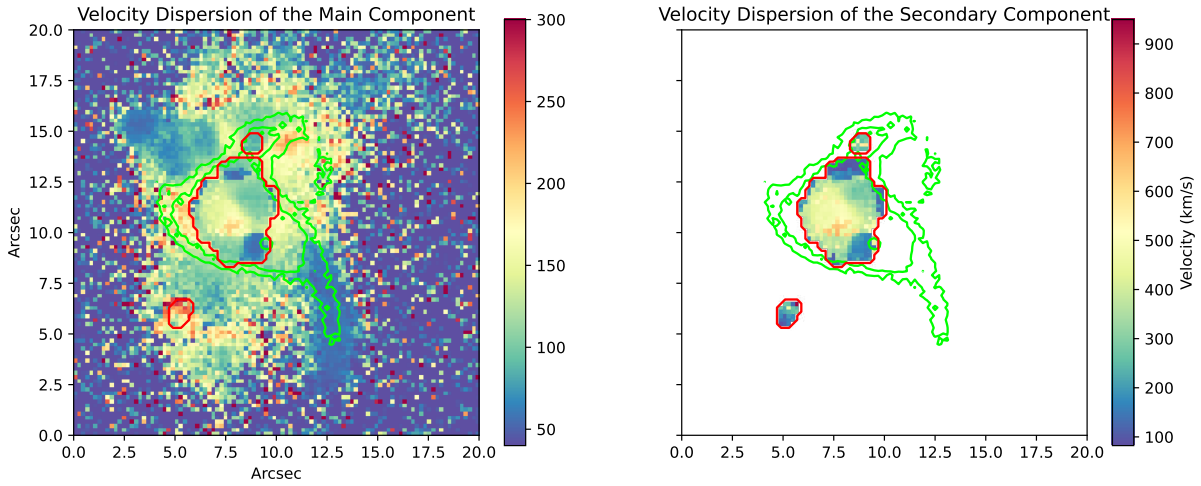

Figure 17 – Comparison between the velocity dispersion of the main component of the fit (left), and the weaker component (right).

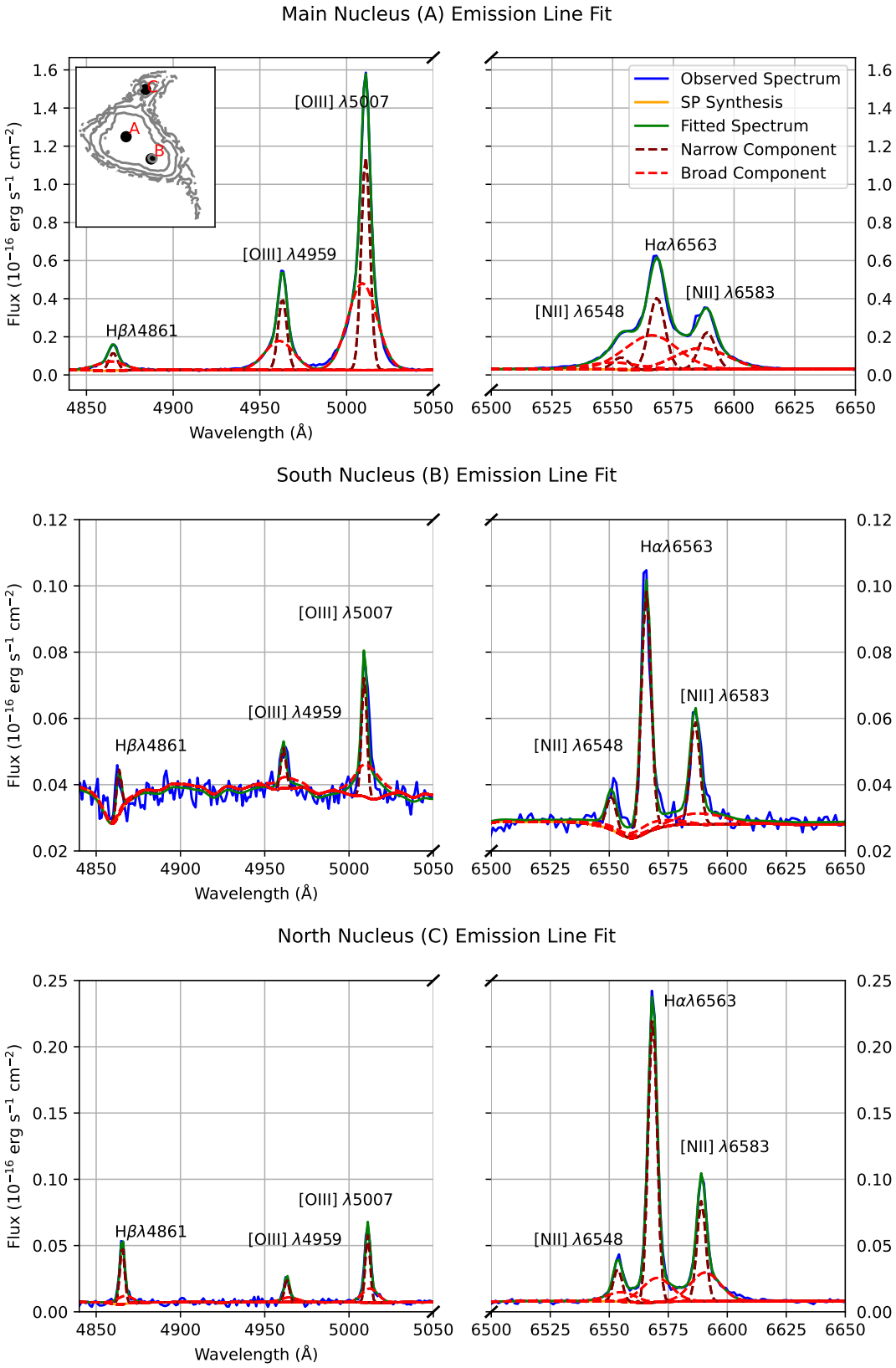

Figure 18 – Two component fit for the three nuclei. The solid lines represent the observed data (blue), the Stellar Population (SP) synthesis (orange) and the fitted curve (green). The dashed lines represent the two Gaussian components used, the narrow component (maroon) and the broad component (red).

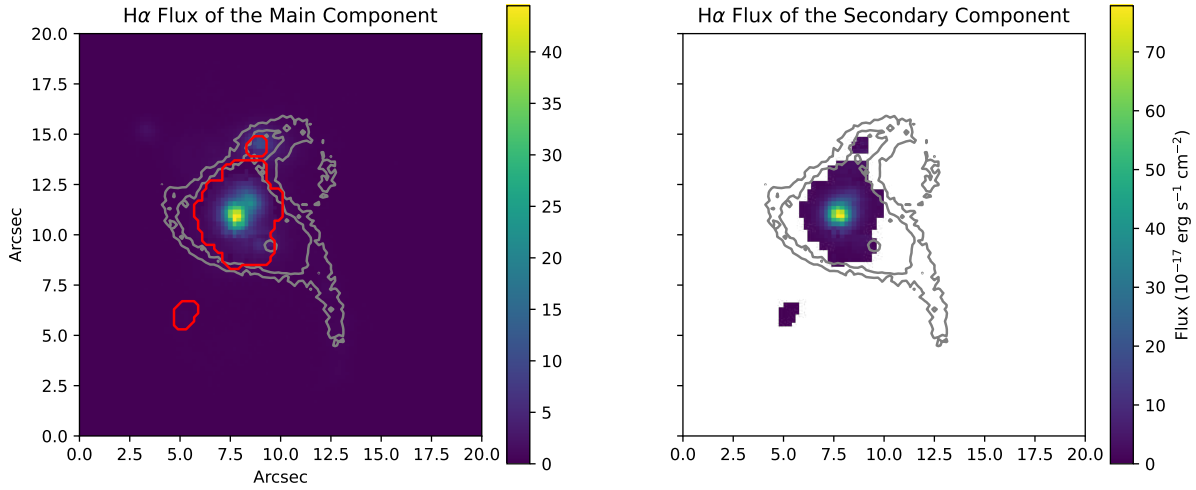

Figure 19 – Comparison between the flux values of the main component of the fit (left), and the weaker component (right).

The Hα flux plot for both components show that the flux of the secondary component is more intense than in the main component (Figure 19). This is because we constructed the secondary component using the broader component. Since the flux is proportional to the width of the Gaussian curve, the wider the broad component is, more flux it has. This also helps to explains why, when plotted without the contour of the mask that limits the one and two component regions, we can see clearly that the flux has a discontinuity at the edge of it (Figure 20). To better understand what is happening, we studied a spaxel at this very limit. Figure 21 shows the comparison between its one and two component fits. We can see that the one component fit Gaussian for the [O III] emission line has a higher flux than the narrow component of the two component fit. In the border, the flux of the broad component is not zero, and because the total flux of the two component fit is the sum of the flux of both gaussian components, the presence of the broader component decreases the flux of the narrow component, which was used to construct the main component.

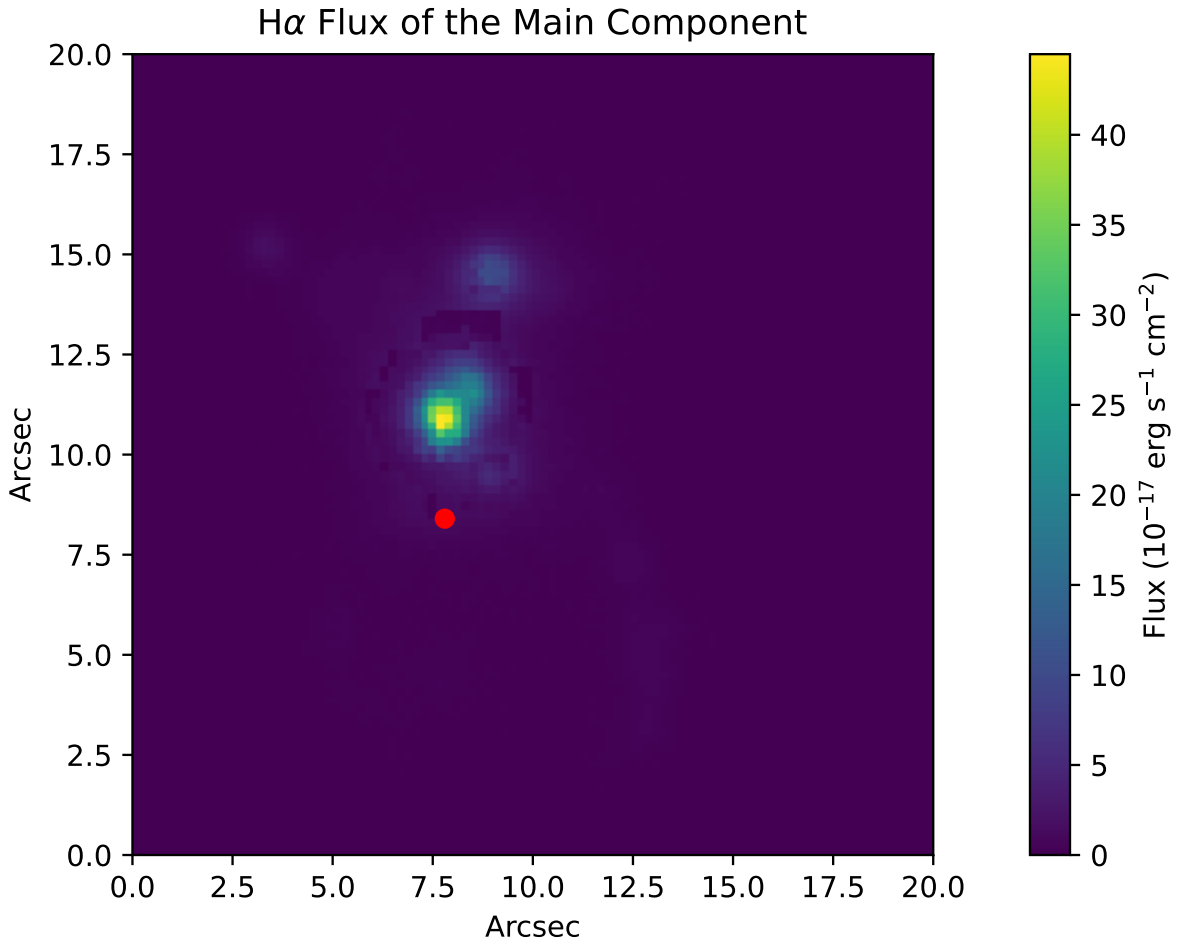

Figure 20 – Flux of Hα of the main component of the two component fit plotted without the mask. It is evident that there is a discontinuity of the flux in the limit between the two fits. The red dot represents a spaxel located at the limits of the mask.

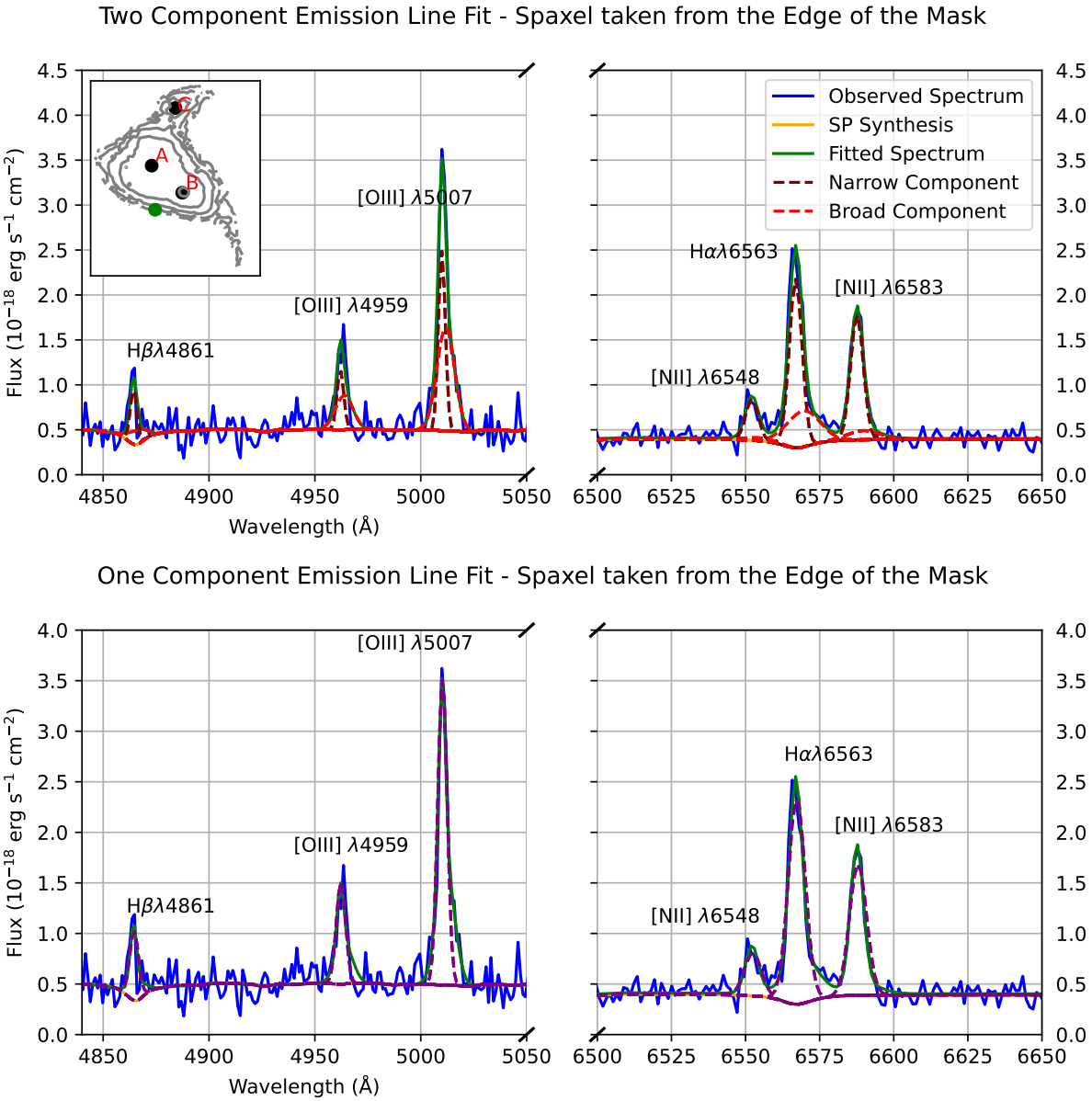

Figure 21 – Comparison between the one and two component fits for a spaxel located at the limits of the mask represented by the green diamond in the spatial plot of the interacting system (top left). The solid lines represent the observed data (blue), the SP synthesis (orange) and the fitted curve (green). The dashed lines on the two component fit plot represent the two Gaussian components used, the narrow component (maroon) and the broad component (red). The purple dashed line on the one component fit plot represent the single Gaussian component.

3.2 KINEMATIC RESULTS

To fully understand the interacting system's kinematics, we must also consider the stellar population and their respective kinematics. Figure 22 compares the gas kinematics of the main component with the stellar kinematics, offering a side-by-side view of their behavior across the interacting system. Comparing stellar kinematics with gas kinematics can only be done in regions with sufficient signal-to-noise ratio. Based on the standard deviation, I traced a contour which delimits the region where there is enough signal from the stars to conduct our analyses. Outside this contour, comparisons can't be done. This issue could be solved by applying techniques that improve the signal-to-noise ratio, such as Voronoi binning. Unfortunately, time limitation prevented us from incorporating this method into our analysis. We see some differences in the kinematics of the stars in the interacting system compared to the gas in the same regions. In the region around the main nucleus, the gas is moving away from us in higher relative velocities, as represented by the redder color in the velocity map. The stars in the same region, however, have relative velocities closer to zero or slightly negative, which means they are moving closer to us, or in a perpendicular direction to our line of sight. This is represented by the yellow-green color in the velocity map. Around the south nucleus, while the gas seems to be moving towards us, as represented by the light blue color, the stars relative velocities are much bluer in our scale. This suggests that while both gas and stars are moving towards us, the stars are doing so in higher relative velocities. The same happens around the north nucleus, where both gas and stars are moving away from us, although their relative velocities are similar. To get a clearer understanding of the stellar kinematics, we isolate the system in Figure 23, allowing for a more focused analysis.

The velocity map of the gas outside the contour show interesting structures, although we cannot be sure if these would be present in the stellar maps as well. Gas follows down the arm connected to the south nucleus, and is moving towards us, while in the region left to the main and north nucleus, the gas is very dispersed and red. In a region south of the whole interacting system, relatively farther away from the center, is a small cloud moving in an upward arch in our direction. This information allows us to get an idea of the kinematic of the system as a whole. Although the velocities along our line of sight are relatively low, varying between ± 150 km s^{-1}, the blue color around the south nucleus is present in both maps indicating that this region of the system is moving toward us. The region around the main nucleus and left to it is redder, indicating that this region is moving away from us. This suggests that the main and south nuclei may be rotating in a counter-clockwise direction at an angle of approximately $-135°$. The stellar and gas velocity maps show that in the region around the north nucleus, both stars and gas are moving away from us. There is a notable downwards arch-like structure visible extending downward from the north nucleus, seemingly connecting to the faint gas cloud at the bottom seen in the gas velocity map. This structure seems to trace the path of gas moving

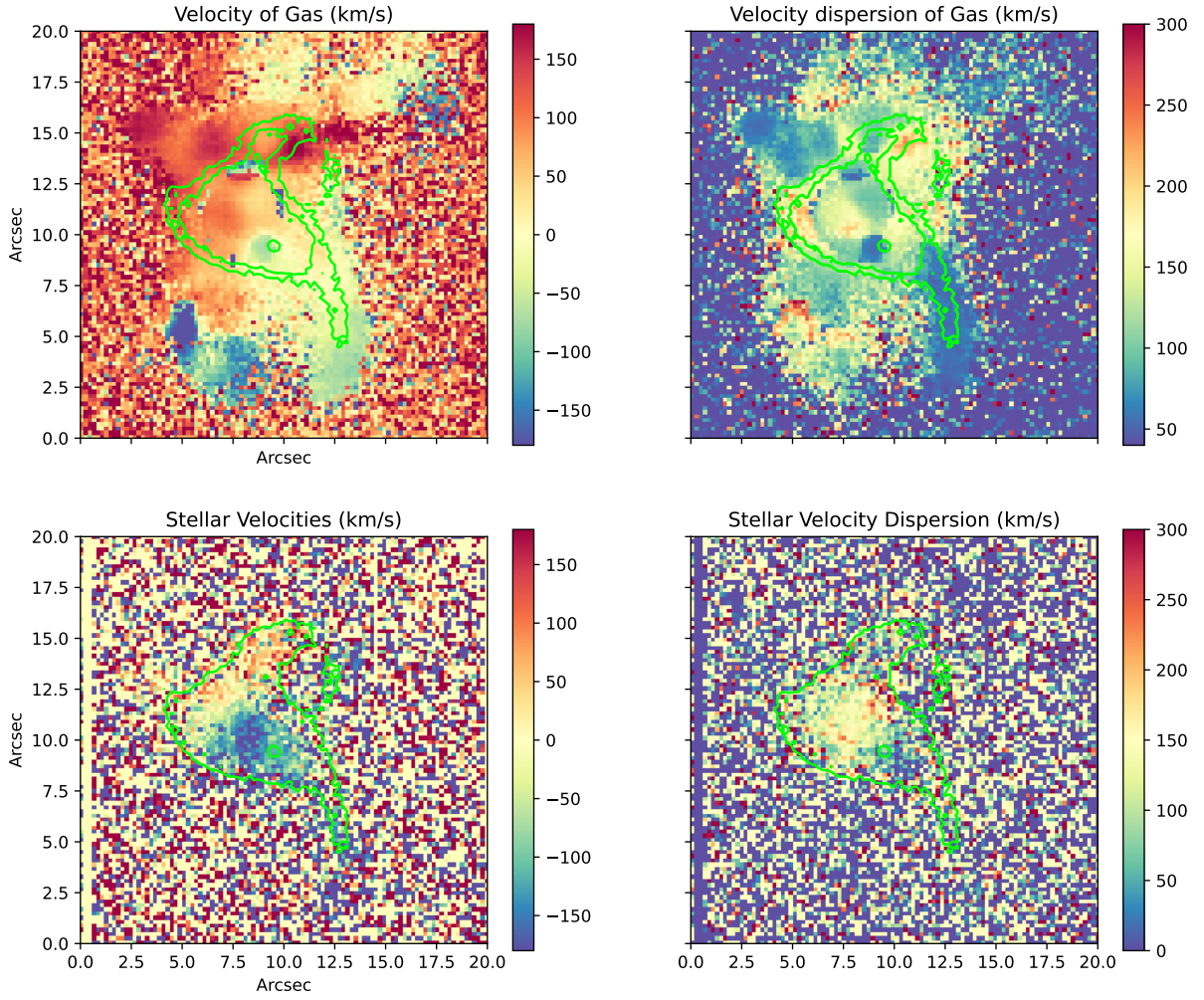

Figure 22 – Stellar and gas velocity and velocity dispersion maps of SDSSJ0849. In the central region, gas is moving away from us faster than the stars, which have lower or slightly negative velocities (toward us or sideways). Near the south nucleus, both gas and stars are moving toward us, but the stars are moving faster. Similarly, near the north nucleus, both are moving away, with similar velocities.

from the north nucleus, extending behind the interacting system's disk (therefore obscured) and rising again on the opposite side. This made us consider the hypothesis that the north nucleus is rotating in a plane that is nearly perpendicular to the rest of the interacting system, indicating a distinct kinematic behavior and a possible different evolutionary history. We hypothesize that this trajectory corresponds to the path followed by the host galaxy of the north nucleus during the merger process, leaving behind the faint gas traces we observe today. To better understand how the system is rotating see figure 24.

The velocity dispersion ranges from 50 km s^{-1} to 300 km s^{-1} for both stars and gas. However, the gas velocity dispersion shows the same disturbances as the ones seen on the velocity maps, which are also not observed in the stellar velocity map. It makes sense that we see greater perturbations in the gas. Since the gas has lower inertia than stars, it

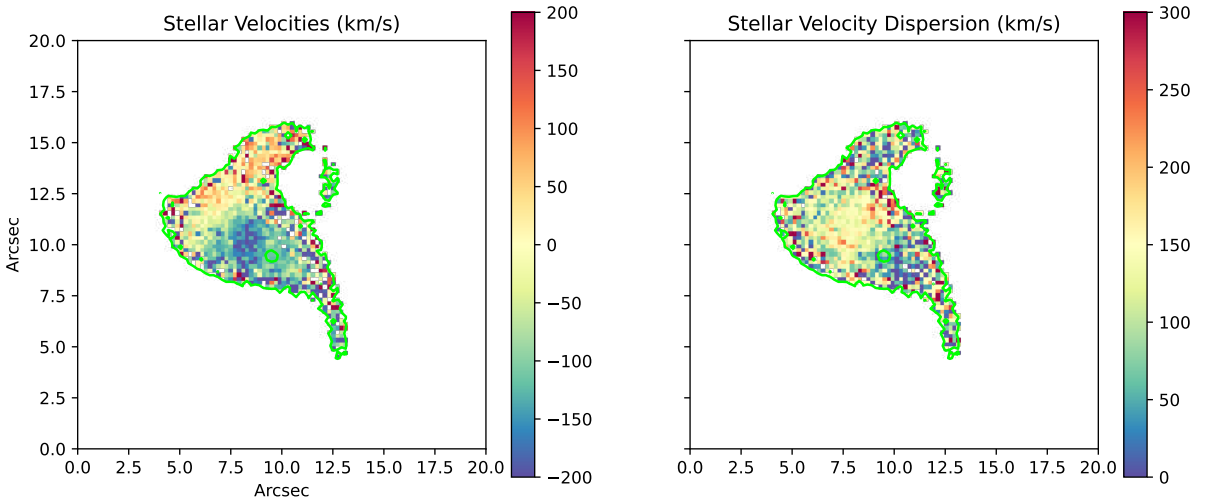

Figure 23 – Isolated stellar velocity and velocity dispersion maps of SDSSJ0849.

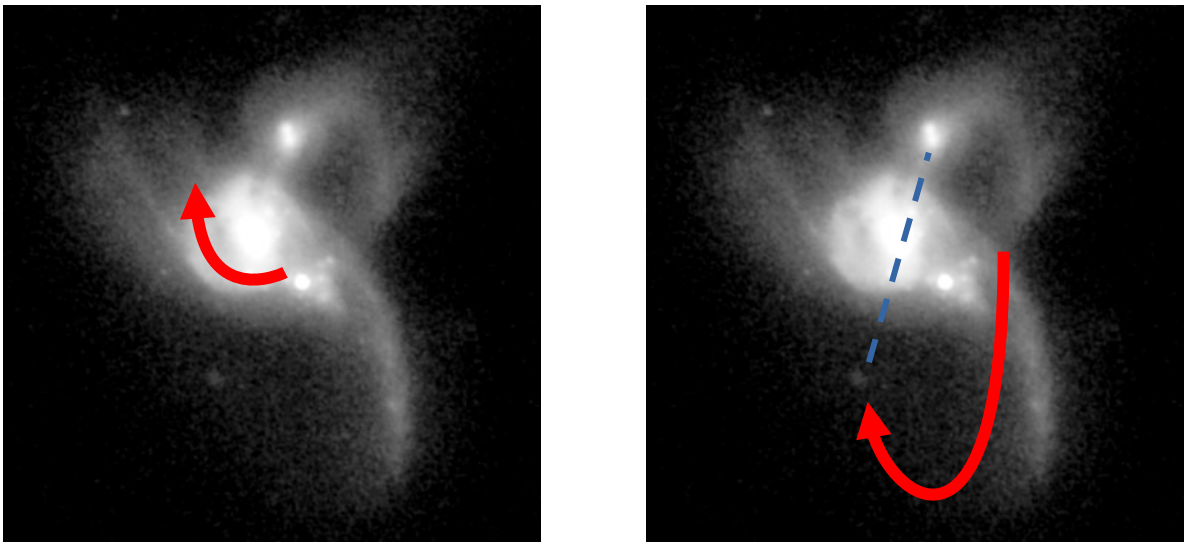

Figure 24 – Infrared image of SDSSJ0849 from Hubble Space Telescope, using Wide Field Camera 3 (WFC3) IR F105W; the arrows represent the direction of rotation of the interacting system. The main and south nuclei appear to be rotating from right to left at an angle of approximately 45°. In contrast, the north nucleus seems to rotate in a plane that is nearly perpendicular to the rest of the interacting system. We propose that during the merger, the host galaxy of the north nucleus followed the path indicated by the arrows, and is now back at the top.

is more susceptible to dynamic perturbations.

3.3 STELLAR POPULATION SYNTHESIS

We have obtained interesting results from the stellar population synthesis. The average age of the stars by pixel and their average metallicity, also by pixel, are shown in figure 25. They show that, on average, the SPs of SDSSJ0849 are very old, their ages ranging from ~ 9 to 10 Gyr, and have metallicity values ranging from $Z \sim 0.050$ to 0.015 up to values close to the Sun's ($Z \sim 0.020$ to 0.030). These relatively low metallicity levels are indicatives of a population that has not undergone extensive enrichment through supernovae and other stellar processes, which is consistent with older SPs.

I then separated the SPs by age, divided into three categories: young stars, intermediate age stars and old stars. Young stars are the ones with ages ≤ 100 Myr, intermediate age stars are the ones with ages between 100 Myr and 1 Gyr, and old stars are the ones with ages ≥ 1 Gyr. Stellar light and mass fraction maps by age (Figure 26) help us identify which regions are more populated by a given SP. Both light and mass fraction maps show that the central region around the main and north nuclei, while the rest of the interacting system have light and mass fractions dominated by intermediate age SPs. We call the attention, however, to the maps of light and mass fractions of young age SPs. While they contribute to these fractions with little over zero percent in almost the whole interacting system, they can be seen around the north and south nuclei. Contributing with $\sim 40\%$ of the light fraction in that region, the distribution around the south nucleus is very asymmetrical, and slightly dislocated from it. While we would have needed results from

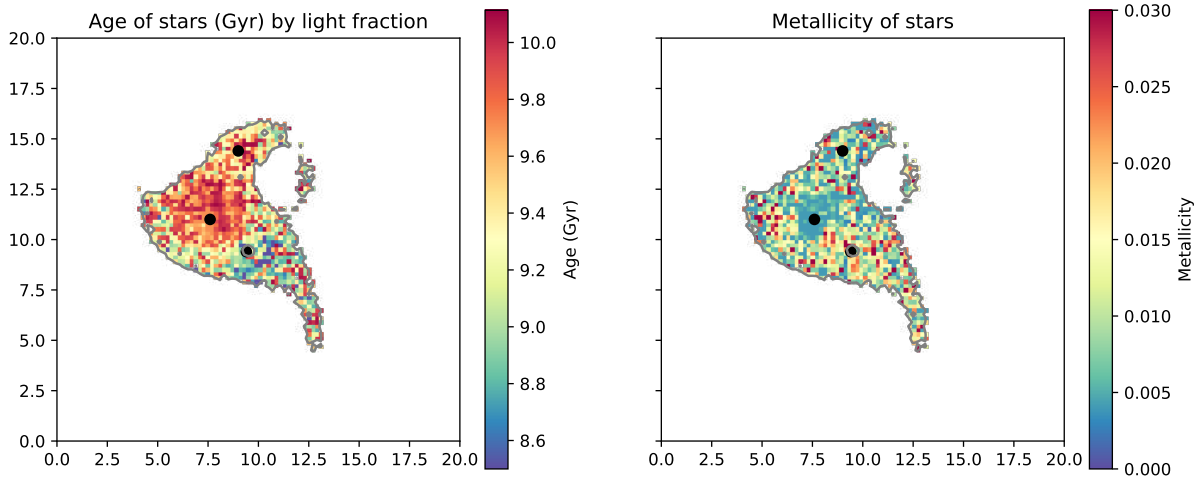

Figure 25 – The left panel shows the average age of stars throughout SDSSJ0849: stellar population of old stars, with the oldest ones present in the central region with average ages of ~ 9 to 10 Gyr and younger ones on the outskirts of the interacting system and around the south nucleus. These stars have average ages of ~ 7 to 8 Gyr. The right panel shows the metallicity of the stars: the stars in SDSSJ0849 have low values of metallicity around the main nucleus. In the other regions of the interacting system, the value of the metallicity is around that of the Sun. The black dots represent the three nuclei positions.

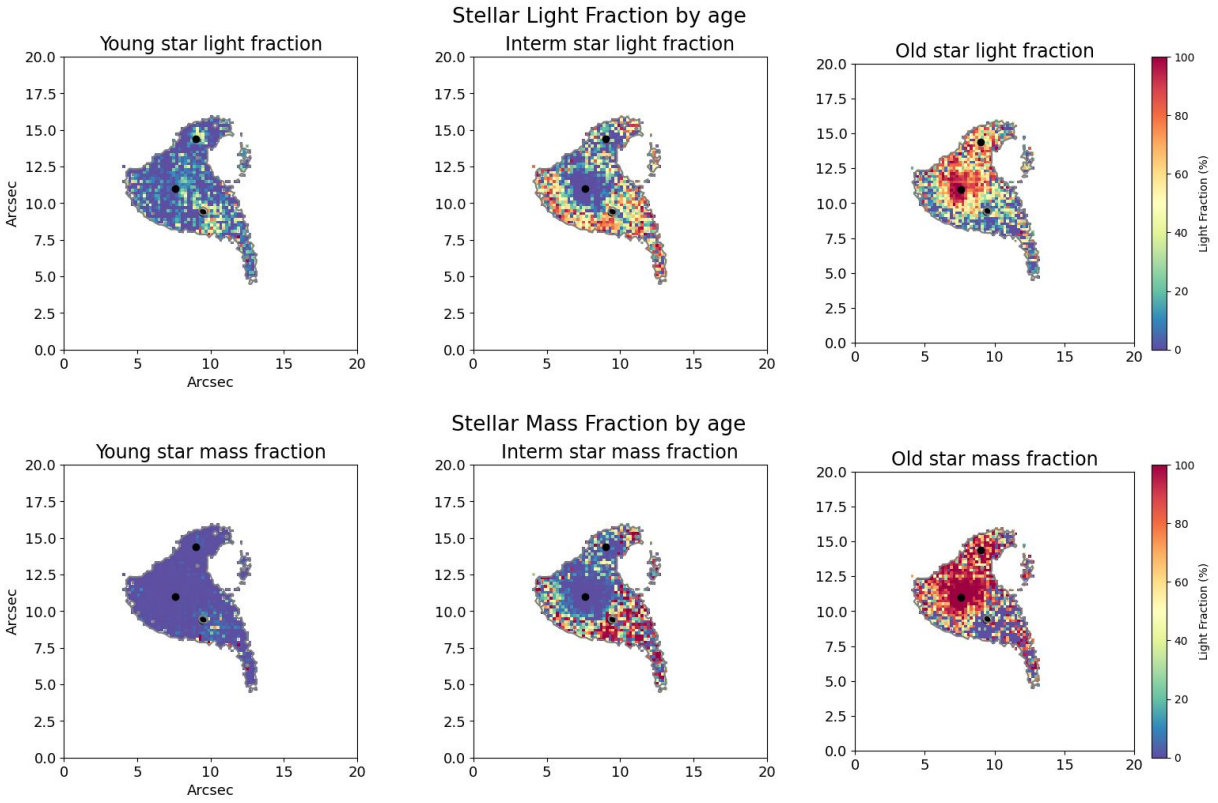

Figure 26 – The top three panels shows the light fraction of stars by age, while the bottom three show the mass fraction by age. The three black dots represent the position of the three nuclei. Older SPs dominate both the light and the mass fractions around the main and north nuclei. Intermediate age SPs the fractions in the outskirts of the interacting system, and young SPs can be seen around the south nucleus, and are more evident in the light fraction map than in the mass fraction one.

SFR to determine if this was caused by a starburst or if the stars from the south nucleus host galaxy had had younger stars prior to the interaction, these details can give us a hint. Allied to the asymmetry of the young SPs distribution, the fact that these stars are very young, less than 100 million years, suggest that these stars might have been formed while the interaction was already happening, or as a result of it. This is not definitive, and further analysis must be conducted for a clearer answer. However, this is a strong indicator that the interaction is driving star formation. The contribution of these SPs to the mass fraction is not as high, only $\sim 20\%$. Around the north nucleus we can also see young age SPs as well, and the same arguments for those around the south nucleus can be used here to suggest that star formation is happening around the north nucleus as well. However, unlike the others, these SPs don't contribute much for the mass fraction.

The reddening map is shown in figure 27. Throughout most of the interacting system, the reddening caused by dust is, on average, $\lesssim 0.6$mag. Reddening is stronger around the nuclei and close to the outer limits of the interacting system. Reddening surpasses the value of 1mag in region around the north nucleus down in the direction of

the main nucleus. We have seen evidence of the perpendicular orbit of the north nucleus host galaxy to the plane of rotation of the other two in section 3.2, and this region aligns with its hypothesized pathway. However, this trail of dust left by the north nucleus is not clear, which can suggest that the gas is too rarefied. The percentage deviation map (Figure 28) shows the quality of the results obtained, with percentages below 10% around the main and south nuclei, and the highest values around the north nucleus and at the edges of the interacting system are lower than 20%.

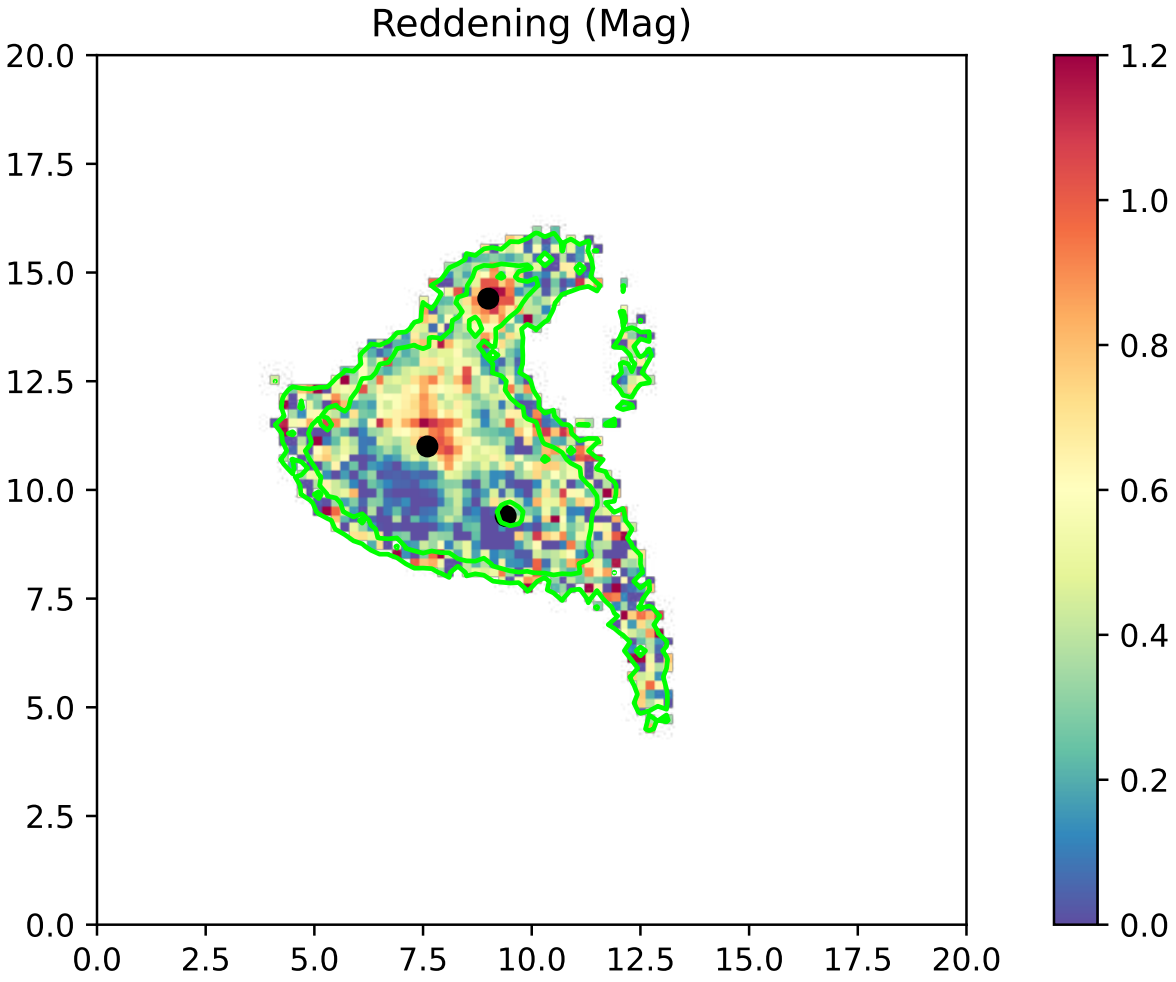

Figure 27 – Reddening (Av) map for SDSSJ0849. Throughout the interacting system, the reddening due to dust is, on average, $\lesssim 0.6$ Mag. The values go up in the region around the north nucleus extending down in the direction of the main region. This region coincides with the hypothesized pathway of the North nucleus orbit, and could suggest that it is leftover gas from its host galaxy, although the absence of a more clear line following that path in the reddening map suggests that this gas is very rarefied

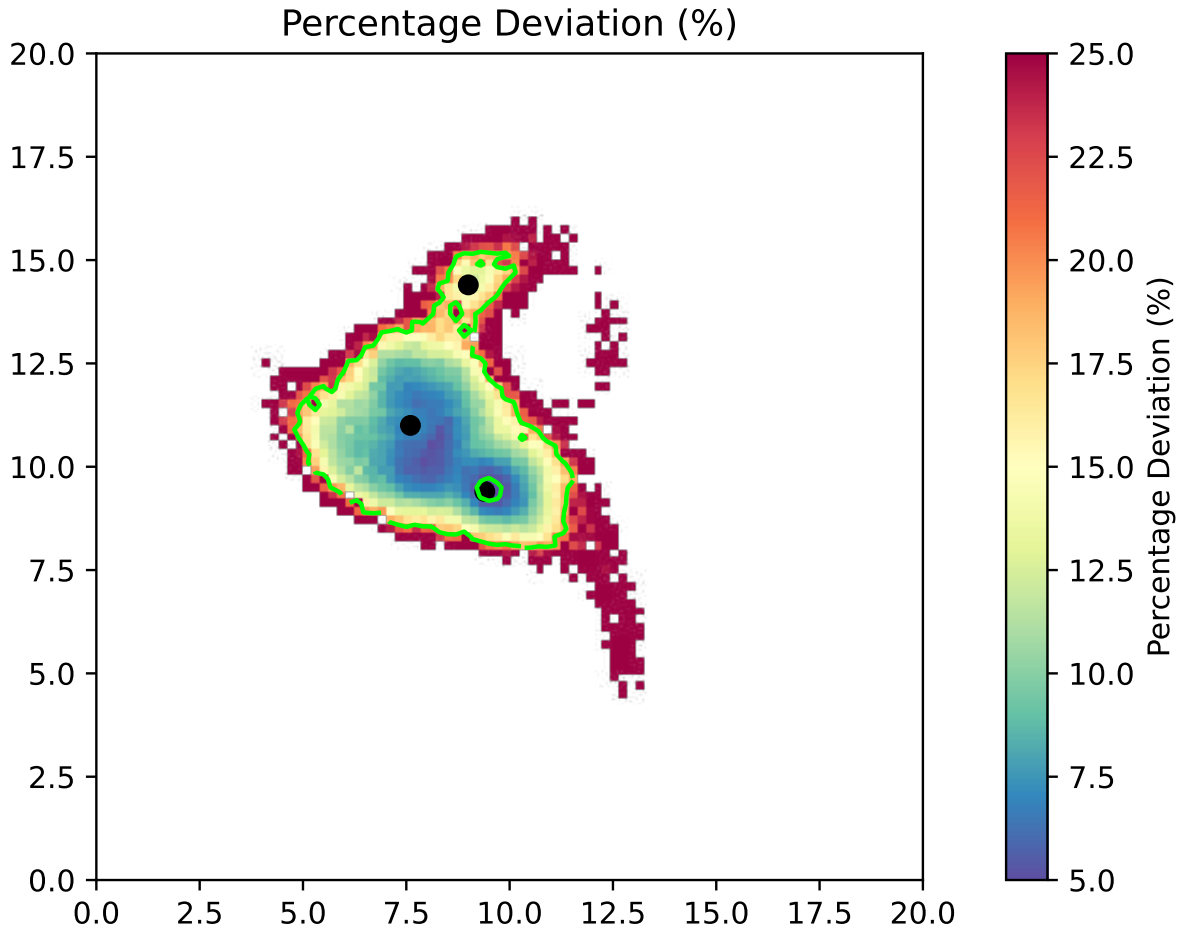

Figure 28 – Mean percentage deviation (Adev) show values bellow 15% throughout the interacting system, showing the good quality of our results. Close to the contour, the values go up to 25%, since those are regions with less signal.

3.4 BPT AND WHAN DIAGRAMS

Figures 29 and 30 show the WHAN and BPT diagrams based on the emission line ratios for the main and weaker fit components. Each figure has three subplots: The BPT diagram, the spatial distribution of the BPT classification, and the WHAN diagram. The BPT diagram is the plot of the emission-line flux ratios [O III] λ5007/Hβ against [N II] λ6583/Hα. The central solid black curve represents the separation proposed by Kewley et al. while the dashed curve represents the demarcation between AGN and star-forming regions, proposed by Stasińska et al. [Kewley et al. 2001, Stasinska et al. 2006]. Each point in both BPT and WHAN diagrams corresponds to a spaxel and each color corresponds to the respective region of the same color in the spatial distribution plot. This way, we can easily identify the photoionization processes occurring in each region of the system. Looking at the BPT diagram for the main component (Figure 29), we find that most of the interacting system's emission is consistent with ionization by harder sources than those typically associated with star formation. The distribution of points above the Stasińska's

line suggests that most of the gas is being photoionized by harder sources than SF. These line ratios above it can be caused by other processes such as heating from shockwaves. However, the spatial distribution along with the detected x-ray emissions coming from the three nuclei strongly supports the idea that the ionization is predominantly driven by AGN activity, since we know that the three nuclei are active.

The WHAN diagram provides additional insights into the nature of the ionizing radiation. In the WHAN diagram, we examine the relationship between the [N II] λ6583/Hα ratio and the equivalent width of the Hα emission line. This diagram helps to distinguish regions ionized by AGN, star formation, and other processes such as shockwave ionization. The classification on the WHAN diagram is in line with the findings from the BPT diagram, showing that a major portion of the system's emission is consistent with strong and weak AGN photoionization. It also shows that the region along the south arm is mainly ionized by SF, as well as a small region east of the south nucleus.

When plotting the BPT and WHAN diagram for the weak component, we see clearly that the gas is being strongly ionized by the main nucleus. This result gives us a very valuable insight about the physical nature of the weak component, which will be discussed in the next section.

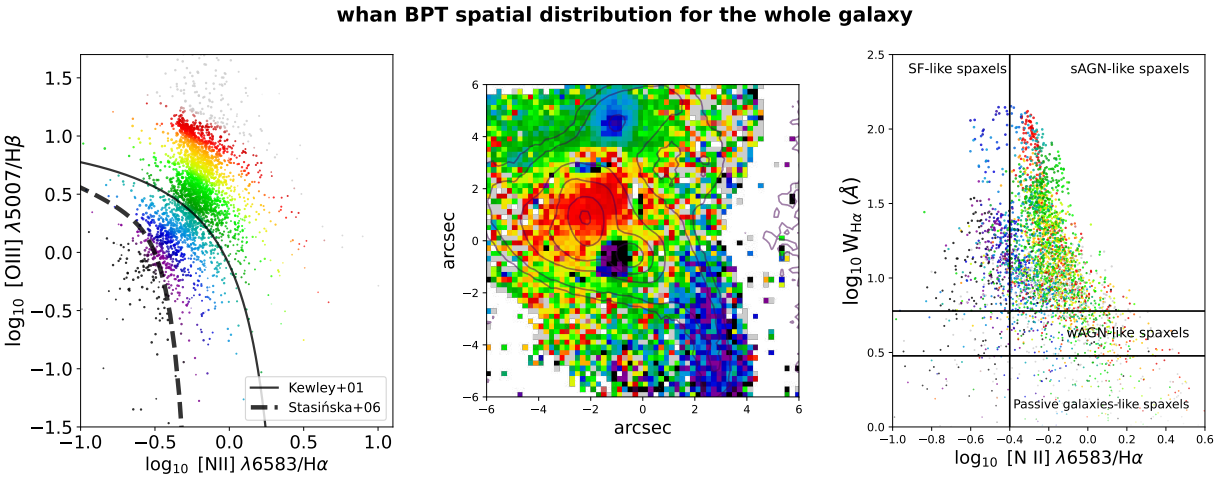

Figure 29 – WHAN and BPT diagrams for the main fit component of SDSSJ0849. The left figure shows the BPT diagram; the center figure is a color map of the interacting system; the right figure shows the WHAN diagram. All three figures are color-coded to better identify which regions present in the interacting system have different photoionization processes.

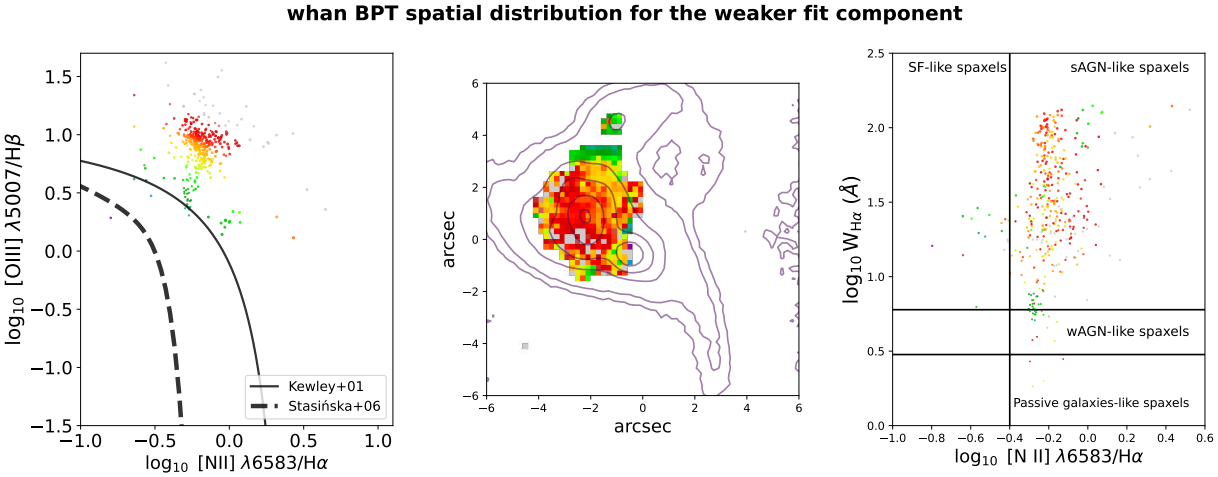

Figure 30 – WHAN and BPT diagrams for the secondary fit component of SDSSJ0849. The left figure shows the BPT diagram; the center figure is a color map of the interacting system; the right figure shows the WHAN diagram. All three figures are color-coded to better identify which regions present in the interacting system have different photoionization processes.

3.5 THE TRUE NATURE OF THE SECONDARY COMPONENT

During our analyses, one question lingered: what is the physical process behind the need of a second component to properly fit our data? We initially speculated that it could be caused by the perpendicular orbit of the north nucleus. In this case, the observed differences in direction and velocity between the two components could be explained by a cloud of gas in front of the center region of the interacting system left there by the north nucleus' host galaxy. However, when analyzing the BPT and WHAN diagrams, we saw that this gas is being ionized by the main nucleus, suggesting that it is physically closer to it. The leftover cloud would be much further away from the nucleus. Suspecting that the weak component may be associated to the activity of the main nucleus, we referred back to the study conducted by Peng et al. [Peng et al. 2022], whose findings are detailed in section 1.3 of the Introduction chapter. In the mentioned study, they identified AGN-driven outflows caused by a double-sided radio jet extending from the main nucleus. We compared the position of the jets relative to the AGN with the region where the secondary component was needed. We found that they coincide spatially when plotted together (Figure 31). This allows us to explain why the the gas in the second component had a significantly higher velocity dispersion than the the gas in the main component.

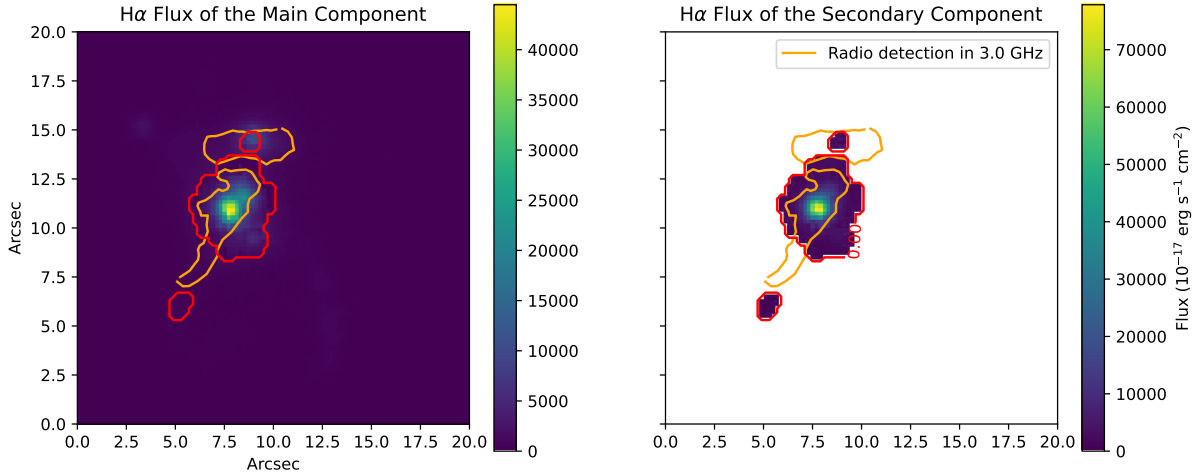

Figure 31 – Plot of the Hα flux of the main and secondary component. The contour in red is our mask, and the contour in orange is the radio detection in 3.0 GHz [Peng et al. 2022]. The position of the radio jets and with the region where the secondary component is coincide, which suggests that gas outflow is the reason we need a second component.

4 CONCLUSIONS

The main goal of this work was to study the trio of interacting galaxies SDSSJ0849, the first discovered triple Type 2 Seyfert galaxy. We used integral field spectroscopy data obtained with the MUSE instrument, installed on the Very Large Telescope (VLT) of the European Southern Observatory (ESO). Based on this data, we conducted a series of analysis based on the spectrum of the galaxy, which has three active nuclei confirmed by X-ray emission.

4.1 OUR FINDINGS

Using the IFSCube software, I fitted 10 emission lines using Gaussian functions: Hβ λ4861 , [O III] λ4959, [O III] λ5007, [N II] λ6300, [N II] λ6364,[O I] λ6548, Hα λ6563, [N II] λ6583, [S II] λ6717, and [S II] λ6730. We identified the presence of a region of narrow lines extended across all the three galaxies in the system. Their relative velocities range between $\pm$200 kms^{-1}. These values correspond to the projected velocity in our line of sight; their magnitude might be greater than the measured values.

When analyzing our data, we noticed the presence of two regions in the interacting system where one Gaussian function was not enough to properly fit the emission lines. One of these regions is located near the center of the interacting system, the other region is further away from the three interacting galaxies. It is very small, and is located south from the main nucleus. We added a second Gaussian function in these regions in order to study the gas kinematics. We believe this is the result of feedback from the main nucleus causing gas outflows. This idea is supported by previously reported radio emissions, where it was found the existence of a double-sided radio jet coming from it [Peng et al. 2022], and our own emission line ratio analysis. The BPT and WHAN help us to determine what ionization processes are present in the system. For the main component, most points in the BPT diagram lie above the Stasińska line, and in the strong AGN-like spaxels quadrant of the WHAN diagram. This suggest that the source of ionization of the gas in the regions around the three nuclei is the AGN, specially around the main nucleus. The diagrams also indicate star formation along the arm connected to the south nucleus. For the second component, all points lie well above the Stasińska line. It is clear that the gas is being photoionized by the main nucleus, which further supports the presence of AGN feedback and gas outflow.

By analyzing the velocity maps, we determined the direction that gas is flowing in our line of sight and found that the north nucleus orbits perpendicular to the rotation of the other two galaxies, the ones hosting the main and south nuclei. We can see on the gas velocity map that the gas near the north nucleus is moving away from us forming a downward arch. In the region south from the interacting system, gas is moving towards us in an upwards arch. These two structures seem to align, which led us to the following

conclusion. From the faint gas clouds that we see, we argue that this galaxy has probably already circled the other two at least once, leaving these trails behind. The other two galaxies, main and south nuclei host galaxies, are in turn orbiting each other from left to right, tilted in an angle of approximately $-135°$.

Stellar population results show that the galaxy has, on average, an older star population with low metallicity. The average metalicity in most parts of the galaxy is around $Z \sim 0.050 - 0.015$, reaching $Z \sim 0.030$ in very few spots. For reference, the Sun's metallicity is around $Z \sim 0.020 - 0.030$. These values are indicatives that the stellar population has not undergone extensive enrichment of the gas, which is consistent with older SPs.

Analyses of the light and mass fractions by age show that older stars (older than 1 Gyr) dominate those fractions in the central regions of the system, specially around the main nucleus, extending up towards the north nucleus, intermediate age stars (older than 100 Myr but younger than 1 Gyr) dominate the light and mass fractions close to the outer limits of the system, around the south nucleus and extending to the connecting arm. In the region around the South nucleus, young stars dominate around 30% of the mass fraction, and 50% of the light fraction. However, the distribution of young stars around the south nucleus is very asymmetrical, which suggests a burst of star formation in that region. Since they are very young stars, they were probably formed after the interaction had already started, and might have possibly been caused by it.

Reddening (Av) caused by dust is, on average, below 1 mag throughout the system, but is higher near the northern nucleus down in the direction of the main nucleus, with values up to 1.2 mag. This region coincides with the hypothesized pathway of the north nucleus' orbit, which can be another evidence supporting this idea. We suggest that this the reddening in this region could be caused by leftover gas from its host galaxy. However the absence of a more clear line following that path in the map indicates that, if this is the case, the gas is very rarefied.

While we know that gas is falling towards the three black holes, since they are active, we can't see that motion reflected in our data. Due to the disturbance in the gas, and the complexity of the galactic system, more analyses are needed. However, those are not simple, and might even be impossible to do. The usual methods are based on assumptions about the galactic disk that cannot be applied to a complex system as ours.

4.2 NEXT STEPS

This work has produced interesting results about the current state of SDSSJ0849. The next natural step is to compare our results with other interacting systems, in order to try to better understand the underlying mechanisms that govern galactic mergers. Through these comparisons, we can draw a more general picture that serves as a link for cosmological and galaxy evolution models. The challenges that we faced throughout this

work have highlighted the complexity of these systems. One of the biggest ones was the noise that compromised the quality of our data, and forced us to discard 80% of it. To avoid completely wasting the telescope time used, a new reduction of the data could be conducted from the raw images. More analyses focused on the black holes could also be of interest, such as their mass accretion rate.

BIBLIOGRAPHY

ALLINGTON-SMITH, J. Basic principles of integral field spectroscopy. *New Astronomy Reviews*, v. 50, n. 4-5, p. 244–251, jun. 2006. ISSN 13876473. Available at: <https://linkinghub.elsevier.com/retrieve/pii/S1387647306000157>. Cited in page 32.

Allington-Smith, J.; Content, R. Sampling and Background Subtraction in Fiber-Lenslet Integral Field Spectrographs. *PASP*, v. 110, n. 752, p. 1216–1234, out. 1998. Cited in page 32.

ALMEIDA, C. R.; RICCI, C. Nuclear obscuration in active galactic nuclei. v. 1, n. 10, p. 679–689, 2017. ISSN 2397-3366. Available at: <http://www.nature.com/articles/s41550-017-0232-z>. Cited 2 times in pages 22 and 23.

ANTONINI, F.; GIELES, M.; GUALANDRIS, A. Black hole growth through hierarchical black hole mergers in dense star clusters: implications for gravitational wave detections. *Monthly Notices of the Royal Astronomical Society*, Oxford University Press (OUP), v. 486, n. 4, p. 5008–5021, maio 2019. ISSN 1365-2966. Available at: <http://dx.doi.org/10.1093/mnras/stz1149>. Cited in page 19.

ANTONUCCI, R. Unified models for active galactic nucle and quasars. v. 31, n. 1, p. 473–521, 1993. ISSN 0066-4146. Available at: <http://adsabs.harvard.edu/abs/1993ARA&A..31..473A>. Cited in page 21.

Antonucci, R. R. J. Optical spectropolarimetry of radio galaxies. *ApJ*, v. 278, p. 499–520, mar. 1984. Cited in page 21.

ANTONUCCI, R. R. J.; MILLER, J. S. Spectropolarimetry and the nature of NGC 1068. v. 297, p. 621, 1985. ISSN 0004-637X. Available at: <http://adsabs.harvard.edu/abs/1985ApJ...297..621A>. Cited in page 21.

Bacon, R. et al. The MUSE second-generation VLT instrument. In: McLean, I. S.; Ramsay, S. K.; Takami, H. (Ed.). *Ground-based and Airborne Instrumentation for Astronomy III*. [S.l.: s.n.], 2010. (Society of Photo-Optical Instrumentation Engineers (SPIE) Conference Series, v. 7735), p. 773508. Cited in page 33.

BALDWIN, J. A.; PHILLIPS, M. M.; TERLEVICH, R. Classification parameters for the emission-line spectra of extragalactic objects. *Publications of the Astronomical Society of the Pacific*, The Astronomical Society of the Pacific, v. 93, n. 551, p. 5, fev. 1981. Available at: <https://dx.doi.org/10.1086/130766>. Cited 2 times in pages 23 and 24.

BARGER, A. J. et al. X-ray, optical, and infrared imaging and spectral properties of the 1 m[clc]s[/clc] chandra deep field north sources. *The Astronomical Journal*, American Astronomical Society, v. 124, n. 4, p. 1839–1885, out. 2002. ISSN 1538-3881. Available at: <http://dx.doi.org/10.1086/342448>. Cited in page 22.

Barger, A. J. et al. Submillimetre-wavelength detection of dusty star-forming galaxies at high redshift. *Nature*, v. 394, n. 6690, p. 248–251, jul. 1998. Cited in page 16.

Barton, E. J.; Geller, M. J.; Kenyon, S. J. Tidally Triggered Star Formation in Close Pairs of Galaxies. *ApJ*, v. 530, n. 2, p. 660–679, fev. 2000. Cited in page 18.

BEGELMAN, M. C.; BLANDFORD, R. D.; REES, M. J. Massive black hole binaries in active galactic nuclei. v. 287, p. 307–309, 1980. ISSN 0028-0836. ADS Bibcode: 1980Natur.287..307B. Available at: <https://ui.adsabs.harvard.edu/abs/1980Natur.287..307B>. Cited in page 19.

BERNARDIS, P. de et al. A flat universe from high-resolution maps of the cosmic microwave background radiation. *Nature*, Springer Science and Business Media LLC, v. 404, n. 6781, p. 955–959, abr. 2000. ISSN 1476-4687. Available at: <http://dx.doi.org/10.1038/35010035>. Cited in page 16.

Blandford, R.; Meier, D.; Readhead, A. Relativistic Jets from Active Galactic Nuclei. *ARA&A*, v. 57, p. 467–509, ago. 2019. Cited in page 20.

BLECHA, L.; SNYDER, G. F.; SATYAPAL, S.; ELLISON, S. L. The power of infrared agn selection in mergers: a theoretical study. *Monthly Notices of the Royal Astronomical Society*, Oxford University Press (OUP), v. 478, n. 3, p. 3056–3071, maio 2018. ISSN 1365-2966. Available at: <http://dx.doi.org/10.1093/mnras/sty1274>. Cited in page 28.

BOLTON, C. T. Identification of cygnus x-1 with hde 226868. *Nature*, Springer Science and Business Media LLC, v. 235, n. 5336, p. 271–273, fev. 1972. ISSN 1476-4687. Available at: <http://dx.doi.org/10.1038/235271b0>. Cited in page 19.

BRUZUAL, G.; CHARLOT, S. Stellar population synthesis at the resolution of 2003. v. 344, n. 4, p. 1000–1028, 2003. ISSN 0035-8711. Available at: <http://onlinelibrary.wiley.com/doi/10.1046/j.1365-8711.2003.06897.x/fullhttps://academic.oup.com/mnras/article-lookup/doi/10.1046/j.1365-8711.2003.06897.x>. Cited 2 times in pages 7 and 42.

Cardelli, J. A.; Clayton, G. C.; Mathis, J. S. The Relationship between Infrared, Optical, and Ultraviolet Extinction. *ApJ*, v. 345, p. 245, out. 1989. Cited in page 39.

CHABRIER, G. Galactic stellar and substellar initial mass function. *Publications of the Astronomical Society of the Pacific*, IOP Publishing, v. 115, n. 809, p. 763–795, jul. 2003. ISSN 1538-3873. Available at: <http://dx.doi.org/10.1086/376392>. Cited in page 42.

COLLESS, M. et al. The 2df galaxy redshift survey: spectra and redshifts. *Monthly Notices of the Royal Astronomical Society*, Oxford University Press (OUP), v. 328, n. 4, p. 1039–1063, dez. 2001. ISSN 1365-2966. Available at: <http://dx.doi.org/10.1046/j.1365-8711.2001.04902.x>. Cited in page 16.

CROTON, D. J. et al. The many lives of active galactic nuclei: cooling flows, black holes and the luminosities and colours of galaxies. *Monthly Notices of the Royal Astronomical Society*, Oxford University Press (OUP), v. 365, n. 1, jan. 2006. ISSN 1365-2966. Available at: <http://dx.doi.org/10.1111/j.1365-2966.2005.09675.x>. Cited in page 14.

DARG, D. W. et al. Galaxy zoo: multimergers and the millennium simulation: Galaxy zoo: multimergers and millennium. *Monthly Notices of the Royal Astronomical Society*, Oxford University Press (OUP), v. 416, n. 3, p. 1745–1755, ago. 2011. ISSN 0035-8711. Available at: <http://dx.doi.org/10.1111/j.1365-2966.2011.18964.x>. Cited in page 29.

Davis, M.; Huchra, J.; Latham, D. W.; Tonry, J. A survey of galaxy redshifts. II. The large scale space distribution. *ApJ*, v. 253, p. 423–445, fev. 1982. Cited in page 15.

Decleir, M. et al. SpeX Near-infrared Spectroscopic Extinction Curves in the Milky Way. *ApJ*, v. 930, n. 1, p. 15, maio 2022. Cited in page 39.

Edge, D. O.; Shakeshaft, J. R.; McAdam, W. B.; Baldwin, J. E.; Archer, S. A survey of radio sources at a frequency of 159 Mc/s. *MmRAS*, v. 68, p. 37–60, jan. 1959. Cited in page 20.

EINSTEIN, A. Die grundlage der allgemeinen relativitätstheorie. *Annalen der Physik*, Wiley, v. 354, n. 7, p. 769–822, jan. 1916. ISSN 1521-3889. Available at: <http://dx.doi.org/10.1002/andp.19163540702>. Cited in page 18.

ELLISON, S. L. et al. A definitive merger-agn connection at z approx 0 with cfis: mergers have an excess of agn and agn hosts are more frequently disturbed. *Monthly Notices of the Royal Astronomical Society*, Oxford University Press (OUP), v. 487, n. 2, p. 2491–2504, maio 2019. ISSN 1365-2966. Available at: <http://dx.doi.org/10.1093/mnras/stz1431>. Cited in page 28.

FABIAN, A. Observational evidence of active galactic nuclei feedback. v. 50, n. 1, p. 455–489, 2012. ISSN 0066-4146. _eprint: 1204.4114. Available at: <http://www.annualreviews.org/doi/10.1146/annurev-astro-081811-125521>. Cited in page 14.

Fath, E. A. The spectra of some spiral nebulae and globular star clusters. *Lick Observatory Bulletin*, v. 149, p. 71–77, jan. 1909. Cited in page 20.

FERNANDES, R. C. et al. The star formation history of seyfert 2 nuclei. v. 355, n. 1, p. 273–296, 2004. ISSN 00358711. Available at: <http://adsabs.harvard.edu/abs/2004MNRAS.355..273C>. Cited in page 43.

FERNANDES, R. C.; HECKMAN, T.; SCHMITT, H.; DELGADO, R. M. G.; STORCHI-BERGMANN, T. Empirical diagnostics of the starburst-AGN connection. v. 558, n. 1, p. 81–108. ISSN 0004-637X. Available at: <http://adsabs.harvard.edu/abs/2001ApJ...558...81C>. Cited in page 41.

FERNANDES, R. C.; STASIńSKA, G.; MATEUS, A.; ASARI, N. V. A comprehensive classification of galaxies in the sloan digital sky survey: how to tell true from fake AGN? v. 413, n. 3, p. 1687–1699, 2011. ISSN 00358711. Available at: <http://adsabs.harvard.edu/abs/2011MNRAS.413.1687C>. Cited 4 times in pages 23, 26, 27, and 44.

FERRARESE, L.; MERRITT, D. A fundamental relation between supermassive black holes and their host galaxies. v. 539, n. 1, p. L9–L12, 2000. ISSN 0004637X. Available at: <http://adsabs.harvard.edu/abs/2000ApJ...539L...9F>. Cited in page 14.

Fitzpatrick, E. L.; Massa, D.; Gordon, K. D.; Bohlin, R.; Clayton, G. C. An Analysis of the Shapes of Interstellar Extinction Curves. VII. Milky Way Spectrophotometric Optical-through-ultraviolet Extinction and Its R-dependence. *ApJ*, v. 886, n. 2, p. 108, dez. 2019. Cited in page 39.

FOORD, A.; GüLTEKIN, K.; RUNNOE, J. C.; KOSS, M. J. AGN triality of triple mergers: Detection of faint x-ray point sources. v. 907, n. 2, p. 71, 2021. ISSN 0004-637X, 1538-4357. Available at: <https://iopscience.iop.org/article/10.3847/1538-4357/abce5d>. Cited 2 times in pages 7 and 29.

FRENK, C.; WHITE, S. Dark matter and cosmic structure. *Annalen der Physik*, Wiley, v. 524, n. 9–10, p. 507–534, set. 2012. ISSN 1521-3889. Available at: <http://dx.doi.org/10.1002/andp.201200212>. Cited in page 16.

GEBHARDT, K. et al. A relationship between nuclear black hole mass and galaxy velocity dispersion. v. 539, n. 1, p. L13–L16, 2000. ISSN 0004637X. Available at: <http://adsabs.harvard.edu/abs/2000ApJ...539L..13G>. Cited in page 14.

Gies, D. R.; Bolton, C. T. The Optical Spectrum of HDE 226868=Cygnus X-1. II. Spectrophotometry and Mass Estimates. *ApJ*, v. 304, p. 371, maio 1986. Cited in page 19.

GOOBAR, A. et al. The acceleration of the universe: Measurements of cosmological parameters from type ia supernovae. *Physica Scripta*, IOP Publishing, T85, n. 1, p. 47, 2000. ISSN 0031-8949. Available at: <http://dx.doi.org/10.1238/Physica.Topical.085a00047>. Cited in page 16.

GORDON, K. et al. Milky way mid-infrared spitzer spectroscopic extinction curves: Continuum and silicate features. *The Astrophysical Journal*, v. 916, p. 33, 07 2021. Cited in page 39.

Gordon, K. D.; Cartledge, S.; Clayton, G. C. FUSE Measurements of Far-Ultraviolet Extinction. III. The Dependence on R(V) and Discrete Feature Limits from 75 Galactic Sightlines. *ApJ*, v. 705, n. 2, p. 1320–1335, nov. 2009. Cited in page 39.

GORDON, K. D. et al. One Relation for All Wavelengths: The Far-Ultraviolet to Mid-Infrared Milky Way Spectroscopic R(V) Dependent Dust Extinction Relationship. *The Astrophysical Journal*, v. 950, n. 2, p. 86, jun. 2023. ISSN 0004-637X, 1538-4357. ArXiv:2304.01991 [astro-ph]. Available at: <http://arxiv.org/abs/2304.01991>. Cited 3 times in pages 9, 37, and 40.

Greenstein, J. L.; Schmidt, M. The Quasi-Stellar Radio Sources 3C 48 and 3C 273. *ApJ*, v. 140, p. 1, jul. 1964. Cited in page 20.

Guth, A. H. Inflationary universe: A possible solution to the horizon and flatness problems. *Phys. Rev. D*, v. 23, n. 2, p. 347–356, jan. 1981. Cited in page 15.

HAAN, S. et al. Dynamical evolution of agn host galaxies—gas in/out-flow rates in seven nuga galaxies. *The Astrophysical Journal*, American Astronomical Society, v. 692, n. 2, p. 1623–1661, fev. 2009. ISSN 1538-4357. Available at: <http://dx.doi.org/10.1088/0004-637X/692/2/1623>. Cited in page 14.

HAARDT, F.; MARASCHI, L.; GHISELLINI, G. A model for the x-ray and ultraviolet emission from seyfert galaxies and galactic black holes. *The Astrophysical Journal*, American Astronomical Society, v. 432, p. L95, set. 1994. ISSN 1538-4357. Available at: <http://dx.doi.org/10.1086/187520>. Cited in page 43.

HAEHNELT, M. G.; NATARAJAN, P.; REES, M. J. High-redshift galaxies, their active nuclei and central black holes. *Monthly Notices of the Royal Astronomical Society*, Oxford University Press (OUP), v. 300, n. 3, p. 817–827, nov. 1998. ISSN 1365-2966. Available at: <http://dx.doi.org/10.1111/j.1365-8711.1998.t01-1-01951.x>. Cited in page 14.

HERNQUIST, L. Fueling activity in galactic nucleia. *Annals of the New York Academy of Sciences*, Wiley, v. 571, n. 1, p. 190–204, dez. 1989. ISSN 1749-6632. Available at: <http://dx.doi.org/10.1111/j.1749-6632.1989.tb50506.x>. Cited in page 18.

HO, L. C. Nuclear activity in nearby galaxies. *Annual Review of Astronomy and Astrophysics*, Annual Reviews, v. 46, n. 1, p. 475–539, set. 2008. ISSN 1545-4282. Available at: <http://dx.doi.org/10.1146/annurev.astro.45.051806.110546>. Cited in page 14.

Hoffman, L.; Loeb, A. Dynamics of triple black hole systems in hierarchically merging massive galaxies. *MNRAS*, v. 377, n. 3, p. 957–976, maio 2007. Cited in page 28.

HOPKINS, P. F.; COX, T. J.; KEREš, D.; HERNQUIST, L. A cosmological framework for the co-evolution of quasars, supermassive black holes, and elliptical galaxies. ii. formation of red ellipticals. *The Astrophysical Journal Supplement Series*, American Astronomical Society, v. 175, n. 2, p. 390–422, abr. 2008. ISSN 1538-4365. Available at: <http://dx.doi.org/10.1086/524363>. Cited in page 28.

Hubble, E. Extragalactic nebulae. *ApJ*, v. 64, p. 321–369, dez. 1926. Cited in page 17.

Hubble, E. A Relation between Distance and Radial Velocity among Extra-Galactic Nebulae. *Proceedings of the National Academy of Science*, v. 15, n. 3, p. 168–173, mar. 1929. Cited in page 15.

Hubble, E. *Realm of the Nebulae*. [S.l.: s.n.], 1936. Cited in page 17.

KAUFFMANN, G. et al. The host galaxies of active galactic nuclei. v. 346, n. 4, p. 1055–1077, 2003. ISSN 00358711. Available at: <http://adsabs.harvard.edu/abs/2003MNRAS.346.1055K>. Cited 2 times in pages 24 and 43.

Kauffmann, G. et al. Stellar masses and star formation histories for 10^5 galaxies from the Sloan Digital Sky Survey. *MNRAS*, v. 341, n. 1, p. 33–53, maio 2003. Cited in page 17.

Kauffmann, G. et al. The dependence of star formation history and internal structure on stellar mass for 10^5 low-redshift galaxies. *MNRAS*, v. 341, n. 1, p. 54–69, maio 2003. Cited in page 44.

KENNICUTT, J. The global schmidt law in star-forming galaxies. v. 498, n. 2, p. 541–552. ISSN 0004-637X. Available at: <http://adsabs.harvard.edu/abs/1998ApJ...498..541K>. Cited in page 18.

KEWLEY, L. J.; DOPITA, M. A.; SUTHERLAND, R. S.; HEISLER, C. A.; TREVENA, J. Theoretical modeling of starburst galaxies. v. 556, n. 1, p. 121–140, 2001. ISSN 0004-637X. Available at: <http://adsabs.harvard.edu/abs/2001ApJ...556..121K>. Cited 2 times in pages 24 and 59.

KEWLEY, L. J.; GROVES, B.; KAUFFMANN, G.; HECKMAN, T. The host galaxies and classification of active galactic nuclei. v. 372, n. 3, p. 961–976, 2006. ISSN 0035-8711. Available at: <http://adsabs.harvard.edu/abs/2006MNRAS.372..961K>. Cited 2 times in pages 25 and 27.

Khostovan, A. A. et al. Evolution of H α equivalent widths from z $\sim$ 0.4 - 2.2: implications for star formation and legacy surveys with Roman and Euclid. *MNRAS*, v. 535, n. 4, p. 2903–2926, dez. 2024. Cited in page 44.

KING, A.; POUNDS, K. Powerful outflows and feedback from active galactic nuclei. *Annual Review of Astronomy and Astrophysics*, v. 53, p. 115–154, 2015. Available at: <https://arxiv.org/abs/1503.05206>. Cited in page 14.

KORMENDY, J.; HO, L. C. Coevolution (or not) of supermassive black holes and host galaxies. v. 51, p. 511–653, 2013. ISSN 0066-4146. _eprint: 1304.7762. Available at: <http://arxiv.org/abs/1304.7762http://dx.doi.org/10.1146/annurev-astro-082708-101811>. Cited 2 times in pages 7 and 14.

KORMENDY, J.; RICHSTONE, D. Inward bound—the search for supermassive black holes in galactic nuclei. v. 33, n. 1, p. 581–624, 1995. ISSN 0066-4146. Available at: <http://www.annualreviews.org/doi/10.1146/annurev.aa.33.090195.003053http://adsabs.harvard.edu/abs/1995ARA&A..33..581K>. Cited 3 times in pages 7, 14, and 18.

KRAFT, D. A software package for sequential quadratic programming. *Technical Report DFVLR-FB 88-28*, 1988. Cited in page 44.

Lambas, D.; Alonso, S.; Mesa, V.; O'Mill, A. Galaxy interactions. I. Major and minor mergers. *A&A*, v. 539, p. A45, mar. 2012. Cited in page 18.

LARSON, R. B.; TINSLEY, B. M. Star formation rates in normal and peculiar galaxies. *The Astrophysical Journal*, American Astronomical Society, v. 219, p. 46, jan. 1978. ISSN 1538-4357. Available at: <http://dx.doi.org/10.1086/155753>. Cited in page 18.

Linde, A. D. A new inflationary universe scenario: A possible solution of the horizon, flatness, homogeneity, isotropy and primordial monopole problems. *Physics Letters B*, v. 108, n. 6, p. 389–393, fev. 1982. Cited in page 15.

LIU, X. et al. A trio of massive black holes caught in the act of merging. v. 887, n. 1, p. 90, 2019. ISSN 1538-4357. Available at: <https://iopscience.iop.org/article/10.3847/1538-4357/ab54c3>. Cited in page 29.

LIU, X.; SHEN, Y.; STRAUSS, M. A.; HAO, L. ACTIVE GALACTIC NUCLEUS PAIRS FROM THE SLOAN DIGITAL SKY SURVEY. i. THE FREQUENCY ON ∼5-100 kpc SCALES. v. 737, n. 2, p. 101, 2011. ISSN 0004-637X, 1538-4357. Available at: <https://iopscience.iop.org/article/10.1088/0004-637X/737/2/101>. Cited in page 29.

Lynden-Bell, D. Galactic nuclei as collapsed old quasars. *Nature*, v. 223, 1969. Available at: <https://www.nature.com/articles/223690a0>. Cited 2 times in pages 7 and 14.

MADAU, P.; DICKINSON, M. Cosmic star-formation history. v. 52, n. 1, p. 415–486, 2014. ISSN 0066-4146. Available at: <http://adsabs.harvard.edu/abs/2014ARA%26A..52..415M>. Cited 2 times in pages 16 and 17.

MADAU, P.; REES, M. J. Massive black holes as population iii remnants. *The Astrophysical Journal*, American Astronomical Society, v. 551, n. 1, p. L27–L30, abr. 2001. ISSN 0004-637X. Available at: <http://dx.doi.org/10.1086/319848>. Cited in page 19.

MAGORRIAN, J. et al. The demography of massive dark objects in galaxy centers. v. 115, n. 6, p. 2285–2305, 1998. ISSN 00046256. Available at: <http://adsabs.harvard.edu/abs/1998AJ....115.2285M>. Cited in page 14.

Marchesini, D. et al. The Evolution of the Stellar Mass Function of Galaxies from z = 4.0 and the First Comprehensive Analysis of its Uncertainties: Evidence for Mass-Dependent Evolution. *ApJ*, v. 701, n. 2, p. 1765–1796, ago. 2009. Cited in page 18.

MATTEO, T. D.; SPRINGEL, V.; HERNQUIST, L. Energy input from quasars regulates the growth and activity of black holes and their host galaxies. v. 433, p. 604–607, 2005. ISSN 0028-0836. ADS Bibcode: 2005Natur.433..604D. Available at: <https://ui.adsabs.harvard.edu/abs/2005Natur.433..604D>. Cited in page 14.

Moustakas, J. et al. PRIMUS: Constraints on Star Formation Quenching and Galaxy Merging, and the Evolution of the Stellar Mass Function from z = 0-1. *ApJ*, v. 767, n. 1, p. 50, abr. 2013. Cited in page 18.

MUZZIN, A. et al. The evolution of the stellar mass functions of star-forming and quiescent galaxies toz= 4 from the cosmos/ultravista survey. *The Astrophysical Journal*, American Astronomical Society, v. 777, n. 1, p. 18, out. 2013. ISSN 1538-4357. Available at: <http://dx.doi.org/10.1088/0004-637X/777/1/18>. Cited in page 18.

O'Raifeartaigh, C.; O'Keeffe, M.; Nahm, W.; Mitton, S. Einstein's 1917 static model of the universe: a centennial review. *European Physical Journal H*, v. 42, n. 3, ago. 2017. Cited in page 15.

Ostriker, J. P.; Peebles, P. J. E. A Numerical Study of the Stability of Flattened Galaxies: or, can Cold Galaxies Survive? *ApJ*, v. 186, p. 467–480, dez. 1973. Cited in page 15.

PAN, H.-A. et al. Sdss-iv manga: Spatial evolution of star formation triggered by galaxy interactions. *The Astrophysical Journal*, American Astronomical Society, v. 881, n. 2, p. 119, ago. 2019. ISSN 1538-4357. Available at: <http://dx.doi.org/10.3847/1538-4357/ab311c>. Cited in page 18.

Peng, S. et al. Very Large Array Multiband Radio Imaging of the Triple AGN Candidate SDSS J0849+1114. *ApJ*, v. 934, n. 1, p. 89, jul. 2022. Cited 5 times in pages 30, 31, 61, 62, and 63.

Penrose, R. Gravitational Collapse and Space-Time Singularities. *Phys. Rev. Lett.*, v. 14, n. 3, p. 57–59, jan. 1965. Cited in page 19.

PFEIFLE, R. W. et al. A triple agn in a mid-infrared selected late-stage galaxy merger. *The Astrophysical Journal*, American Astronomical Society, v. 883, n. 2, p. 167, out. 2019b. ISSN 1538-4357. Available at: <http://dx.doi.org/10.3847/1538-4357/ab3a9b>. Cited 2 times in pages 28 and 29.

PFEIFLE, R. W. et al. Buried black hole growth in ir-selected mergers: New results from chandra. *The Astrophysical Journal*, American Astronomical Society, v. 875, n. 2, p. 117, abr. 2019a. ISSN 1538-4357. Available at: <http://dx.doi.org/10.3847/1538-4357/ab07bc>. Cited 2 times in pages 28 and 29.

RICHSTONE, D. et al. Supermassive black holes and the evolution of galaxies. *Nature*, arXiv, 1998. Available at: <https://arxiv.org/abs/astro-ph/9810378>. Cited in page 14.

SATYAPAL, S. et al. Galaxy pairs in the sloan digital sky survey – ix. merger-induced agn activity as traced by the wide-field infrared survey explorer. *Monthly Notices of the Royal Astronomical Society*, Oxford University Press (OUP), v. 441, n. 2, p. 1297–1304, maio 2014. ISSN 0035-8711. Available at: <http://dx.doi.org/10.1093/mnras/stu650>. Cited in page 28.

SATYAPAL, S. et al. Buried agns in advanced mergers: Mid-infrared color selection as a dual agn candidate finder. *The Astrophysical Journal*, American Astronomical Society, v. 848, n. 2, p. 126, out. 2017. ISSN 1538-4357. Available at: <http://dx.doi.org/10.3847/1538-4357/aa88ca>. Cited in page 28.

Schlafly, E. F.; Finkbeiner, D. P. Measuring Reddening with Sloan Digital Sky Survey Stellar Spectra and Recalibrating SFD. *ApJ*, v. 737, n. 2, p. 103, ago. 2011. Cited in page 39.

Schmidt, M. 3C 273 : A Star-Like Object with Large Red-Shift. *Nature*, v. 197, p. 1040, 1963. Cited in page 20.

SCHWARZSCHILD, K. On the gravitational field of a mass point according to einstein's theory. arXiv, 1999. Available at: <https://arxiv.org/abs/physics/9905030>. Cited in page 18.

SEYFERT, C. K. Nuclear emission in spiral nebulae. v. 97, p. 28. ISSN 0004-637X. Available at: <http://adsabs.harvard.edu/abs/1943ApJ....97...28S>. Cited in page 20.

Shakura, N. I.; Sunyaev, R. A. Black holes in binary systems. Observational appearance. *A&A*, v. 24, p. 337–355, jan. 1973. Cited 2 times in pages 14 and 19.

SILK, J.; REES, M. J. Quasars and galaxy formation. 1998. Available at: <http://adsabs.harvard.edu/abs/1998A&A...331L...1S>. Cited in page 14.

Slipher, V. M. The spectrum and velocity of the nebula N.G.C. 1068 (M 77). *Lowell Observatory Bulletin*, v. 3, p. 59–62, jan. 1917. Cited 2 times in pages 15 and 20.

Somerville, R. S.; Davé, R. Physical Models of Galaxy Formation in a Cosmological Framework. *ARA&A*, v. 53, p. 51–113, ago. 2015. Cited 2 times in pages 14 and 16.

SOUSA, S. G.; SANTOS, N. C.; ISRAELIAN, G.; MAYOR, M.; MONTEIRO, M. J. P. F. G. A new code for automatic determination of equivalent widths: Automatic routine for line equivalent widths in stellar spectra (ares). *Astronomy & Astrophysics*, EDP Sciences, v. 469, n. 2, p. 783–791, abr. 2007. ISSN 1432-0746. Available at: <http://dx.doi.org/10.1051/0004-6361:20077288>. Cited in page 44.

STASINSKA, G.; FERNANDES, R. C.; MATEUS, A.; SODRE, L.; ASARI, N. V. Semi-empirical analysis of sloan digital sky survey galaxies - III. how to distinguish AGN hosts. v. 371, n. 2, p. 972–982, 2006. ISSN 0035-8711. Available at: <http://adsabs.harvard.edu/abs/2006MNRAS.371..972S>. Cited 3 times in pages 25, 27, and 59.

Stasińska, G. et al. Can retired galaxies mimic active galaxies? Clues from the Sloan Digital Sky Survey. *MNRAS*, v. 391, n. 1, p. L29–L33, nov. 2008. Cited in page 25.

Stockman, H. S.; Angel, J. R. P.; Miley, G. K. Alignment of the optical polarization with the radio structure of QSOs. *ApJ*, v. 227, p. L55–L58, jan. 1979. Cited in page 21.

STORN, R.; PRICE, K. Differential evolution: A simple and efficient adaptive scheme for global optimization over continuous spaces. *Journal of Global Optimization*, v. 23, 01 1995. Cited in page 44.

VOLLMANN, K.; EVERSBERG, T. Remarks on statistical errors in equivalent widths. v. 327, n. 9, p. 862–865. ISSN 0004-6337. Available at: <http://doi.wiley.com/10.1002/asna.200610645>. Cited in page 44.

Volonteri, M.; Habouzit, M.; Colpi, M. The origins of massive black holes. *Nature Reviews Physics*, v. 3, n. 11, p. 732–743, set. 2021. Cited in page 19.

WEBSTER, B. L.; MURDIN, P. Cygnus x-1—a spectroscopic binary with a heavy companion? *Nature*, Springer Science and Business Media LLC, v. 235, n. 5332, p. 37–38, jan. 1972. ISSN 1476-4687. Available at: <http://dx.doi.org/10.1038/235037a0>. Cited in page 19.

WEILBACHER, P. M. et al. Design and capabilities of the muse data reduction software and pipeline. In: RADZIWILL, N. M.; CHIOZZI, G. (Ed.). *Software and Cyberinfrastructure for Astronomy II*. SPIE, 2012. v. 8451, p. 84510B. ISSN 0277-786X. Available at: <http://dx.doi.org/10.1117/12.925114>. Cited in page 34.

WESTON, M. E. et al. Incidence of *WISE* -selected obscured AGNs in major mergers and interactions from the SDSS. v. 464, n. 4, p. 3882–3906, 2017. ISSN 0035-8711, 1365-2966. Available at: <https://academic.oup.com/mnras/article-lookup/doi/10.1093/mnras/stw2620>. Cited in page 28.

White, S. D. M.; Rees, M. J. Core condensation in heavy halos: a two-stage theory for galaxy formation and clustering. *MNRAS*, v. 183, p. 341–358, maio 1978. Cited 2 times in pages 14 and 15.

Yee, H.; Ellingson, E. Statistics of Close Galaxy Pairs from a Faint-Galaxy Redshift Survey. *ApJ*, v. 445, p. 37, maio 1995. Cited in page 18.

York, D. G. et al. The Sloan Digital Sky Survey: Technical Summary. *AJ*, v. 120, n. 3, p. 1579–1587, set. 2000. Cited in page 21.

Zwicky, F. Republication of: The redshift of extragalactic nebulae. *General Relativity and Gravitation*, v. 41, n. 1, p. 207–224, jan. 2009. Cited in page 15.